PERFORMANCE LIMITS OF OPTICAL RECTENNAS

by

SAUMIL JOSHI

B.E., Electrical Engineering
University of Delhi, 2009

M.S., Electrical Engineering
University of Colorado, 2011

A thesis submitted to the

Faculty of the Graduate School of the

University of Colorado in partial fulfillment

of the requirement for the degree of

Doctor of Philosophy

Department of Electrical, Computer, and Energy Engineering

2015

This thesis entitled:

Performance limits of optical rectennas

written by Saumil Joshi

has been approved for the Department of Electrical, Computer, and Energy Engineering

_____

(Prof. Garret Moddel)

_____

(Prof. Wounjhang Park)

Date_____

The final copy of this thesis has been examined by the signatories, and we find that both the content and the form meet acceptable presentation standards of scholarly work in the above mentioned discipline.

Joshi, Saumil (Ph.D., Electrical Engineering)

Performance limits of optical rectennas

Thesis directed by Prof. Garret Moddel

Optical rectennas are antenna-coupled diode rectifiers that receive and convert optical-frequency electromagnetic radiation into DC output. Because classical rectennas working at microwave frequencies can achieve very high rectification efficiencies, rectennas working as solar cells were expected to have efficiencies significantly higher than conventional solar cells. By applying the theory of photon-assisted tunneling (PAT) to optical rectennas at solar intensities, I show that the power conversion efficiency of rectenna solar cells is fundamentally limited to the Trivich-Flinn efficiency limit of 44%. This unexpected result is the same as the Shockley-Queisser ultimate efficiency limit of conventional solar cells.

Is it possible to exceed this efficiency limit? I answer this question by showing that there is a correspondence between the quantum and classical operation of a rectenna. Such correspondence allows high frequency rectennas to operate in the same way as classical rectennas, and to potentially exceed the Trivich-Flinn efficiency limit. I propose two ways to achieve classical operation in optical rectennas.

Diode design is crucial for achieving high rectification efficiency. High-speed diodes, such as metal-insulator-metal (MIM) diodes, have insufficient asymmetry for harvesting low intensity radiation. I suggest steps to improve the characteristics of double insulator MIM diodes and calculate their power conversion efficiency using PAT theory. A simple figure of merit is provided to quickly assess the usefulness of MIM diodes in optical rectennas.

Although ineffective at visible frequencies, MIM diodes have *RC* time constants sufficient for operation at low terahertz frequencies, useful in applications including detection and high-speed electronics. I develop the steps to design MIM diodes at 1 THz, propose materials that will give the required current-voltage characteristics and *RC* time constant, perform electrical and optical measurements on fabricated devices, and suggest steps to improve their performance.

In contrast to MIM diodes, novel planar devices called geometric diodes have very low *RC* time constants and are capable of rectifying radiation up to 100 THz. I measure the infrared optical response of graphene-based geometric diodes, and demonstrate one of the best room-temperature detectors working at 28 THz.

Dedicated to my parents and teachers

ACKNOWLEDGMENTS

I express my deepest gratitude to my thesis advisor Prof. Garret Moddel for his meticulous efforts in helping and encouraging me to grow as a researcher, for teaching me lessons I will always value, and for being a most caring parent away from home. Garret, I will always treasure the memories of these last five years. I am very fortunate of having you as my mentor.

I am most grateful to my parents, Dr. P. K. Joshi and Mrs. Rashmi Joshi, for teaching me everything, for imparting in me the best of the values, for their relentless support towards my goals and pursuits, and for all that I am today. I thank my brother, Mayank, for his persistent belief in my abilities, and for being my best friend. I am thankful to my sister-in-law, Vasudha, for her never-tiring encouragement and care, and for sending me sweets to cheer me up! My sincere regards to my grandparents for their blessings. Words are not enough to express my gratitude to all of you.

I am indebted to Prof. Wounjhang Park for his help and support, and for giving me my first experience of excellent research at the University of Colorado. I greatly appreciate the help and guidance of my committee members: Prof. Dragan Maksimovic, Prof. Milos Popovic, and Prof. Charles Rogers. I thank Prof. Al Gasiewski for his support during my first semester as a teaching assistant. Many thanks to Prof. Ravindra Sinha, Prof. Pragati Kumar, and Prof. S. Indu at the University of Delhi.

I will always be grateful to Sachit Grover and James Zhu for mentoring me during the most difficult periods of my graduate work. I cannot thank them enough for helping me learn crawl and walk as a researcher, and for their utmost care for me outside the lab. I thank Olga Dmitriyeva and Kendra Krueger for always being supportive. I am grateful to Dave Doroski for his encouragement, his amusing stories, and for his interesting tales about his garden. I thank Brad Pelz for being the most supportive friend and colleague over the last one year, and for his best efforts in encouraging me to get out of the lab and relax. I am thankful to Dr. Michael Cromar for his encouragement, his thought-provoking ideas, and for the knowledge I gained from his wealth of experience. Also, many thanks to Amina Belkadi for her patience with my work and help with my writing, to Anu Jagia for her extensive help during the last few months of my thesis work. All the best to Shuai for his graduate studies in the group. Thanks to friends and colleagues outside the lab including Sandeep Srikumar, Ginni Grover, Kaniska Mohanty, Xi Chen, Yonghao Cui, Natalia Azarova, Chenchen Mao, Sungmo Ahn, Suehyun Cho, Dawei Liu, Tzu-Min Ou, Zefram Marks, Ben Pollard, Marc Castro, Yue Cao, Xinghui Liu, and Bosheng Zhang.

I am grateful to Pat Brady and Jim Nelson of RedWave Inc, and Dave Powell of Abengoa Solar for their financial support. Many thanks to members of the RedWave team, including Zach Thacker, Dale Kotter, Pallab Midya, Patrick Pinhero, and Dennis Slafer.

Thanks to friends back home including Abhishek, Rajat, and Someshwar. Many thanks to the entire Boulder gang: I will be forever grateful to Vikram for taking care of me in Boulder, and for his never-ending concern about my well-being; thanks to Namrata for always being eager to help, for the great cakes she baked for my birthdays; I thank Anish for introducing me to Boulder, Shiva and Nithya for their support, Bhaskar for his motivation and amusing greetings, Rahul for cheering all of us, Satish and Shashank for their interesting views about everything, Haridas for his inspiration, and Sourabh for his encouragement. I will miss everyone.

TABLE OF CONTENTS

LIST OF FIGURES

INTRODUCTION

An optical rectenna consists of an antenna coupled to a high-speed diode that rectifies high frequency electromagnetic radiation to DC (Corkish et al., 2002; Moddel and Grover, 2013; Yu et al., 2014). Rectennas were initially developed for microwave frequency detection and energy harvesting (Brown, 1973, 1969; Messenger and McCoy, 1957), used for optical detection (Elchinger et al., 1976; Hocker et al., 1968; Sanchez et al., 1978; Small et al., 1974), and proposed for solar energy harvesting in 1972 (Bailey, 1972). Over the last five decades, significant work has been done on developing rectennas for microwave energy harvesting (Hagerty et al., 2004; McSpadden et al., 1998; Yoo and Chang, 1992). Because microwave rectennas can achieve rectification efficiencies beyond 70% they have been considered as devices that, if used for solar energy harvesting, could surpass the Shockley-Queisser efficiency limit of solar cells (Corkish et al., 2002; Sarehraz et al., 2005; Shockley and Queisser, 1961a) to reach the thermodynamic limit of harvesting solar radiation 93% (Landsberg and Tonge, 1979), using low-cost materials and simple design (Bareiß et al., 2012) unlike multi-junction solar cells that are expensive. In this thesis, I study the performance limits of optical rectennas by applying the theory of photon-assisted tunneling to diodes in a rectenna circuit under monochromatic and broadband illumination.

Recently, Grover et al. (Grover et al., 2013) developed a detailed description of the operating principle of optical rectennas using the theory of photon-assisted tunneling (Dayem and Martin, 1962a; Tien and Gordon, 1963; Tucker, 1979; Tucker and Feldman, 1985). They show that at petahertz frequencies, the interaction of high-speed rectenna diodes with photons is quantized, and due to interaction with single photons, the resulting diode response is different from its classical response. In chapter I, I apply the theory of photon-assisted tunneling (PAT) to a diode in a simple

rectenna equivalent circuit to calculate rectenna response. I use this method in chapter II to calculate the efficiency limits of broadband rectennas as solar cells and show that due to the finite spatial coherence of sunlight, the power conversion efficiency of solar energy harvesting by rectennas is limited to the Trivich-Flinn efficiency limit (Trivich and Flinn, 1955) of 44%. Rectennas can exceed this limit if they operate in the classical regime. I show that in chapter III, where I determine that classical operation of rectennas is applicable not only at microwave frequencies, but also at optical frequencies. Similarly, rectennas can operate quantum mechanically at microwave frequencies, depending on the input conditions. This demonstrates the correspondence between the classical and quantum operation of a rectenna and provides new ideas to design rectennas for exceeding the Trivich-Flinn efficiency limit.

A diode has to meet some important requirements for efficient rectification. Over the last few decades, several high-speed diodes, capable of rectifying optical frequencies have been used for optical rectennas. These include metal-insulator-metal (MIM) diodes (Choi et al., 2011; Cowell et al., 2011; Eliasson, 2001; Eliasson and Moddel, 2003a; Grossman et al., 2002; Grover and Moddel, 2012a; Miskovsky et al., 2012; Sanchez et al., 1978), traveling wave diodes (Estes and Moddel, 2007; Grover et al., 2010a; Hobbs et al., 2007), geometric diodes (Moddel et al., 2012; Zixu Zhu et al., 2014; Zhu et al., 2013a, 2013b), and sharp-tip diodes (Miskovsky et al., 2012, 1980). The devices are capable of rectifying waves up to 100 THz. Several diode issues such as the *RC* time constant, impedance matching with the antenna, and diode reverse leakage affect the performance of a rectenna (Grover and Moddel, 2011). In chapter IV, I present guidelines to improve the performance of double insulator MIM (MIIM) diodes for high frequency energy harvesting. I use the theory of PAT to calculate the power conversion efficiency of the MIIM diodes under illumination from a monochromatic source, taking the reverse leakage, impedance matching, and

RC time constant issues into account. These requirements are important for efficient rectenna operation, but are often ignored in literature.

Since the calculation of rectenna response using PAT involves solving a non-linear electrical circuit and is time-consuming, in chapter V, I develop a simple figure of merit to estimate the power conversion efficiency of a rectenna under illumination. The results correspond well with the PAT calculations and simplify rectenna analysis. The purpose of this figure of merit is to quickly estimate, for a set of input conditions, the conversion efficiency of MIM diodes published in literature without need for elaborate calculations.

In chapter VI, I present my work on the design and characterization of single insulator Ni/NiO/Ni MIM diodes for detection of 1 THz radiation. In chapter VII, I discuss the measurement of the optical response of rectennas using geometric diodes for 28 THz detection. I conclude the thesis with a summary and suggestions regarding future work on energy harvesting using rectennas.

CHAPTER I

HOW TO ANALYZE OPTICAL RECTENNA RESPONSE

A. Chapter summary

Optical rectennas, antenna-coupled diode rectifiers that receive optical-frequency electromagnetic radiation and convert it to DC output, have been proposed for use in harvesting electromagnetic radiation from a blackbody source. The operation of these devices is qualitatively different from that of lower-frequency rectennas, and their design requires a new approach. To that end, I present a method to determine the rectenna response to high frequency illumination. It combines classical circuit analysis with classical and quantum-based photon-assisted tunneling response of a high-speed diode. I demonstrate the method by calculating the rectenna response for low and high frequency monochromatic illumination, and for radiation from a blackbody source. Such a blackbody source can be a hot body generating waste heat, or radiation from the sun.

B. Introduction

Recently, there has been a surge of interest in optical antennas connected to high-speed nonlinear diodes. Such systems, known as optical rectennas, have been investigated as optical and high-frequency detectors (Briones et al., 2013; Heiblum et al., 1978; Hoofring et al., 1989; Sanchez et al., 1978; Small et al., 1974), and for infrared and visible-light-frequency energy-harvesting (Eliasson, 2001; Yu et al., 2014; Moddel and Grover, 2013; Joshi and Moddel, 2013; Byrnes et al., 2014). They incorporate nano-antennas and high-speed diodes such as metal-insulator-metal and geometric diodes for high frequency rectification (Choi et al., 2011; Eliasson and Moddel, 2003b; Grover et al., 2010b; Krishnan et al., 2008; Miskovsky et al., 2012; Moddel et al., 2012;

Periasamy et al., 2013; Vandenbosch and Ma, 2012; Wilke et al., 1994; Zhu et al., 2013b). However, no simple method exists for analyzing rectenna performance at optical frequencies. In this chapter, I present a method to calculate the optical response and performance of a diode in an optical rectenna. The analysis presented here is different from the one in Grover et al. (2013), (Grover et al., 2013) which provides the fundamental physical concepts. Here, I apply those concepts to the electrical circuit theory of rectennas using equivalent electrical circuit analysis methods. The efficiency limits of rectennas have been developed using this approach in Joshi and Moddel (2013) and in chapter II (Joshi and Moddel, 2013).

To determine the response of the rectenna under optical illumination, I apply the theory of photon-assisted tunneling (PAT) to high-speed diode operation (Grover et al., 2013; Tien and Gordon, 1963), which cannot be explained using classical large-signal theory traditionally used for microwave rectenna analysis (Yoo and Chang, 1992).

The optical response of a rectenna depends on the performance of its components, which include an antenna, a diode, a low-pass filter, and a load, as shown in figure I-1. The antenna collects incident electromagnetic waves and generates an alternating current, which is rectified by a high-speed diode. A low-pass filter allows only rectified DC current to flow to the load. The load current can be used for detection or energy harvesting of electromagnetic radiation. When used for energy harvesting, the performance of the rectenna is determined by calculating the rectenna power conversion efficiency, which is the ratio of the DC output power across the load (P_{out}^{DC}) and the AC input power available at the antenna terminals (P_{in}^{AC}),

$$\eta = \frac{P_{out}^{DC}}{P_{in}^{AC}}. \tag{I-1}$$

The P_{out}^{DC} is the product of the rectified DC output current, which I refer to as the illuminated DC current (I_{illum}), and the DC output voltage, which is the operating voltage (V_O) of the rectenna (previously referred to as V_D in Grover et al. (2013) (Grover et al., 2013)).

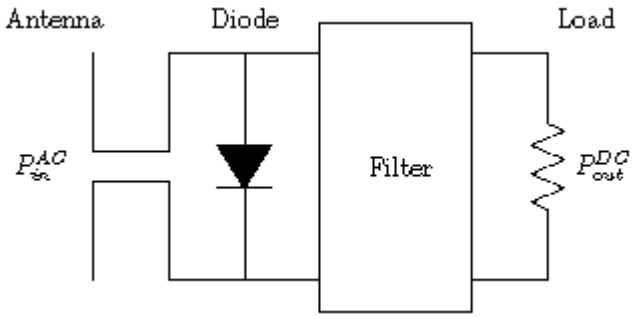

Figure I-1. General schematic of a rectenna. The input power available at the antenna is P_{in}^{AC}. The diode rectifies the AC signal to produce DC. The low-pass filter blocks the AC from being lost in the load. P_{out}^{DC} is the rectified DC output power provided to the load.

In the following sections I demonstrate a method to determine the optical response of the rectenna by applying the theory of PAT to a diode in an equivalent circuit, unifying the theory of PAT with conventional circuit analysis. I plot the illuminated *I(V)* characteristics, I_{illum} vs. V_O, under monochromatic and broadband illumination conditions.

C. Rectenna equivalent circuit

The optical rectenna can be modeled as the equivalent electrical circuit shown in figure I-2. The antenna is represented by a Thévenin-equivalent generator (an AC voltage source represented by $v_S = V_S \cos(\omega t)$) in series with the antenna input impedance, which at the resonant frequency is represented by the radiation resistance (R_S). The Thévenin-equivalent voltage across the antenna is a function of the input power (P_{in}^{AC}), and is calculated using the energy conservation principle as follows. When the antenna is connected to a matched resistive load and illuminated by a monochromatic source of angular frequency ω, maximum power transfer occurs between the

antenna and the load, such that P_{in}^{AC} is sent to the load without reflection. The peak value of the source voltage is calculated as,

$$V_S = \sqrt{8R_S P_{in}^{AC}} \ .$$

(I-2)

A capacitor *C* acts as the clamping capacitor for the rectenna circuit, in addition to modeling the fact that the antenna blocks DC. This results in an alternating voltage across the diode that is clamped by a DC voltage. In this way, the output DC voltage can rise to the AC peak voltage and, under ideal conditions, provide a rectification efficiency that approaches 100%. The DC clamp voltage across the capacitor is the operating voltage that appears across the load (Joshi and Moddel, 2013). The load is connected in parallel with the diode through a low-pass filter *L* to allow only DC to flow through the load and block the AC power from being dissipated in it.

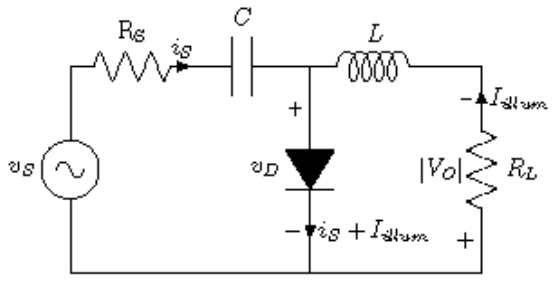

Figure I-2. Equivalent circuit of a rectenna. The antenna source voltage is v_S, and its equivalent radiation resistance is R_S. A capacitor *C* blocks the flow of DC current in the antenna circuit, and also provides voltage clamping. The inductor *L* forms a low-pass filter to block the AC power from being dissipated in the load. The AC current in the antenna circuit is i_S and the rectified DC current is I_{illum}. The total (AC plus DC) voltage across the diode is v_D and the total current through the diode is $i_S + I_{illum}$. The load resistance is R_L and the DC operating voltage across the load is V_O.("Note:," n.d.)

D. Procedure to calculate rectenna illuminated *I(V)* characteristics

In this section, I present the procedure to calculate the illuminated *I(V)* characteristics of the rectenna. The detailed method is presented in appendix A. Before analyzing the equivalent circuit

with a resistive load to determine the illuminated *I(V)* characteristics, I consider a simple case in which the load is a short circuit. This case illustrates and develops an understanding of how the rectenna generates a DC illuminated short-circuit current and works as a detector. Because the load has zero resistance, the operating voltage, equal to the clamping voltage across *C*, is zero, which simplifies the equivalent circuit. Kirchhoff's voltage law applied to the antenna-diode loop of the circuit gives the instantaneous voltage across the diode,

$$v_D(t) = v_S(t) - i_S(t)R_S \,.$$

(I-3)

The short-circuit mode results in the circuit of figure I-2, but with R_L replaced by a short. When a time-dependent voltage is applied to the diode, it produces an AC current that flows through the antenna circuit, and a DC current that flows as the short-circuit current (I_{SC}) through the diode-filter loop. The I_{SC} is the point that intersects the current axis on the illuminated *I(V)* characteristics of the rectenna.

When a non-zero resistance load is placed in the circuit, I_{illum} flows through the load and the DC voltage is

$$\left|V_O\right| = I_{illum}(V_O)R_L \,.$$

(I-4)

Since the V_O also appears across the capacitor *C* as the clamping voltage, the effect of the load resistance is to change the time-dependent voltage across the diode, which is now the sum of the operating voltage across the capacitor and an AC voltage:

$$v_D(t) = -\left|V_O\right| + v_S(t) - i_S(t)R_S \,.$$

(I-5)

To calculate the illuminated *I(V)* characteristics of the rectenna, I sweep over a range of values of V_O. The $v_D(t)$ and $i_S(t)$ cannot be solved directly for a given V_O and $v_S(t)$ since the diode current is a function of $v_D(t)$. Therefore, for a given V_O, Eq. I-5 is solved iteratively to determine $v_D(t)$ and $i_S(t)$ using the diode dark *I(V)* characteristics. The $v_D(t)$ is updated to a new value using Eq. I-5, and $i_S(t)$ is calculated again using the diode *I(V)* characteristics. The procedure is repeated until the time-series sum of the difference between the n^{th} and $(n+1)^{th}$ iterated values of $v_D(t)$ is a small fraction (0.001) of the maximum amplitude of $v_S(t)$.

To determine the relation between $i_D(t)$ and $v_D(t)$, I use either classical or PAT theory (Tien and Gordon, 1963). For classical large-signal analysis, the diode current is calculated using the diode dark *I(V)* characteristics,

$$i_D(t) = I_{dark}[v_D(t)]\,.$$

(I-6)

However, classical analysis of the rectenna does not take into account the quantization effect of the high energy photons on the electronic states in the diode, and is therefore appropriate only when (Hamilton and Shapiro, 1970)

$$V_D \gg \hbar\omega/q.$$

(I-7)

V_D is the amplitude of the AC voltage across the diode. On the other hand the quantum regime requires PAT theory and occurs at optical frequencies when

$$V_D < \hbar\omega/q.$$

(I-8)

In PAT theory, using the diode dark *I(V)* characteristics and the diode voltage, the diode current is calculated as generalized by Tucker (Tucker, 1979),

$$i_D(t) = \iint d\omega' W(\omega') I_{dark}\left(\omega' + \frac{qV_O}{\hbar}\right) e^{-i\omega' t} d\omega'' W(\omega'') e^{-i\omega'' t} .$$

(I-9)

Here, the integration is over the range of incident frequencies represented by ω. The W is the phase factor described in (Tucker, 1979) and is the result of modulation of the Fermi level in the diode metal contact due to an applied time-dependent perturbation $v_D(t)$. The W is related to the diode voltage through its Fourier transform,

$$\int_{-\infty}^{\infty} d\omega' W(\omega') e^{-i\omega' t} = \exp\left\{-i\frac{q}{\hbar}\int^{t} dt' \left[v_D(t')\right]\right\} .$$

(I-10)

The average of $i_D(t)$ is the current I_{illum} that flows through the load and results in a DC output power,

$$P_{out}^{DC} = \left|V_O\right| I_{illum}(V_O) .$$

(I-11)

In the energy harvesting mode of the rectenna, the direction of I_{illum} in the diode corresponds to that under positive bias. Since the diode generates DC power, V_O is negative and power is produced where the plots of V_O vs. I_{illum} are in the second quadrant of the diode $I(V)$ characteristics (Grover et al., 2013), as illustrated in figure I-3. In the next sections, I use the procedure detailed above to calculate the optical response and the illuminated $I(V)$ characteristics of rectennas under monochromatic and broadband illumination.

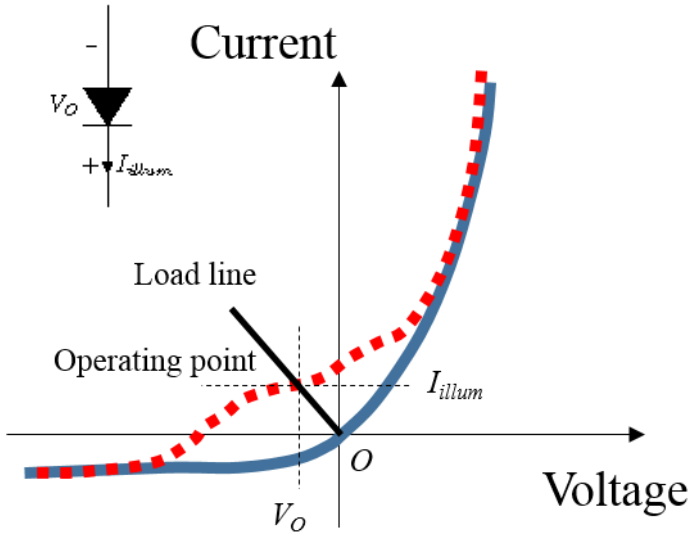

Figure I-3. Illustration of the illuminated I(V) characteristics of the diode in a rectenna. The solid blue curve represents the dark *I(V)* characteristics of the diode and the dotted red curve represents the illuminated *I(V)* characteristics. The inset shows the sign of positive I_{illum}, corresponding to a diode dark current under positive bias, and the sign of V_O, which is negative. In this mode, the diode generates DC power in the second quadrant of the diode *I(V)* characteristics. The load line intersects the illuminated *I(V)* curve at the operating point, and the load resistance is chosen to maximize the power delivered to it.

E. Optical response of the rectenna under monochromatic illumination

To demonstrate the method described above, I calculate the optical response of a rectenna under monochromatic illumination, with a diode having the piecewise linear *I(V)* characteristics shown in figure I-4(a). The forward resistance of the piecewise linear diode is 50 Ω and the reverse leakage current is zero. Such an *I(V)* has a semi-classical "secant resistance" (Grover et al., 2013; Joshi and Moddel, 2013) of 100 Ω at a V_O of 0 V, where the secant resistance is the reciprocal of the slope of the line connecting points on the *I(V)* curve at $\pm\hbar\omega/q$ about V_O. This provides a match to an antenna impedance of 100 Ω at V_O = 0 V. To contrast classical and PAT results I calculate the response of this rectenna for two different situations that represent Eq. I-7 and I-8. For the purpose of defining the operating regime, since V_D is a dynamic quantity and changes with V_O, for simplicity I will use V_S as an approximation for V_D. For a piecewise linear diode with zero reverse

leakage, V_D can vary from $V_S/2$ to V_S depending on the diode forward resistance and V_O, and therefore V_S is a good approximation for V_D. I will show that PAT theory applies in both the situations, whereas classical theory applies only when $V_S \gg \hbar\omega/q$. Detailed calculations on comparing classical and quantum operation are presented in chapter III.

a. *Classical case: $V_D \gg \hbar\omega/q$*

In the first case, corresponding to Eq. I-7, the photon energy is 0.004 eV and the input power is 200 μW, resulting in a V_S of 0.4 V calculated using Eq. I-2. Knowing $v_S(t)$ and the diode $I(V)$ characteristics, I iteratively solve Eq. I-5 for different values of V_O using both classical and PAT theories to calculate $v_D(t)$ and $i_D(t)$. The P_{out}^{DC} and the conversion efficiency are calculated using Eq. I-11 and I-1 and the results are shown in figure I-4(b). The I_{illum} is maximum when the load is short circuited and decreases with an increase in $|V_O|$, approaching zero as $|V_O|$ exceeds the peak diode voltage amplitude. For the given conditions the rectenna conversion efficiency approaches a maximum of ~40% at a V_O of –0.15 V. The classical and PAT results overlap for $V_S \gg \hbar\omega/q$, verifying that classical analysis is valid.

In figures I-4(c) and I-4(d), I plot the time-dependent source voltage, diode voltage, and diode current for operating voltages of 0 V and –0.15 V, respectively, to show the effect of V_O on the rectenna response. In Figure I-4(c) the peak value of the source voltage is 0.4 V, and the $i_D(t)$ in the negative half of the AC cycle is zero, as is classically expected from the $I(V)$ characteristics. The average current over the full cycle gives I_{illum} and is the rectenna short-circuit current. Since $V_O = 0$ V, the output power is zero and the rectenna functions as a detector rather than for energy harvesting.

In figure I-4(d), V_O = –0.15 V and represents the case when a load is connected across the diode such that the rectenna conversion efficiency is maximum. Because the voltage across the diode is clamped at V_O, in contrast with figure I-4(c) the diode voltage and current are positive over a smaller portion of the AC cycle. The I_{illum} is positive and the rectenna generates DC power. However, since the effective AC resistance of the piecewise linear diode shown in figure I-4(a) increases as V_O becomes more negative, the result is a decrease in the power coupling efficiency between the antenna and the diode. Therefore, the overall conversion efficiency is limited to 40% at V_O = –0.15 V. But this efficiency can be improved by adjusting the diode *I(V)* characteristics to decrease the diode AC resistance and improve the coupling efficiency at the required operating point.

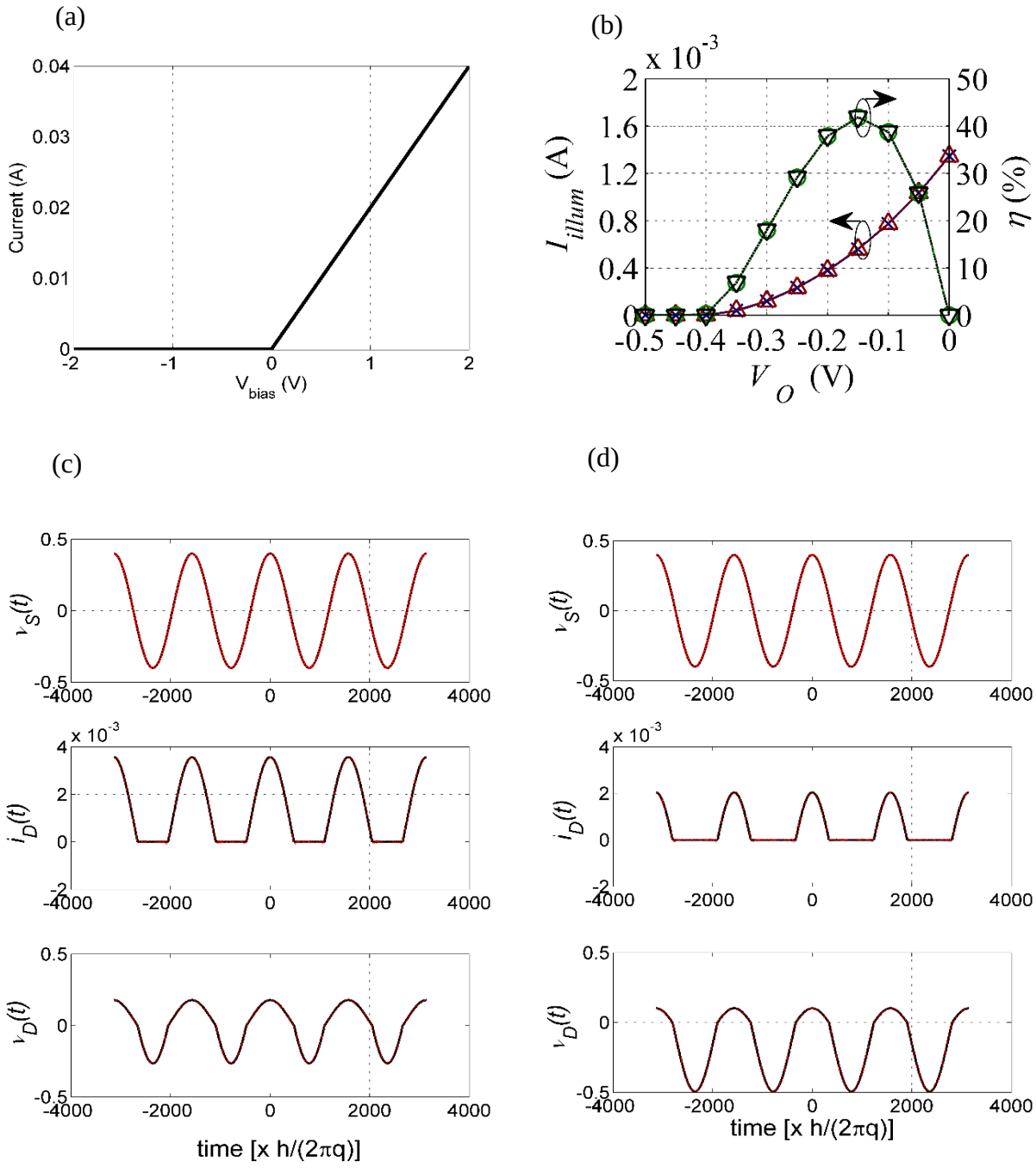

Figure I-4. Comparison of photon-assisted tunneling (PAT) and classical theory rectenna responses to low photon energy illumination (0.004 eV, corresponding to 310 μm) at two operating voltages, for an input power of 200 μW. (a) The dark *I(V)* characteristics of the piecewise linear diode having a forward resistance of 50 Ω and zero reverse leakage current. (b) The PAT illuminated *I(V)* (blue crosses) and conversion efficiency (green circles) characteristics of the

diode as a function of V_O. Also plotted are the classical illuminated *I(V)* (red triangles) and efficiency (black flipped triangles) characteristics, which coincide with the PAT results. This conversion efficiency is not the maximum efficiency of the rectenna, and can be improved using a diode *I(V)* that matches well with the antenna at $|V_O|$ close to V_S. Plots of $v_S(t)$, $i_D(t)$, and $v_D(t)$ were calculated using PAT theory (dotted red line) and classical theory (solid black) for (c) V_O = 0 V and (d) V_O = –0.15 V. The PAT and classical results superimpose under these conditions, and cannot be distinguished.

b. *Quantum case:* $V_D < \hbar\omega/q$

The quantum operation occurs when rectennas are illuminated with low intensity and high frequency radiation. Such a case corresponds to Eq. I-8, and is important in the analysis of rectennas as solar cells because radiation from the sun consists of low intensity but high energy photons. Here, I calculate the rectenna response under the conditions, $\hbar\omega/q$ = 4 V and V_S = 0.4 V, using the method presented in the previous section, and for the *I(V)* characteristics shown in figure I-4(a).

The rectenna illuminated *I(V)* and conversion efficiency characteristics are shown in figure I-5(a). The rectenna has a quantized step-like response that shows up as a hump in the illuminated *I(V)* characteristics. The I_{illum} is maximum when the diode is short-circuited, i.e., $|V_O|$ = 0 and the antenna and the diode AC impedances are matched, which results in electrons absorbing single photons and giving I_{illum}. As $|V_O|$ increases, the AC resistance of the diode increases and the impedance match between the antenna and the diode is poor, resulting in reduced power transfer between them and a gradual decrease in the I_{illum} (Joshi et al., 2013). When $|V_O|$ approaches $\hbar\omega/q$, the I_{illum} reduces to zero indicating that the photon energy is insufficient to assist electrons to tunnel through the diode and generate a current, in the same way as sub-bandgap energy photons do not contribute to the photocurrent in semiconductor solar cells. The resulting PAT maximum conversion efficiency is limited to ~48% at V_O = –2.6 V due to the mismatch in the antenna and diode impedance. However, for an ideal diode with an impedance that matches the antenna

impedance at $V_O = \hbar\omega/q$, the monochromatic conversion efficiency in the quantum regime ($V_D < \hbar\omega/q$) can approach 100%, as presented in reference (Joshi and Moddel, 2013).

Unlike the classical case, where the I_{illum} is expected to be non-zero up to the magnitude of ~V_S, the I_{illum} in the quantum case is non-zero up to ~$\hbar\omega/q$, which is greater than V_S. In addition, the response calculated using classical theory, shown in figure I-5(b), does not exhibit the quantum humps expected when $\hbar\omega/q$ is large relative to V_S. Therefore, classical theory gives incorrect results for the quantum case of $V_D < \hbar\omega/q$ and cannot be used for calculating rectenna response in that range.

In figures I-5(c) and I-5(d), I plot the $v_D(t)$ and $i_D(t)$, respectively, for V_O = 0 V and V_O where the rectenna conversion efficiency is maximum. In classical theory analysis, and as shown earlier in figures I-4(c) and I-4(d), the current in the negative half of the AC cycle is zero. As a result, the time-dependent waveforms have a DC term, a fundamental term, and multiple harmonics. In contrast, for these examples the PAT time-dependent waveforms have only significant DC and fundamental terms, with harmonics that are small compared to the fundamental. This is characteristic of the quantum regime of diode operation and is due to the absence of higher-order photon absorption terms, limiting higher frequency currents and voltages. In figure I-5(d), the time domain plots are shown for V_O = –2.6 V where the rectenna PAT conversion efficiency is maximum, and V_O = –0.15 V where the rectenna conversion efficiency calculated using classical theory is maximum.

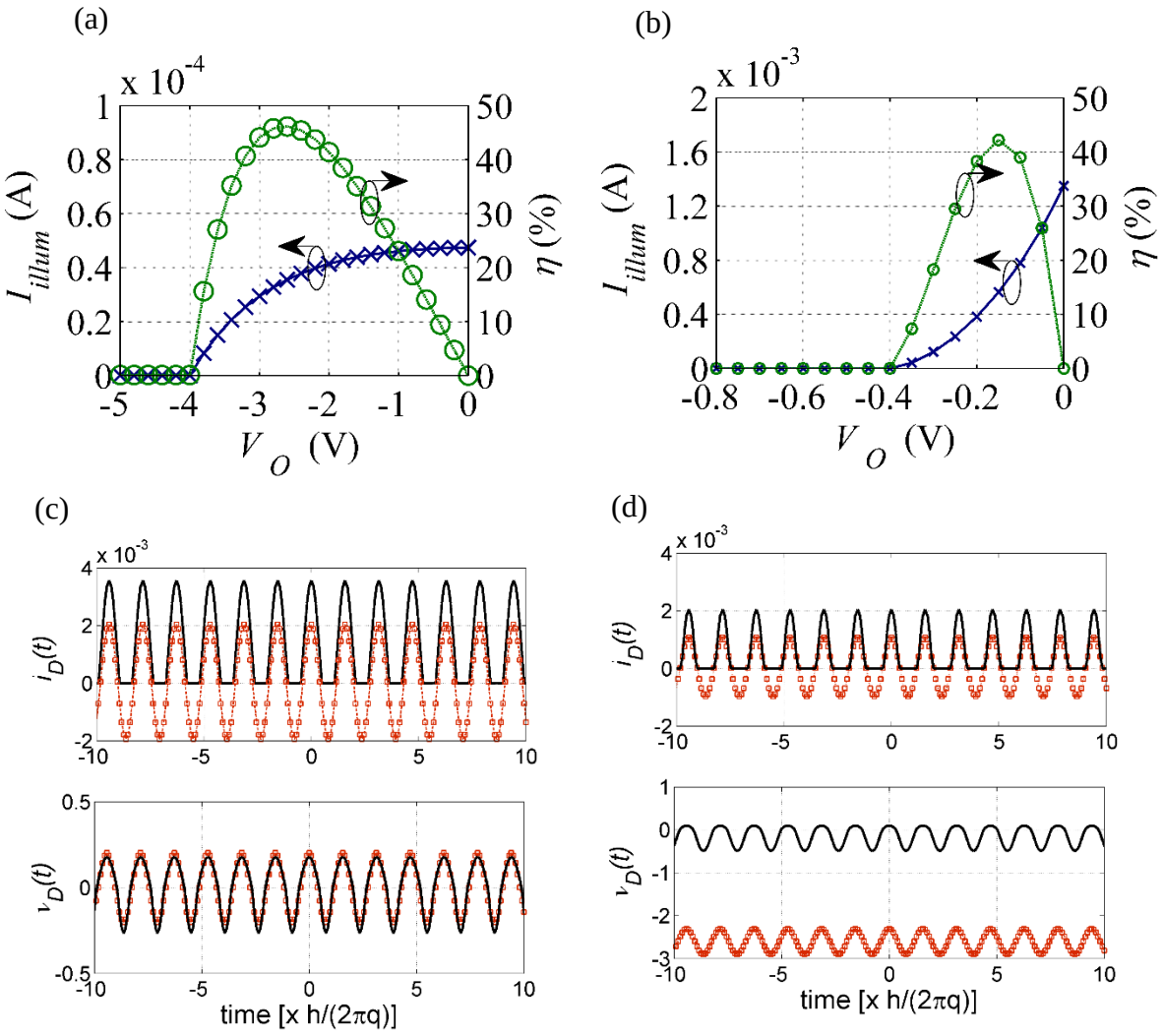

Figure I-5. Comparison of PAT and classical theory rectenna responses to high photon energy illumination (4 eV, corresponding to 310 nm), at two operating voltages for an input power of 200 μW. The diode *I(V)* characteristics are the same as in figure I-4(a). Illuminated *I(V)* (blue crosses) and conversion efficiency (green circles) characteristics calculated using: (a) PAT theory and (b) classical theory. Classical theory gives incorrect results for this quantum case where $V_D < \hbar\omega/q$. Also shown are plots of the time-dependent diode current ($i_D(t)$) and diode voltage ($v_D(t)$) calculated at (c) V_O = 0 V using both PAT (red circles) and classical theories (solid black) and at (d) V_O = –2.6 V for PAT theory and V_O = –0.15 V for classical theory. The average of the diode currents in (d) gives the rectenna I_{illum}, shown in (a) and (b), and the chosen values for V_O provide the maximum rectification conversion efficiency. This efficiency is not the ultimate efficiency of the rectenna in the quantum case, and can be improved using a diode that matches the antenna impedance at $|V_O| \sim \hbar\omega/q$.

F. Optical response under broadband illumination: Application to waste heat energy harvesting

The method shown above can be extended to determine the response of a rectenna to broadband sources, such as the sun or a hot blackbody. One application of rectennas is energy harvesting of waste heat from hot sources (Moddel, 2013), which I consider below.

A hot source radiates a broad electromagnetic spectrum that can be collected by a rectenna using a broadband antenna. It has been shown that an ideal broadband antenna with a wavelength-dependent area generates voltages with the spectral density of thermal noise across a hot resistor (Oliver, 1965; Yu et al., 2014). For simplicity, I assume that the impedance of the receiving antenna and its effective area is constant and independent of the frequency. A broadband antenna receiving this energy is represented by a source with a broad voltage spectrum whose shape may be approximated as the square root of the Planck blackbody spectrum. Using the inverse Fourier transform, I convert the frequency spectrum of the source voltage to the time domain (Joshi and Moddel, 2013). The phase distribution for the different frequency components is random and generated as normally distributed pseudorandom numbers. This randomly varying time-dependent voltage is such that the power delivered to an impedance-matched load resistance is equal to the antenna input power. I use Eq. I-4 through I-9 to determine the response of the rectenna to broadband illumination.

In figure I-6 I show the response of the diode to illumination from a hot body source of temperature 800 K. The input power from the source at the antenna terminals is assumed to be 1 μW. The spectrum ranges from photon energies of 0.01 eV to 4 eV and peaks at ~0.2 eV. The input power and the resulting source voltage is low such that the diode operates in the quantum regime and as a result, it responds to each frequency component individually in the absence of

higher order harmonics. As in a semiconductor solar cell, all photons with energy less than $q|V_O|$ do not tunnel through the diode and are unused, whereas photons with energy greater than $q|V_O|$ generate current at V_O and are used only partially. Therefore, the conversion efficiency of the rectenna peaks at V_O = –0.12 V and is limited to ~33 %.

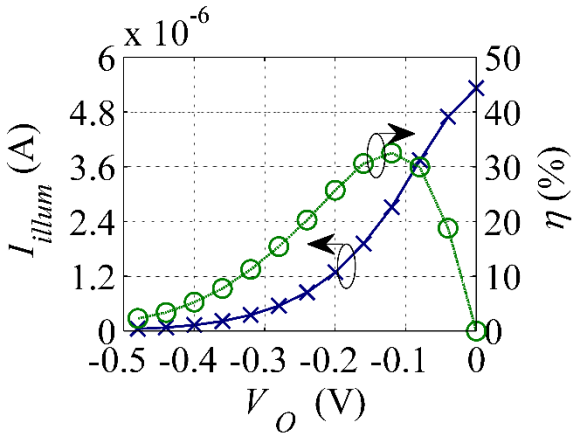

Figure I-6. Broadband illuminated *I(V)* and conversion efficiency characteristics of the diode in a rectenna calculated using PAT theory. The source is a blackbody of temperature 800 K, the input power to the rectenna is 1 μW, and the diode *I(V)* characteristics are the same as in figure I-4(a). The I_{illum} (blue crosses) and conversion efficiency (green circles) calculated using PAT theory are shown as a function of V_O. The maximum conversion efficiency is ~33 % for this diode *I(V)* and input conditions, and can be improved further using an *I(V)* characteristic that matches the antenna impedance at a negative operating voltage.

In this chapter, I concentrate on the method of analyzing the response rather than the ultimate power conversion efficiency of the rectenna and hence do not use a perfectly matched diode for the analysis. The theoretical efficiency can be improved by using a diode *I(V)* characteristic that matches well with the antenna impedance at the required V_O, as in reference (Joshi and Moddel, 2013) and chapter II. In practice, however, the diode will have a finite reverse leakage current, a finite capacitance, and a turn-on voltage greater than 0 V. In addition, the power from the blackbody source will also be limited at the rectenna due to the finite coherence area of blackbody

radiation at a nearby surface (Mashaal and Gordon, 2013). These constraints will result in a reduction in the conversion efficiency of the rectenna.

G. Conclusion

In this chapter, I described the procedure to calculate the illuminated *I(V)* characteristics of rectennas. I analyzed the response of rectennas in the energy harvesting mode using a simple equivalent circuit, and solved for the time-dependent diode current and voltage using both photon-assisted tunneling (PAT) and classical theories. I used the diode *I(V)* to calculate the illuminated *I(V)* characteristics of the rectenna under monochromatic illumination and broadband illumination such as that from a hot body source. The monochromatic illumination results show that classical theory cannot be used to calculate the rectenna response when the photon energy is high and the flux is low, corresponding to $V_D < \hbar\omega/q$. Here an accurate calculation requires a PAT analysis, which incorporates the quantum operation of the rectenna through discrete steps in the illuminated *I(V)* characteristics.

CHAPTER II

EFFICIENCY LIMITS OF RECTENNA SOLAR CELLS

A. Chapter summary

Because rectifiers can convert a wide range of frequencies to DC power it was thought that rectenna solar cells, antennas coupled to ultra-high speed diodes, could efficiently harvest the entire solar spectrum. I show that there are limits to broadband optical conversion, and provide a quantitative analysis of the efficiency limits of rectenna solar cells using the theory of photon assisted tunneling. This quantum-mechanical approach is different from classical rectification that occurs for lower frequency rectennas. I show that the conversion efficiency approaches 100% for monochromatic illumination. For broadband illumination at terrestrial solar intensities, the diode operating voltage plays the role that bandgap plays in conventional solar cells. Hence, using every available photon optimally produces a result much like, but potentially higher than the Shockley-Queisser efficiency limit for conventional solar cells.

B. Introduction

Optical rectennas have been proposed for harvesting solar energy as an alternative to conventional semiconductor photovoltaic devices (Bailey, 1972). In contrast to optical rectennas, conventional solar cells have a bandgap that constrains their conversion efficiency to the Shockley-Queisser limit (Shockley and Queisser, 1961b). I examine the response of optical rectennas to broadband blackbody radiation. To explain the operation of optical rectennas under multispectral illumination I use the theory of photon-assisted tunneling (PAT) (Tien and Gordon, 1963).

PAT theory and experiments have been investigated for superconducting junctions used as photon detectors (Dayem and Martin, 1962b; Tucker, 1979). For these devices, semi-classical (quantum) behavior comes into play when the photon energy divided by the electron charge ($\hbar\omega/q$) becomes large compared to the voltage at which significant nonlinearity appears in the diode current-voltage [*I(V)*] characteristics (Tucker and Feldman, 1985). I apply PAT theory to metal insulator metal (MIM) diodes, which have been investigated for solar rectennas (Berland, 2003; Corkish et al., 2002; Eliasson, 2001; Goswami et al., 2004; Grover and Moddel, 2012b), but the same approach can be applied to other diodes operating at optical frequencies (Grover, 2011).

The theoretical conversion efficiency of microwave rectennas used in harvesting narrow and broadband radiation can be high. At such low frequencies and high input intensities the device operating voltage is much larger than $\hbar\omega/q$ and the behavior may be treated classically, as shown in chapter I. However, at the low intensities of solar radiation and large $\hbar\omega/q$, comparable to the onset of significant nonlinearity in the diode DC *I(V)* characteristics, nonlinear effects lead to a significant change in the physics used to describe device operation. I address here how this limits the broadband efficiency.

Considering the theoretical conversion efficiency as the DC power produced as a function of AC electrical power dissipated by the diode (Yoo and Chang, 1992) results in misleadingly high efficiency values. Instead, I consider the conversion efficiency as a function of the radiant power incident at the antenna, which includes coupling losses from the antenna to the diode. I choose diode characteristics that provide ideal load matching, which limits the diode rectification characteristics but avoids the much larger losses due to poor power coupling.

C. Calculation of the efficiency limits

To calculate conversion efficiency under broadband illumination, I select the power equivalent to one sun incident on the earth's surface (i.e., 1000 W/m^2). If the current collected by each diode includes components that are out of phase with each other, cancellation and power loss results. Therefore the maximum power supplied to each diode is limited by the area over which the solar radiation is coherent. The coherence efficiency is defined as the coherent power intercepted by the antenna relative to the total incident power (Grover, 2011; Mashaal and Gordon, 2011). For a coherence efficiency of 90% this area corresponds to a radius of ~19 μm. The maximum power coupled to the antenna is then calculated to be approximately 1.1×10^{-6} W. I consider the ideal case where the capacitance of the diode is sufficiently small so that there is no *RC* falloff at the optical frequencies of interest. I do not investigate antenna efficiency limits, which are analyzed elsewhere (Vandenbosch and Ma, 2012).

I use the procedure detailed in chapter I. In PAT, microwave radiation gives rise to a DC tunneling current that occurs in voltage steps of $\hbar\omega/q$ (Dayem and Martin, 1962b), producing an increase in the tunneling current at voltages below the knee of the dark *I(V)* curve. This is equivalent to sampling the DC *I(V)* curve at voltage steps of $\hbar\omega/q$ (Tien and Gordon, 1963). Mathematically, the above statement is written as,

$$I_{illum} = \sum_{n=-\infty}^{\infty} J_n^2\left(\frac{qV_D}{\hbar\omega}\right) \times I_{dark}(V_O + n\frac{\hbar\omega}{q}).$$

(II-1)

Where I_{illum} is the illuminated DC current with photon energy $\hbar\omega$, V_D is the amplitude of the AC voltage across the diode, V_O is the DC operating voltage, I_{dark} is the diode DC dark current, and J_n corresponds to the Bessel function of order n. At low intensities and high frequencies

corresponding to solar radiation, the Bessel terms are significant only for $n = -1$, 0 and 1, because the argument $qV_D/\hbar\omega$ is small. The interpretation is that electrons are available for tunneling across the barrier at energies of one photon energy higher and lower than the Fermi level and the initial state itself. The occupation of these states is governed by the corresponding Bessel terms, which are a function of the source intensity and the photon energy.

I illustrate the process in figure II-1 for a diode with piecewise-linear characteristics and negligible reverse leakage currents. In a rectenna diode having a sufficiently low positive turn-on voltage, there is an increase of the tunneling current in the second quadrant of the *I(V)* characteristics, providing rectification and power generation.

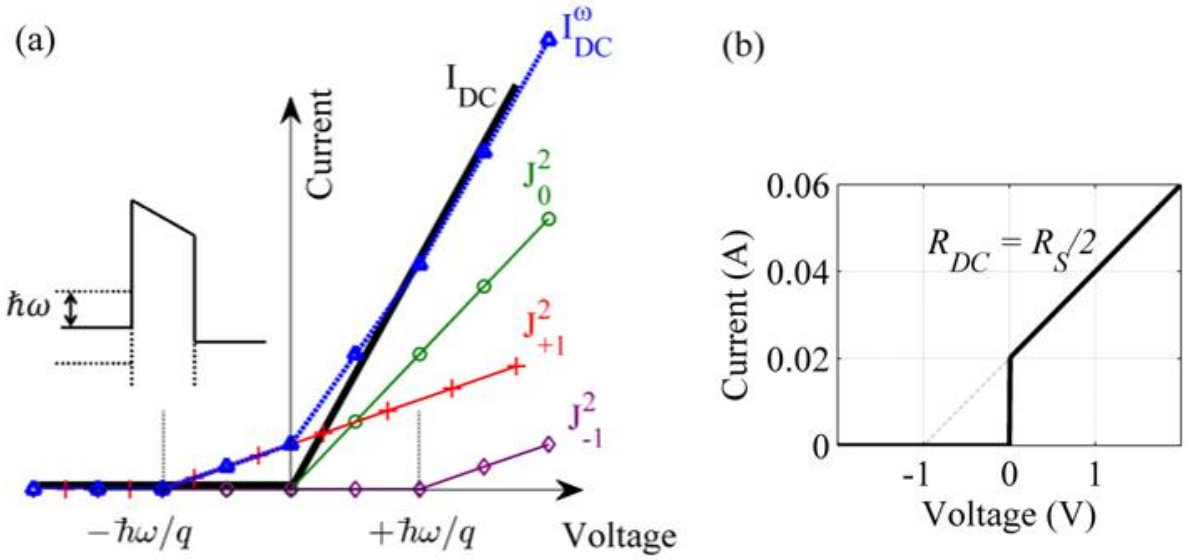

Figure II-1. Illustration of photon-assisted tunneling in a diode and the ideal diode I(V) characteristics. (a) *I(V)* characteristics showing the effect of photon-assisted tunneling (PAT) under illumination. The dark *I(V)* characteristics are represented by the black solid line. Tunneling currents are produced by photon absorption (red pluses) and emission (purple diamonds), for a photon energy of $\hbar\omega$. The combination of these currents produces the DC tunneling current (blue triangles). The inset illustrates the energy band diagram of a typical MIM diode under DC bias. (b) Diode *I(V)* characteristics (solid black) for optimal matching to an antenna. The x-axis intercept is the operating voltage V_O, and the reciprocal of the slope of the *I(V)* (i.e., R_{DC}) is set to half the antenna impedance (R_S).

It can be inferred from figure II-1(a) that a high reverse resistance is required to minimize the leakage currents and increase the power output in the second quadrant. I assume a diode that has negligible reverse leakage. The presence of source resistance requires impedance matching with the diode for maximum power transfer. The impedance offered by the diode to an input at a particular photon energy is the reciprocal of the slope of a secant between two points on the *I(V)* curve, one photon energy above and below the V_O (Grover and Moddel, 2011). This impedance R_D is

$$R_D = \frac{2\times(\hbar\omega/q)}{I(V_O+\hbar\omega/q)-I(V_O-\hbar\omega/q)} \approx \frac{2\times(\hbar\omega/q)}{I(V_O+\hbar\omega/q)} = \frac{2\times(\hbar\omega/q)}{m\times(-|V_O|+\hbar\omega/q)+b}. \quad \text{(II-2)}$$

For $m=1/R_{DC}$ and $b=|V_O|/R_{DC}$, I obtain $R_D=2R_{DC}$.

Thus, to perfectly match the diode and the antenna at a particular V_O, the required *I(V)* is such that its first quadrant differential resistance R_{DC} is half the antenna impedance and an extrapolation of the *I(V)* intercepts on the x-axis at V_O, as shown in figure II-1(b). This is not a realistic resistance characteristic, but instead is used to find the maximum theoretical conversion efficiency that can be obtained.

D. Efficiency for monochromatic illumination

I use the method presented in chapter I to calculate the rectenna conversion efficiency. For monochromatic illumination of the rectenna, since there is optimal power transfer all incident power is coupled to the diode. In the quantum limit, there is one electron per incident photon, i.e., unity quantum efficiency (Tucker and Feldman, 1985). My simulation produced this current maximum at $qV_O = \hbar\omega/q$, as shown in figure II-2(a), giving a power conversion efficiency of

100%. The current drops to zero when the voltage exceeds this because the PAT no longer provides sufficient energy to surmount the barrier.

This result shows that for a carefully engineered diode a rectenna operating under monochromatic illumination approaches unity power conversion efficiency. This opens the way for applications in room-temperature terahertz sensing and detection, and high frequency power transfer and conversion applications.

At high input intensities or low frequencies, multiple steps appear in the *I(V)* due to higher order and mixed excitations. As the intensity increases or the frequency decreases further the results approach the classical expression for large signal rectification (Hamilton and Shapiro, 1970), in agreement with the correspondence principle and as shown in chapter III. However, at low intensity and high frequency limits the quantum approach of PAT is required.

E. Solar spectrum rectification

To understand the rectification process for the solar spectrum I first consider the case of illumination at two different frequencies ω_1 and ω_2. Under this condition, the distribution of electrons is still discrete but gives rise to states at energies $\hbar\omega_1/q$ and $\hbar\omega_2/q$, and sum and difference energies $\hbar(\omega_1+\omega_2)/q$ and $\hbar(\omega_1-\omega_2)/q$ due to mixing. As with the higher order terms in the monochromatic case, higher order mixing occurs at high input intensities and low input frequencies, giving rise to multiple sum and difference combinations of the two. The time-dependent voltage across the barrier in the simplest case of two-frequency illumination is given as,

$$V(t) = V_O + V_1\cos(\omega_1 t) + V_2\cos(\omega_2 t) \tag{II-3}$$

In Eq. II-3, V_1 and V_2 are the voltage amplitudes across the diode at the two frequencies ω_1 and ω_2. I derive the expression for the illuminated DC current following Tucker's approach,

$$I_{illum} = \sum_{n=-\infty}^{\infty}\sum_{m=-\infty}^{\infty} J_m^2\left(\frac{qV_1}{\hbar\omega}\right) J_n^2\left(\frac{qV_2}{\hbar\omega}\right) \times I_{dark}(V_O + m\frac{\hbar\omega_1}{q} + n\frac{\hbar\omega_2}{q}) \,. \tag{II-4}$$

In Eq. II-4, m and n are the photon absorption or emission numbers for the two different frequencies.

The simulated *I(V)* curves for illumination at two frequencies, corresponding to photon energies of 1 eV and 1.5 eV, is shown in figure II-2(b). The calculations were performed using the method presented in chapter I. Steps appear at qV_O equal to the photon energies. The conversion efficiency is lower than for the single frequency case because for smaller magnitude V_O the full photon energy of the higher energy photons is not used, and at larger magnitude V_O the lower energy photons do not contribute to the current.

A way to increase the power conversion efficiency is to channel the unused photons to higher energy states through higher order and mixing terms in Eq. II-4, which would give rise to non-zero current at operating voltages of less than -1.5 V. As seen in figure II-2(b) neither of these processes contribute significantly to the current-voltage characteristics at solar intensities because the occupation probabilities of the higher order and mixed states, as represented by the higher order Bessel terms in Eq. II-4, are significantly lower than the fundamental states. At high intensities photon stepping at these higher order and mixed energies is observed, as shown in figure II-2(c). In reality, however, rectennas cannot make use of a concentrated sunlight because of the coherence

limitation described earlier. Improving the *I(V)* characteristics would also increase the strength of the mixed states, but at the cost of a poorer impedance match with the antenna.

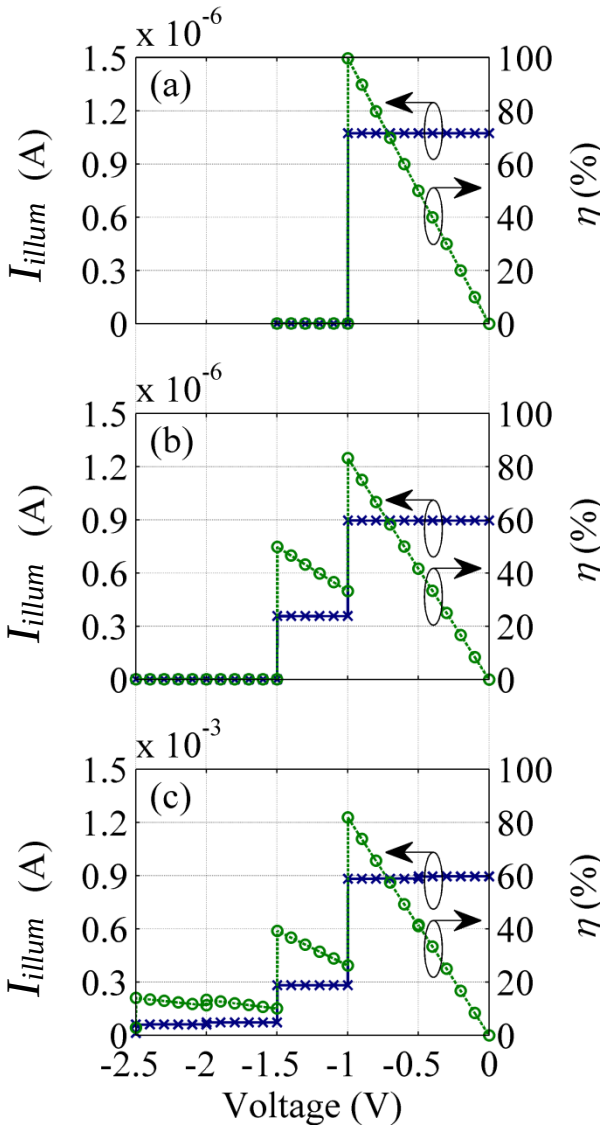

Figure II-2. Illuminated I(V) (blue crosses) and power conversion efficiency η (green circles) characteristics of the rectenna under monochromatic and two-frequency illumination. (a) Monochromatic illumination. The incident photon energy is 1 eV, and the input power is 1.1×10^{-6} W, corresponding to a solar power of 1000 W/m^2 over an area with a radius of ~19 μm. Rectenna efficiency approaches 100% when qV_O approaches $\hbar\omega$. (b) Two frequency illumination corresponding to photon energies of 1 eV and 1.5 eV for the same total input power. The voltage amplitude of the two sources is equal and the fraction of the number of low to high energy photons is 1.5:1. (c) Same as (b), with increased input power corresponding to 10^3 suns, showing the

appearance of tunneling current at high reverse operating voltages due to excitation of both higher order and mixing terms.

To analyze solar conversion efficiency I model the solar spectrum as a blackbody at 5780 K, and consider the maximum terrestrial input power (P_{in}) of 1.1×10^{-6} W. I use Rayleigh's theorem (Riley et al., 2006) to calculate the source voltage spectrum ($v_S(t)$) received by an antenna illuminated by the blackbody source. I assume a constant antenna impedance of 100 Ω. The power dissipated in an antenna matched load is P_{in}. I calculate the resulting voltage developed across the diode ($v_D(t)$) using the method presented in chapter I. The diode current and conversion efficiency under multispectral illumination is calculated, as shown in figure 3.

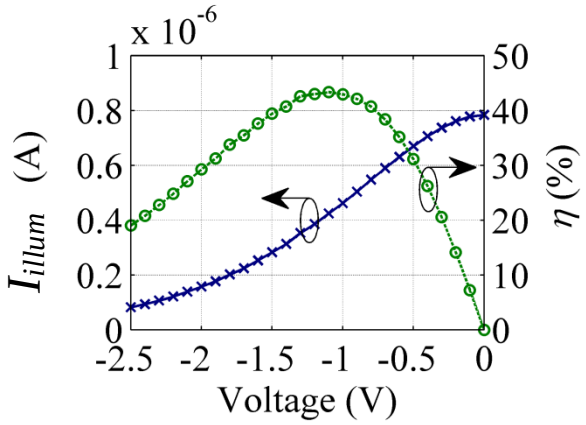

Figure II-3. Illuminated *I(V)* (blue crosses) and conversion efficiency (green circles) characteristics of the diode for an ideal rectenna under solar blackbody illumination at 5780 K. The input power is 1.1×10^{-6} W. This is the maximum power available due to coherence issues, as described in the text. The diode dark *I(V)* characteristics have a shape like that shown in figure II-1(b), but with a slope and intercept designed for optimal power coupling from the antenna for each operating voltage. The maximum conversion efficiency is ~44%.

The maximum power conversion efficiency of ~44% is produced at an operating voltage of 1.1 V. This result is reminiscent of the Shockley-Queisser ultimate efficiency for devices having bandgap cutoff. With rectenna solar cells, operating voltage qV_O plays the role that bandgap plays

in conventional solar cells, so that only photons having an energy equal to qV_O are used optimally. Lower energy photons are wasted and the energy of higher energy photons is only partially used. Under the conditions employed here, I obtain virtually no advantage from mixing and higher order terms, due to the low input intensity. This maximum conversion efficiency is higher than the Shockley-Queisser (Shockley and Queisser, 1961b) limit of 33%, which is reduced from 44% due to the finite temperature of the cell and radiative recombination in the diode. In this chapter, I have not included these effects, which require device thermodynamic analysis (Markvart, 2007), nor limits imposed by the antennas. As with multi-gap conventional solar cells, the conversion efficiency of rectenna solar cells can be increased with the use of spectral splitting and rectenna solar cells at different operating voltages. Because spectral splitting with rectennas does not require materials matched to each spectral range, rectenna solar cells have an inherent advantage in this process.

The maximum conversion efficiency I found is limited because there are no mixing or higher order terms at solar terrestrial intensity. In contrast, microwave rectennas make use of substantial mixing of low energy photons, and attain higher conversion efficiencies.

Although the optical rectenna results were developed here for the case of metal-insulator-metal diodes, the same semiclassical characteristics are expected for other diodes types operating at optical frequencies (Grover, 2011).

F. Conclusion

In this chapter I explored the efficiency limits of rectenna solar cells. I developed the calculations based on the theory of photon assisted tunneling (PAT) and showed that, for diodes that are optimally matched to antennas, monochromatic power conversion efficiencies approach

100% and the multispectral conversion efficiency is limited to 44% at solar terrestrial intensities. Spectral splitting can improve the conversion efficiency, and can be accomplished simply by setting the operating voltage for each rectenna to rectify the desired spectral range.

CHAPTER III

OPTICAL RECTENNA OPERATION: WHERE MAXWELL MEETS EINSTEIN

A. Chapter summary

The analysis of rectennas is carried out either classically using Maxwell's wave-like approach, or quantum-mechanically using Einstein's particle-like approach for electromagnetic radiation. I analyze the correspondence between the two approaches by comparing rectenna response first to monochromatic illumination obtained using photon-assisted tunneling theory and classical theory. Applied to broadband rectenna operation, this correspondence provides clues to designing a rectenna solar cell that has the potential to exceed the 44% quantum-limited conversion efficiency. The comparison of operating regimes shows how optical rectenna operation differs from microwave rectenna operation.

B. Introduction

At radio and microwave frequencies, rectennas are analyzed using classical circuit analysis (McSpadden et al., 1998), governed by Maxwell's electromagnetic wave theory. In contrast, the operation of rectennas (Corkish et al., 2002; Moddel, 2013; Yu et al., 2014) at optical frequencies is fundamentally different from their low frequency response and is described using the theory of photon-assisted tunneling (PAT) (Grover et al., 2013), where the quantum interpretation of photon absorption by an electron follows Einstein's particle-like approach to electromagnetic radiation. One consequence of the quantum nature of the rectification is to limit the broadband solar conversion efficiency to 44% (Joshi and Moddel, 2013), which is the Trivich-Flinn quantum efficiency limit (Joshi et al., 2013; Trivich and Flinn, 1955).

Here I apply PAT theory for tunnel junctions to a rectenna equivalent circuit and demonstrate three different regimes of operation: classical, quantum, and a transition regime. I use the method presented in chapter I to determine rectenna response under different conditions to show the regimes of operation. I apply the results to suggest a rectenna design and setup that has the potential to exceed the 44% conversion efficiency limit by shifting the operation to the classical regime.

C. Operating regimes of the rectenna

The rectenna operates in one of the three regimes based on the amplitude of the diode AC voltage (V_D) relative to the photon energy divided by the electronic charge ($\hbar\omega/q$), with this ratio denoted by the parameter α. Since V_D is a dynamic quantity and changes with the operating voltage (V_O), for simplicity I will use the source voltage (V_S) as an approximation for V_D. For a piecewise linear diode with zero reverse leakage, V_D can vary from $V_S/2$ to V_S depending on the diode forward resistance and V_O, and therefore α_S is a good approximation for α. The three regimes, sketched in figure III-1, are

a. Quantum regime: $\alpha_S < 1$
b. Transition regime: $\alpha_S \sim 1$
c. Classical regime: $\alpha_S \gg 1$

In the following, I analyze rectenna operation under monochromatic illumination in each of the three regimes, with the goal of understanding the characteristics in each regime. To make the differences easily discernable, I use the following assumptions in my calculations: the diode dark *I(V)* characteristics (I_{dark}) may be approximated with a piecewise linear curve with zero reverse leakage current and a forward resistance (R_f) of 50 Ω such that its secant resistance (Grover et al., 2013) at $V_O = 0$ is 100 Ω, R_S is 100 Ω to roughly match the impedance of free-space, the diode

capacitance is negligible so that the rectification is not *RC*-time-constant limited, the diode is at 0 K and does not produce thermal noise, and the antenna efficiency is unity.

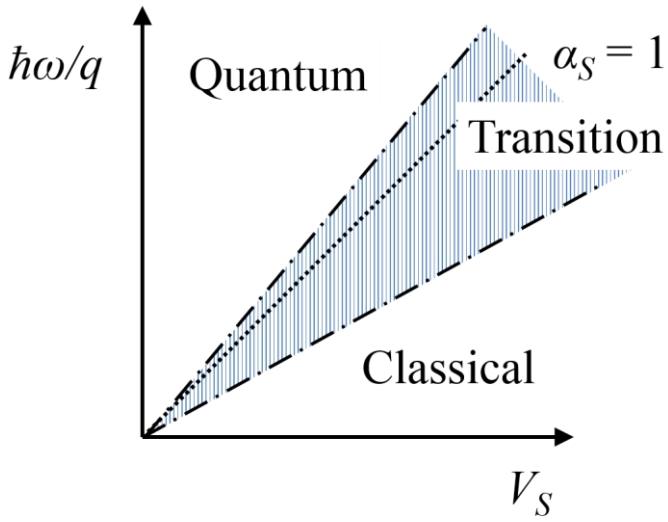

Figure III-1. Sketch of the operating regimes of a rectenna as a function of the source voltage ($V_S = \sqrt{8P_{in}R_S}$) and the photon energy divided by the electronic charge ($\hbar\omega/q$). Classical operation occurs when $V_S \gg \hbar\omega/q$, whereas quantum operation occurs when $V_S < \hbar\omega/q$. The ratio of V_S to $\hbar\omega/q$ is α_S, and the hatched blue area around the $\alpha_S = 1$ line (dotted line) is the transition regime.

a. Quantum regime ($\alpha_S < 1$)

The rectenna operates in the quantum regime when $\hbar\omega/q > V_S$ according to PAT theory, and electrons can absorb only individual photons. For $\alpha_S < 1$ the I_{illum} is quantized and results in discrete steps in the illuminated *I(V)* characteristics. I can simplify and average the expression in Eq. I-9 to express I_{illum} as (Grover et al., 2013),

$$I_{illum} = \sum_{n=-\infty}^{\infty} J_n^2\left(\frac{qV_D}{\hbar\omega}\right) \times I_{dark}(V_O + n\frac{\hbar\omega}{q}).$$

(III-1)

Here n is the number of photons absorbed or emitted by an electron in the diode. For small $qV_D/\hbar\omega$, the Bessel terms in Eq. III-1 are significant only for $n = -1$, 0, and 1. Therefore, the I_{illum} depends on I_{dark} at discrete voltages $\hbar\omega/q$ above and below the V_O [which is also the reason that the previously mentioned secant resistance [(Grover et al., 2013)] is a function of the secant between two points on the $I(V)$]. The resulting diode current responsivity is,

$$\beta = \frac{q}{\hbar\omega}\left\{\frac{I_{dark}(V_O+\hbar\omega/q)-2I_{dark}(V_O)+I_{dark}(V_O-\hbar\omega/q)}{I_{dark}(V_O+\hbar\omega/q)-I_{dark}(V_O-\hbar\omega/q)}\right\}. \tag{III-2}$$

For asymmetric tunnel diodes where [$I_{dark}(V_O+\hbar\omega/q-I_{dark}(V_O) \gg I_{dark}(V_O)-I_{dark}(V_O-\hbar\omega/q)$], the diode current responsivity approaches $q/\hbar\omega$ (Tucker, 1979), which means that for each incoming photon at most one electron tunnels through the barrier. A high-speed and sufficiently asymmetric diode can detect single photons in weak optical signals, but for $V_O \leq -\hbar\omega/q$ the rectified current drops to zero, as is evident in the following two sets of figures.

Using the method outlined in the previous section, I calculate the response of the diode in a rectenna under different input conditions to demonstrate its operation in the quantum regime. The three cases correspond to small α_S (~0.1, 0.05, and 0.03) and different incident frequencies (0.1 eV, 0.2 eV, and 1 meV). With change in frequency, the P_{in} has to be adjusted in each case so that the rectenna is in the quantum regime. I choose two different frequencies to show that the response is frequency dependent (shown in figures III-2(a) and III-2(b) for 0.1 eV and 0.2 eV), and quantum operation of the rectenna is not limited to infrared (IR) and optical frequencies, but also applies at microwave frequencies (shown in figure III-2(c) for 1 meV) for very low input powers. Since $\alpha_S < 1$, the rectenna operates in the quantum regime and the results follow the qualitative argument

presented above, i.e., electrons absorb photons when $|V_O| < \hbar\omega/q$ to generate a photocurrent which decreases to zero as $|V_O| \geq \hbar\omega/q$. As a result, in the quantum regime current is produced only when V_O is within $\hbar\omega/q$ of the origin, and therefore photons cannot used to generate current at voltages greater than $\hbar\omega/q$.

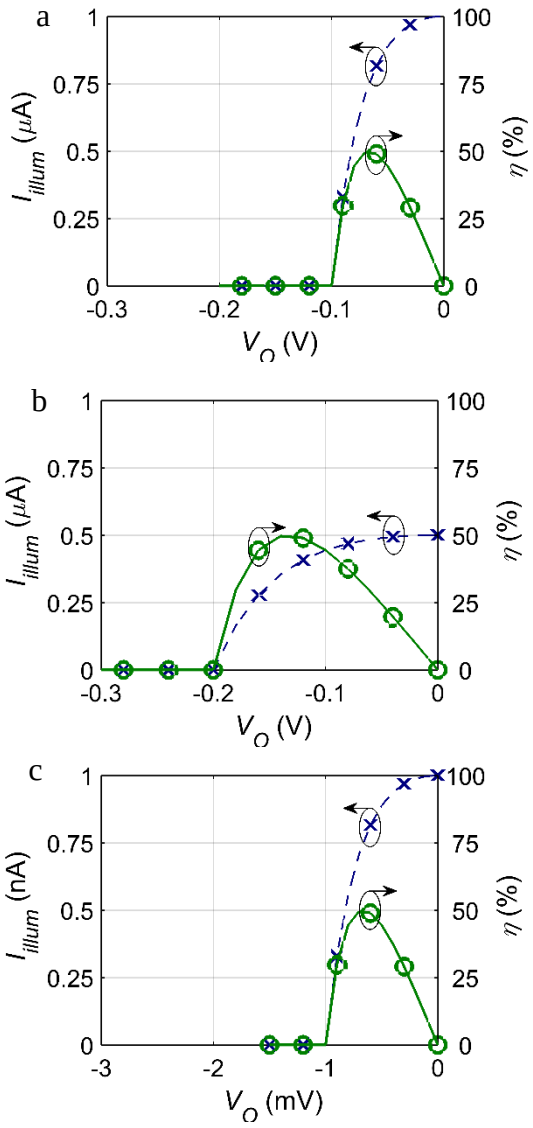

Figure III-2. Quantum regime *I(V)* (blue crosses) and conversion efficiency (green circles) characteristics of a rectenna under monochromatic illumination, to show the response of the rectenna at infrared (IR) frequencies, and at microwave frequencies for low input power. The diode

I(V) characteristics are piecewise linear with a forward resistance of 50 Ω and zero reverse leakage. Quantum operation of the rectenna at (a) Incident photon energy $\hbar\omega$ = 0.1 eV for small α_S ~ 0.1 (P_{in} = 100 nW), (b) $\hbar\omega$ = 0.2 eV for small α_S ~ 0.05, (P_{in} = 100 nW). (c) $\hbar\omega$ = 1 meV for small α_S ~ 0.03 (P_{in} = 1 pW) showing quantum operation of the rectenna at microwave frequencies for very low input powers. Unlike classical theory where the response is independent of frequency, the I_{illum} is frequency dependent and is non-zero for $|V_O| < \hbar\omega/q$.

b. Transition regime (α_S ~ 1)

As the V_S exceeds $\hbar\omega/q$, electrons absorb multiple photons and the rectenna operates in the transition regime. Here the discrete nature of the illuminated *I(V)* is maintained, but starts approaching the classical response. The discrete behavior is seen in the form of steps in the illuminated *I(V)* that occur at integer multiples of $\hbar\omega/q$. In figure III-3, I plot the rectenna response for α_S ~2.8 and $\hbar\omega$ = 0.1 eV. As $|V_O| > 0.1$ V, electrons that absorb single photons have insufficient energy to generate a photocurrent, and the contribution of these electrons (called the first-order photon absorption term, corresponding to n = 1 in Eq. III-1) to I_{illum} reduces to zero. The second-order absorption (electrons absorbing two photons) continues to contribute to the I_{illum} up to V_O = −0.2 V, which results in a second step in the illuminated *I(V)*. As the $|V_O|$ is increased, the successive higher order absorptions give a step-like behavior. The shapes of conversion efficiency plots in these figures exhibit the characteristics of each regime. Their magnitudes depend upon the particular illumination intensities and diode parameters, and are not by themselves significant.

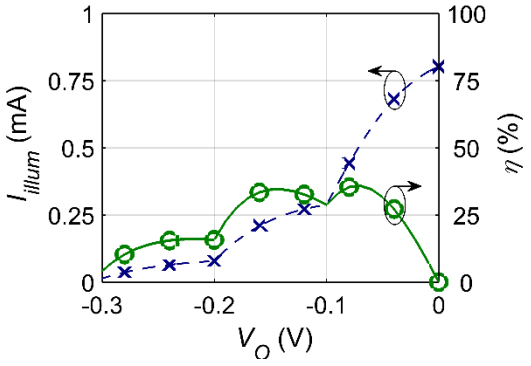

Figure III-3. Transition regime *I(V)* (blue crosses) and conversion efficiency (green circles) characteristics of a rectenna operating under monochromatic illumination for the diode of Figure III-2, showing discrete steps at integer multiples of $\hbar\omega/q$. The $\hbar\omega$ is 0.1 eV and the P_{in} is 100 μW, giving $\alpha_S = 2.8$. The steps in the I_{illum} at $V_O = -0.1$ V and $V_O = -0.2$ V are due to the second and third-order photon absorptions resulting in a non-zero current for $V_O < -0.1$ V and $V_O < -0.2$ V.

c. Classical regime ($\alpha_S \gg 1$)

When $V_S \gg \hbar\omega/q$ each electron absorbs many photons. Electron excitations occur at multiple energies, such that the PAT response of the diode to illumination is essentially equal to the classical response. On applying these limits, the expression for I_{illum} in Eq. III-1 reduces to the classical form (Hamilton and Shapiro, 1970; Joshi et al., 2013),

$$I_{illum} = \frac{1}{\pi}\int_{-\pi/2}^{\pi/2} I_{dark}\left(V_D + V_\omega \sin\theta\right) d\theta \,. \tag{III-3}$$

Shown in figure III-4(a) is the rectenna response at microwave frequencies ($\hbar\omega$ = 1 meV), as in figure III-2(c), but at a higher P_{in} of 1 μW, which results in classical operation. As I will show for the case of broadband illumination, classical operation provides significant advantages for conversion efficiency if it can be attained at higher frequencies. The classical response can occur at optical and IR wavelengths, but requires large V_S, which can be achieved in two ways: increasing the input power, and increasing the source and diode impedances.

a. *Increasing the input power:* A large voltage across the antenna results in a large voltage across the matched diode. In figure III-4(b), I plot the illuminated *I(V)* characteristics of the rectenna for P_{in} = 10 mW, and $\hbar\omega$ = 0.1 eV, resulting in α_S = 28. The PAT and classical results are virtually identical to each other.

b. *Increasing the source impedance*: Increasing the R_S results in a larger V_S for the same input intensity, according to Eq. I-2, but a large R_S requires a high impedance diode for good impedance match. An R_S = 1 MΩ, R_f = 500 kΩ, P_{in} = 1 μW, and $\hbar\omega$ = 0.1 eV results in the same α_S as in (a), above, and the illuminated *I(V)* characteristic of the rectenna approaches the classical result, as shown in figure III-4(c). (In reality, such large resistances would result in far too large an *RC* time constant for optical frequency rectification, but may be acceptable for microwave rectennas.)

In the three cases shown in figure III-4, I_{illum} is a smooth function of the V_O and decreases to zero as the V_O exceeds the amplitude of the v_D. The discrete steps in the I_{illum} that were evident for the quantum case are not noticeable even as the frequency approaches 30 THz.

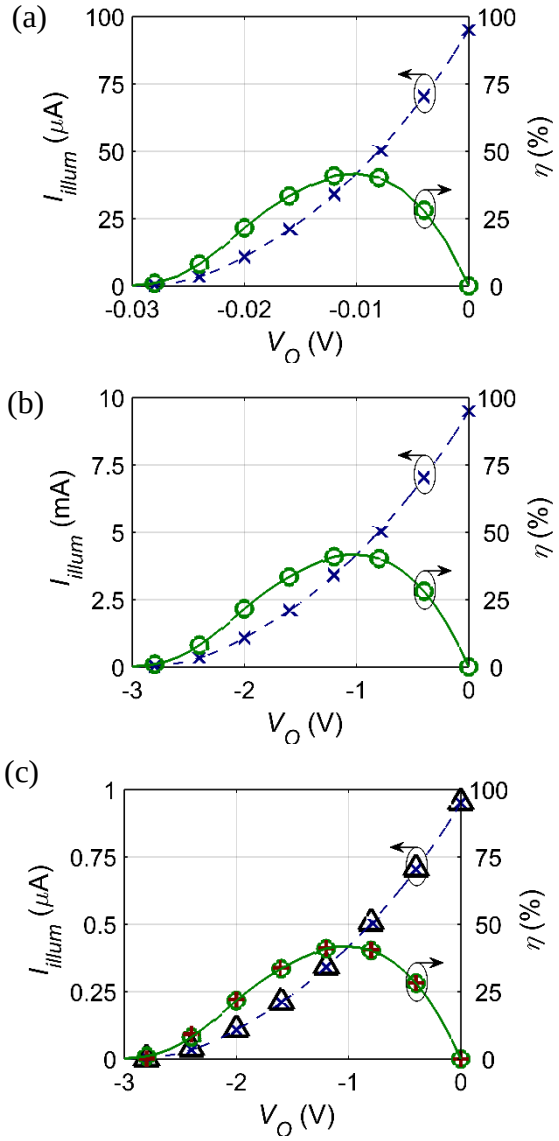

Figure III-4. Classical regime *I(V)* (blue crosses) and conversion efficiency (green circles) of a rectenna operating under monochromatic illumination, calculated using PAT theory under different input conditions, such that the $V_S \gg \hbar\omega/q$. The diode has piecewise linear *I(V)* with zero reverse leakage. (a) As expected at microwave frequencies, when the P_{in} is high so that $V_S \gg \hbar\omega/q$, (1 µW with $R_f = 50\ \Omega$ and $\hbar\omega = 1$ meV) the response is classical. The two ways to achieve large V_S compared to $\hbar\omega/q$ resulting in classical operation at IR frequencies ($\hbar\omega = 0.1$ eV) include, using (b) large $P_{in} = 10$ mW (with $R_f = 50\ \Omega$, $R_S = 100\ \Omega$), and (c) large $R_S = 1$ MΩ ($R_f = 500$ kΩ, and $P_{in} = 1$ µW). Also plotted are the illuminated *I(V)* (black triangles) and conversion efficiency (red pluses) characteristics calculated using classical theory, showing that the classical theory and PAT theory results are identical in the classical regime. Although not shown, the same applies to results in (a) and (b).

The maximum conversion efficiency of the rectenna under monochromatic illumination in the classical case is lower than the conversion efficiency in quantum regime because of the additional power loss in the higher order harmonic currents generated due to multiphoton absorption, as in the transition regime. However, the classical regime can have a positive effect on the conversion efficiency of harvesting broadband radiation because low energy photons of different frequencies mix and excite electrons to higher energy levels, and used at higher operating voltages. The absence of such mixing in the quantum rectification of low intensity broadband solar radiation limits the maximum conversion efficiency to 44%, as was shown in reference (Joshi and Moddel, 2013).

D. Application to broadband rectification

To demonstrate that broadband rectenna operation in the classical regime results in a higher conversion efficiency of rectification compared to the quantum regime, I calculate the rectenna response to blackbody illumination under different operating conditions. In my calculations, I choose the temperature of the blackbody and two different conditions such that the rectenna operates in classical and in quantum regimes. I confirm classical rectenna operation under high V_S by comparing the PAT response with the response calculated using classical theory. Then I compare the ultimate efficiency of the rectenna in the quantum regime with its conversion efficiency in the classical regime for varying diode resistances and show that the classical regime can be more efficient.

I use a 3D blackbody spectrum of temperature 600 K. Values for P_{in} and R_S are large enough (P_{in} = 100 μW, R_S = 10 kΩ) that the resulting V_S (rms) is high relative to the $\hbar\omega/q$ at which the peak in the blackbody spectrum occurs (~0.15 eV), and therefore the rectenna operates in the

classical regime. Comparing results calculated from PAT theory to the I_{illum} and η calculated using classical theory shows that the two results superimpose each other, as in figure III-5(a), confirming that the input conditions are appropriate for classical operation of the rectenna.

The quantum regime occurs when the P_{in} and R_S are such that the V_S (rms) is low compared to the peak $\hbar\omega/q$ of the blackbody spectrum, and is shown in figure III-5(b) (for P_{in} = 100 nW, R_S = 100 Ω). The resulting range of V_O over which rectenna operates is smaller than in the classical regime, and the electrons are used at $V_O \sim \hbar\omega/q$ to generate current. Therefore, the conversion efficiency of quantum operation is expected to be lower than classical operation. The peak conversion efficiency (η_{peak}) is 37.5% and is lower than the classical η_{peak} of 42%.

The low conversion efficiency in the broadband quantum regime could be due to a poor impedance match between the antenna and the diode. To remove the effect of impedance matching, I calculate the ultimate rectenna efficiency for an ideal diode that is matched with the antenna at every V_O (Joshi and Moddel, 2013). I found the maximum conversion efficiency in this quantum regime case to be ~ 44% for solar radiation (Joshi and Moddel, 2013), and the maximum efficiency number is the same for radiation from a blackbody of any temperature. I compare this ultimate efficiency with the classical η_{peak} vs. the R_f, calculated using classical theory, showing in figure III-5(c) that the operation of broadband rectennas in the classical regime can exceed the quantum-limited efficiency. The η_{peak} decreases with increasing R_f due to decreasing impedance match with the antenna, but is greater at small R_f than the ultimate conversion efficiency in the quantum regime.

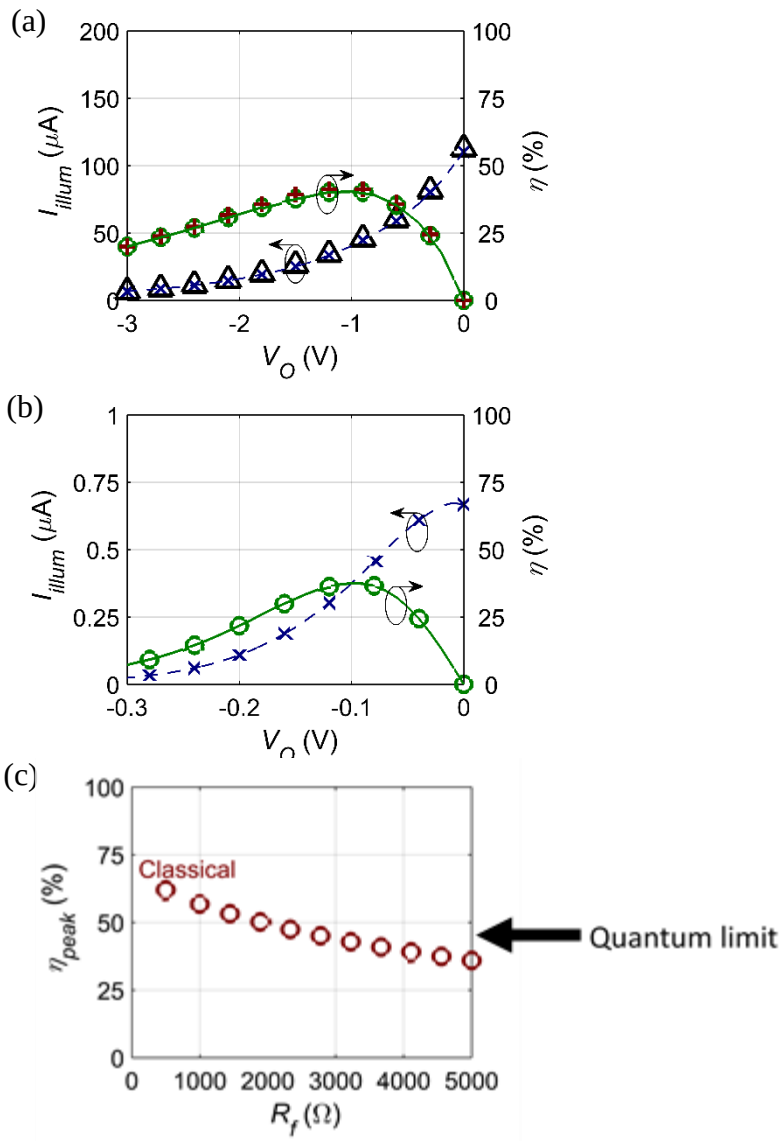

Figure III-5. Comparison of classical and quantum operation for rectennas under broadband illumination from a blackbody of temperature 600 K, showing *I(V)* (blue crosses) and conversion efficiency (green circles) characteristics. The diode is a piecewise linear diode with zero reverse leakage current. (a) Classical operation of the rectenna occurs at large P_{in} and R_S (when P_{in} = 100 μW, R_f = 3 kΩ, and R_S = 10 kΩ) giving high V_S (rms) compared to the $\hbar\omega/q$ at which the blackbody spectrum peaks, and the results superimpose over the classical theory results (red pluses and black triangles). The peak conversion efficiency (η_{peak}) is 42%. (b) Quantum operation of the rectenna occurs at small P_{in} = 100 nW and R_S = 100 Ω (R_f = 30 Ω). The rectenna operates efficiently over a smaller range of V_O compared to the classical case and the resulting peak conversion efficiency is lower at 37.5%. (c) Variation of the peak conversion efficiency (η_{peak}) of the rectenna (red circles), calculated using classical theory, with change in the diode R_f. Broadband classical operation is more efficient than quantum operation of the rectenna where the ultimate conversion efficiency is 44%.

Despite the improvement in the theoretical conversion efficiency for classical operation of the rectenna compared to quantum operation, there are practical challenges of operating the rectenna in the regimes of figures III-5(a) and III-5(c), especially for sources with low intensity and high frequency radiation such as the sun. A drawback of increasing the R_S is an increase in the rectenna *RC* time constant and a decrease in the coupling efficiency (Grover and Moddel, 2011; Sanchez et al., 1978). In addition, increasing the radiation resistance of the antenna is an engineering challenge. However, designs such as the traveling-wave diode (Grover et al., 2010a; Hobbs et al., 2007), geometric diode (Zhu et al., 2013b; Z. Zhu et al., 2014), and the sharp tip configurations (Miskovsky et al., 2012) mitigate the effect of the *RC* time constant and can potentially be used together with this technique.

A second problem that limits the increase in V_S is the diode breakdown voltage. MIM diodes, used in rectennas for high frequency rectification, work on the principle of electron tunneling through nanometer-scale thin oxides (Alimardani and Conley, 2013; Choi et al., 2011; Cowell et al., 2011; Grover and Moddel, 2012a; Krishnan et al., 2008; Periasamy et al., 2011). The breakdown strength of oxides is of the order of 1 MV/cm (McPherson et al., 2003), resulting in a breakdown voltage of 1 V across a 10 nm thick tunneling layer. This makes harvesting of high frequency solar radiation difficult, because classical operation requires $V_S \gg \hbar\omega/q$.

The third problem is the limited spatial coherence of radiation from blackbody sources (Mashaal and Gordon, 2013, 2011). Since input intensities are low and the radiation from blackbodies is coherent only over small areas, the rectenna must be small and receives only enough optical power to operate in the quantum regime, such that the resulting conversion efficiency of energy harvesting is limited (Joshi and Moddel, 2013).

For these three reasons achieving classical operation of rectennas for energy harvesting of high temperature blackbody radiation is a challenge, and new solutions are required for rectennas to exceed the Trivich-Flinn (Trivich and Flinn, 1955) efficiency limit.

E. Conclusion

I investigated rectenna operation using the quantum theory of photon-assisted tunneling under different operating conditions. I found that there are different regimes of rectenna operation, from quantum to classical. Rectennas follow Einstein's photon-based approach if the diode voltage (V_D) is less than the photon energy divided by the electronic charge ($\hbar\omega/q$), and follow Maxwell's classical electromagnetic wave nature of light if $V_D \gg \hbar\omega/q$. The correspondence between classical and quantum operation of the rectenna in the limit of large V_D compared to $\hbar\omega/q$ allows classical operation at optical and IR frequencies for high incident intensity and for large source and diode impedances. This is useful to improve the conversion efficiency of broadband rectennas for harvesting blackbody radiation, including solar radiation, beyond the quantum limit. The conversion efficiency of solar rectennas can exceed the 44% limit for conventional semiconductor solar cells if classical operation can be achieved.

CHAPTER IV

DESIGN OF METAL/MULTI-INSULATOR/METAL DIODES FOR OPTICAL RECTENNAS

A. Chapter summary

Various high-speed metal-insulator-metal diodes have been investigated for harvesting solar radiation using rectennas. However, many of the diodes do not meet the impedance matching, asymmetry, and *RC* time-constant requirements for energy harvesting. Here I list crucial diode requirements often ignored in literature, propose diode design guidelines, and apply them to improve the current-voltage characteristics of metal/multi-insulator/metal diodes. I show that the diode performance can be improved but with limitations, and new designs are required for efficient harvesting of high frequency radiation.

B. Introduction

Optical rectennas are antenna-coupled diode rectifiers that convert high-frequency electromagnetic radiation to DC. They have been proposed for optical detection (Fumeaux et al., 1998; Hoofring et al., 1989; Heiblum et al., 1978) and energy harvesting in the infrared (IR) (Corkish et al., 2002; Moddel, 2013) using high-speed diodes such as metal-insulator-metal (MIM) diodes (Elchinger et al., 1976; Eliasson, 2001; Grover and Moddel, 2012a; Small et al., 1974), geometric diodes (Zhu et al., 2013b; Z. Zhu et al., 2014), and other ballistic devices (Song, 2002) for rectifying the optical-frequency current (tens to hundreds of terahertz) generated in the antenna by the incoming radiation.

MIM diodes are attractive for rectennas due to their femtosecond fast operation and ease of fabrication (Bareiß et al., 2012; Grover and Moddel, 2012b; Small et al., 1974). Several novel diode designs have been proposed to enhance their AC to DC rectification efficiency (Choi et al., 2011; Grover et al., 2010a; Miskovsky et al., 2012). Despite this, rectennas and MIM diodes aimed at energy harvesting applications face several challenges (Yu et al., 2014). These challenges include improving the diode asymmetry with low turn-on voltage and reducing the reverse leakage current, keeping a short electron transit time, a short *RC* time-constant, and a good impedance match with the antenna (Grover and Moddel, 2011; Moddel, 2013).

In this chapter, I propose steps to improve the performance of double insulator MIM (MIIM) diodes (Alimardani and Conley, 2013; Eliasson, 2001; Grover and Moddel, 2012b), calculate their rectification efficiency under illumination, and discuss the potential challenges with their design and operation.

C. Rectenna diode requirements for energy harvesting

MIM diodes for rectennas have to meet several requirements for efficient energy harvesting and detection of radiation, and they must be designed accordingly. Rectenna diodes for energy harvesting operate in the second quadrant of the diode *I(V)* characteristics, and generate DC power with positive illuminated current (I_{illum}) and a negative operating voltage (V_O). A plot of I_{illum} vs. V_O, called the illuminated *I(V)* characteristics (see figure 1.2 in reference [(Moddel, 2013)]), intersects the load line at the operating point of the rectenna. The rectification efficiency (η) is calculated as,

$$\eta = \frac{|V_O| I_{illum}(V_O)}{P_{in}^{AC}} \qquad \text{(IV-1)}$$

Here P_{in}^{AC} is the AC input power at the antenna terminals.

Although the operation of optical rectennas is different from classical rectennas, they can be analyzed using a classical equivalent electrical circuit model, as explained in reference [(Joshi and Moddel, 2015a, 2013)] using the theory of photon-assisted tunneling (PAT) (Grover et al., 2013; Tien and Gordon, 1963; Tucker, 1979).

For efficient operation of an energy-harvesting rectenna, the diode must meet the following requirements:

a. Good impedance match with the antenna and short *RC* time constant: The power coupling between the antenna and the diode is maximum when the antenna radiation resistance and the diode AC impedance match each other. In addition, the rectenna *RC* time constant should be less than $1/2\pi f$ for good coupling efficiency, which is given as,

$$\eta_C = \frac{\frac{4R_S R_D}{(R_S + R_D)^2}}{1 + \left(2\pi f \frac{R_S R_D}{R_S + R_D} C_D\right)^2}. \quad \text{(IV-2)}$$

Here R_S is the radiation resistance of the antenna, R_D is the AC resistance of the diode at the V_O, and C_D is the diode capacitance.

b. High diode asymmetry and low reverse leakage current: The asymmetry of the diode around the V_O should be high to generate a photocurrent under illumination that is greater than the reverse leakage current of the diode at V_O. The reverse leakage current (I_{leak}) is such that,

$$I_{leak}(V_O) << \frac{P_{in}^{AC}}{V_O}.$$

c. Short electron transit time: The transit time of an electron through the diode should be less than the inverse angular frequency ($\omega = 2\pi f$) of the incoming wave, so that the electron can travel through the diode before the AC field reverses direction.

Diode requirements depend strongly on the input conditions. The intensity of radiation from hot blackbodies may be such that rectenna diodes either work in the quantum regime or the classical regime, depending on the diode voltage (V_D) relative to the photon energy divided by q ($\hbar\omega/q$) (Joshi et al., 2013; Joshi and Moddel, 2015b). From PAT theory applied to tunnel diodes in rectennas, when the P_{in} is such that V_D is less than the $\hbar\omega/q$, the rectenna operates in the quantum regime. On the other hand, when the V_D is much greater than $\hbar\omega/q$ the rectenna operates in the classical regime. The differences between classical and quantum regimes result in different diode resistance and responsivity values, and therefore different diode requirements. Some of the diode requirements have been discussed in references [(Grover and Moddel, 2011; Moddel, 2013)], and the effect of these on the rectenna response is analyzed in detail in reference [(Joshi and Moddel, 2015c)].

D. Diode designs

It is challenging to meet all the diode requirements using single-insulator MIM diodes (Grover and Moddel, 2011). In the following, I use resonant MIIM and step MIIM diode designs (Moddel and Eliasson, 2004; Grover and Moddel, 2012a; Maraghechi et al., 2012a; Alimardani and Conley, 2013), which are described below, and suggest ways to improve their performance. I compute the current density vs. voltage [*J(V)*] characteristics of these diodes using the method presented in reference [(Grover and Moddel, 2012b)] by solving the Schrodinger equation using the transfer

matrix method. To simplify understanding of the design concept, I do not take into account the effect of charge storage in the resonant wells (Cahay et al., 1987) or the effect of image forces on the shape of the potential barrier (Simmons, 1969), which affect the *J(V)* response of the device. These effects are small and can be reduced or compensated for by making small changes in the diode design.

The resonant MIIM diode, shown in figure IV-1(a), is a double insulator diode with a triangular potential well formed between the two insulators. For one bias polarity, a resonant state is formed in this potential well between the two barriers and provides enhanced *J(V)* characteristics. For the opposite bias polarity, the electrons tunnel through the insulators with a lower transmission probability due to a lack of a resonant state, resulting in a reduced current (Grover and Moddel, 2012b). The diode asymmetry, leakage current, and the turn-on voltage depend on the width of the insulators (d_1 and d_2), the barrier heights (ϕ_{b1} and ϕ_{b2}), and the position of the resonant well with respect to the metal Fermi energy levels.

The step MIIM diode has a step-like potential barrier formed by two insulators, as shown in figure IV-1(b) (Matsumoto et al., 1996). The first insulator (I_1) is thick, has a high relative permittivity (ϵ_{r1}), and forms a lower barrier height (ϕ_{b1}) with the metal. In contrast, the second insulator (I_2) is thin, has a lower relative permittivity (ϵ_{r2}), and forms a higher barrier height (ϕ_{b2}) with the second metal compared to ϕ_{b1}. When the diode is biased in either direction, the high contrast in the relative permittivity of the two layers leads to a small potential drop in I_1 and a greater potential drop in I_2, giving a large asymmetry to the diode design. In positive bias, when $V_b > \phi_{b1}$, electrons tunnel through I_2 and over the conduction band edge of I_1, giving large current density. In negative bias, electrons tunnel through both the barriers, resulting in a current that is small, but may still produce substantial leakage.

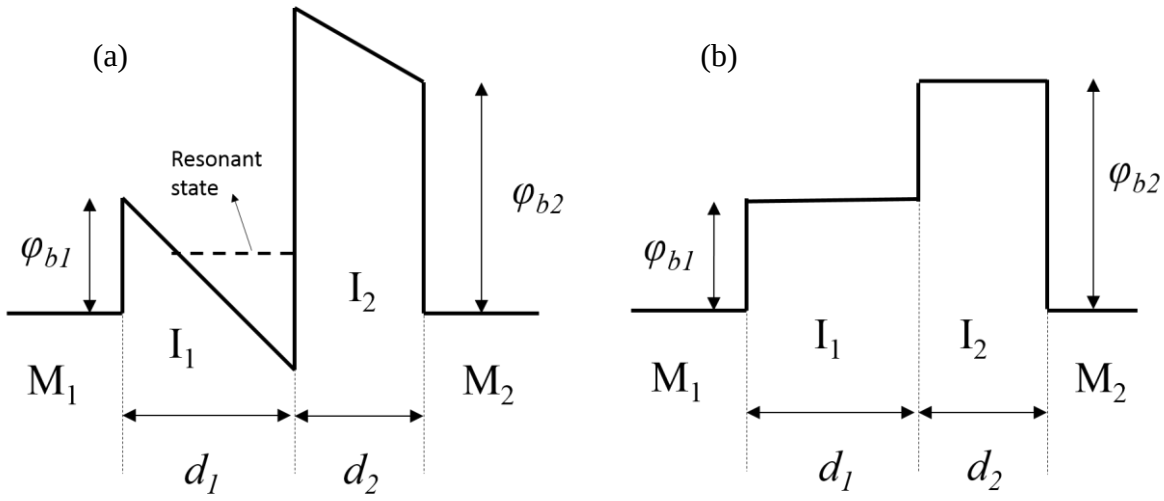

Figure IV-1. Illustration of the ideal energy-band diagrams of resonant and step MIIM diodes at zero bias. (a) Resonant MIIM diode and (b) Step MIIM diode, both with insulators I_1 and I_2 of thicknesses d_1 and d_2 and forming barrier heights ϕ_{b1} and ϕ_{b2} with the two metals M_1 and M_2. For the diode configuration shown here, a difference in the refractive indices of I_1 and I_2 in the two diode designs leads to their resonant ($\epsilon_{r1} \lesssim \epsilon_{r2}$) and step behavior ($\epsilon_{r1} \gg \epsilon_{r2}$). When biased, the resonant diode forms a potential well while the step diode does not, as explained in the text. The resonant state in the resonant MIIM is indicated by the dotted line in the triangular potential well formed between the two insulators. In this diode, a difference in the work functions of M_1 and M_2 (ϕ_1 and ϕ_2) results in a potential drop across I_1 and I_2 at zero bias. The diode characteristics such as the forward current density, turn-on voltage, and the reverse leakage current can be tuned by changing the device design parameters including oxide thicknesses, metal/insulator barrier heights, refractive indices, and the work functions of the two metal layers

E. Diode design guidelines

I use a starting set of diode parameters (ϕ_{b1}, ϕ_{b2}, d_1, d_2, $\epsilon_{r1}/\epsilon_{r2}$, and $\Delta\phi$) for the resonant diode and step diode, labeled as 'resonant' and 'step' diodes in figure IV-2. From this starting set of diode parameters, I follow a sequence of design steps and propose new resonant diodes (labeled 1A, 2A, and 3A) and new step diodes (labeled 1B, 2B, and 3B), and show a step-by-step improvement in the *J(V)* characteristics to increase diode asymmetry and reduce the reverse leakage current, compared to the initial diode set. The parameters used for modeling the diodes are listed in table IV-I.

1. If we need to increase the forward current density, it can be accomplished by increasing the electron transmission through the diode by decreasing the effective oxide thickness and increasing the width of the resonant states, compared to the initial diode set.
    a. Resonant MIIM diode: The forward-current density of the resonant MIIM diode is increased by increasing the width of the insulator forming the resonant well, and therefore increasing the number of resonant states in the potential well. In addition, decreasing the barrier height of the potential well increases the energy width of the resonant state resulting in enhanced current density. For example, in figure IV-2(a) I show the *J(V)* characteristics labeled 1A, for increased d_1 = 3 nm, and decreased ϕ_{b2} = 0.3 eV, resulting in ~17x enhancement in the current density at 0.2 V.
    b. Step MIIM diode: The diode forward current can be increased by decreasing d_2 and ϕ_{b2}, both of which increase the electron transmission through the insulator. The *J(V)* characteristics shown in figure IV-2(b) and labeled 1B, show a 15x increase in current density at 0.2 V, compared to the unadjusted diode.
2. If we need to decrease the reverse leakage current, it can be achieved by reducing the electron transmission through the diode, using a design with an absence of resonant states and a thick effective oxide compared to the initial diode set.
    a. Resonant MIIM diode: The reverse leakage current of the resonant MIIM diode is reduced by increasing d_2, which decreases the transmission probability through the insulator. In figure IV-2(a), I show the *J(V)* characteristics for increased d_2 = 2 nm, labeled 2A. The result is that the reverse leakage current decreases by ~40x but the forward current through the device also decreases, with the result that the diode asymmetry increases by only a factor of three.

b. Step MIIM diode: The reverse leakage current is reduced and the asymmetry increased by increasing the ratio $\epsilon_{r1}/\epsilon_{r2}$. This results in a smaller potential drop across I_1 when reverse biased and therefore an effectively thicker insulator for electron tunneling and a reduced current density. In figure IV-2(b), I show the variation of the diode response with a change in the ratio of the relative permittivity of the barriers from 5 to 100, labeled 2B. As the ratio increases, the leakage current decreases and the asymmetry of the device increases.

3. If the goal is to decrease the diode turn-on voltage, this can be accomplished with low barrier insulators and resonant states closer to the Fermi energy level in the metal layers, compared to the initial diodes.

   a. Resonant MIIM diode: A thick d_1 results in wider potential wells and a greater number of resonant states that are lower in energy compared to those in thin insulators, lowering the turn-on voltage of the diode in addition to increasing the forward current density. Another method to lower the turn-on voltage is to choose metals with work functions such that, at zero bias, the resonant state in the potential well is at the same energy as (or close to the energy of) the Fermi level in the metals. Changing the work function of M_2 so that there is a positive work function difference between the two metal layers ($\Delta\phi = \phi_1 - \phi_2 > 0$) results in a potential drop across the insulators and the formation of a triangular potential well at zero bias, thereby requiring a smaller applied bias voltage (compared to 2A) to turn the diode on. Another way to decrease the turn-on voltage is to have a higher potential drop in I_1 compared to I_2, using different refractive indices, which results in the formation of a potential well at lower bias voltages. As seen from the *J(V)* curve of the diode labeled 3A in figure IV-2(a), where a $\Delta\phi = 0.2$ eV and $\epsilon_{r1}/\epsilon_{r2} = 1/2$ are used as examples, the asymmetry

is greater than for 2A due to a greater increase in the forward current than the reverse current.

b. Step MIIM diode: The result of reducing ϕ_{b1} on the turn-on voltage is shown in the curves labeled 3B in figure IV-2(b), and it demonstrates that a smaller ϕ_{b1} (= 0.05 eV) results in a smaller turn-on voltage. The reverse leakage current remains the same, compared to 2B, and the asymmetry increases.

Diode	ϕ_{b1} (eV)	d_1 (nm)	ϕ_{b2} (eV)	d_2 (nm)	$\Delta\phi$ (eV)	$\epsilon_{r1}/\epsilon_{r2}$
Resonant	0.1	1	0.4	1	0	1/1
1A	0.1	3	0.3	1	0	1/1
2A	0.1	3	0.3	2	0	1/1
3A	0.1	3	0.2	2	0.2	1/2
Step	0.1	1	0.4	1	0	5/1
1B	0.1	1	0.3	0.5	0	5/1
2B	0.1	1	0.3	0.5	0	100/1
3B	0.05	3	0.3	0.5	0	100/1

Table IV-I. Diode design parameters used to calculate the *J(V)* characteristics of resonant (1A, 2A, and 3A) and step (1B, 2B, and 3B) MIIM diodes shown in figure IV-2.

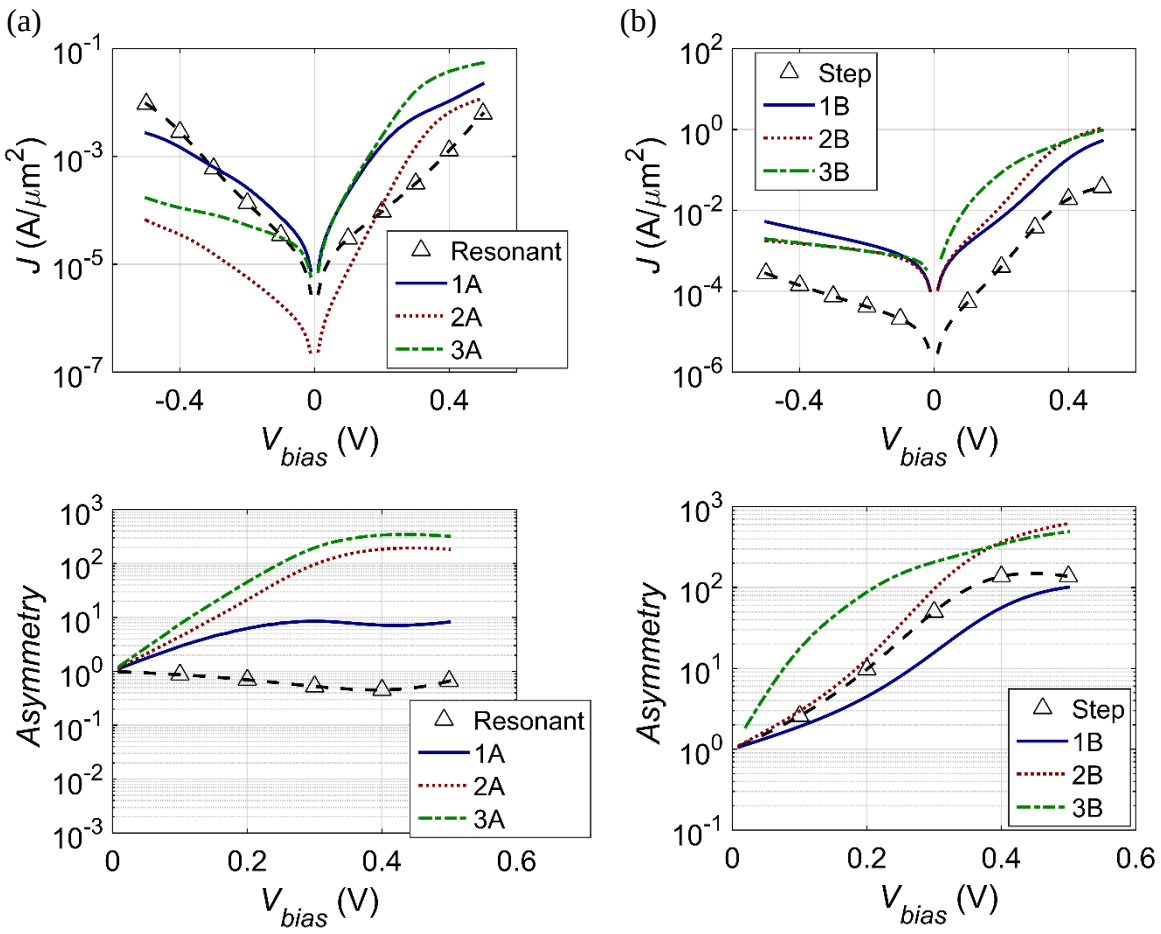

Figure IV-2. The effect of changing diode parameters on MIIM diode current density vs. voltage [J(V)] and asymmetry (ratio of diode forward current to the reverse current) characteristics. Plots of *J(V)* characteristics and asymmetry characteristics of (a) resonant MIIM diodes, and (b) step MIIM diodes, showing the effect of changing diode parameters to increase the forward current density (solid blue, labeled 1A and 1B), reduce the reverse leakage current (dotted red, labeled 2A and 2B), and reduce the turn-on voltage (dash-dot green, labeled 3A and 3B) of the diode.

F. Rectification efficiency of MIIM diodes

The usefulness of the MIIM diodes for high frequency rectification can be determined by calculating their efficiency under monochromatic illumination using the theory of PAT (Grover et al., 2013) and following the method presented in references (Joshi and Moddel, 2015a) and (Joshi and Moddel, 2013). In this section, I calculate the rectification efficiency of the 3A and 3B diodes under monochromatic illumination. While in (Joshi and Moddel, 2015a) and (Joshi and Moddel,

2013), I assumed that the C_D is negligible and therefore does not affect the η_C, here I include its effect by multiplying the efficiency calculated using PAT with the following term,

$$\eta_C^{RC} = \frac{1}{1+\left(2\pi f \frac{R_D R_S}{R_D + R_S} C_D\right)^2}.$$

(IV-4)

For the purpose of calculating $\eta_C{}^{RC}$, the R_D is approximated as

$$R_D = \frac{2\Delta}{I(V_O + \Delta) - I(V_O - \Delta)}.$$

(IV-5)

The Δ is approximated as V_S if the rectenna works in the classical region ($V_S \gg \hbar\omega/q$) and is equal to $\hbar\omega/q$ if it operates in the quantum region ($V_S < \hbar\omega/q$) (Joshi and Moddel, 2015b). In my calculations I will assume R_S = 100 Ω.

To see the effect of the diode reverse leakage current and impedance matching with the antenna on rectenna performance, I calculate the η vs. V_O characteristics for diode 3A of figure IV-2 with changing diode area. The maximum η increases as the edge-length (for a square-shaped diode) increases from 100 nm to 200 nm due to an increase in coupling efficiency, but decreases as the size is increased further to 400 nm due to increased reverse leakage. The results are shown in figure IV-3(a) for a resonant diode, and similar results are seen for a step diode in figure IV-4(a), where I plot the η vs. V_O characteristics for diode 3B of figure IV-2. The load resistance is different from the diode resistance and must be chosen to obtain the V_O where rectenna η is maximum.

The effect of increasing frequency is a decrease in the efficiency due to poor *RC* coupling, following Eq. IV-2 and is shown in figures IV-3(b) and IV-4(b), where I plot the η vs. V_O with increasing *f* (10 THz to 90 THz).

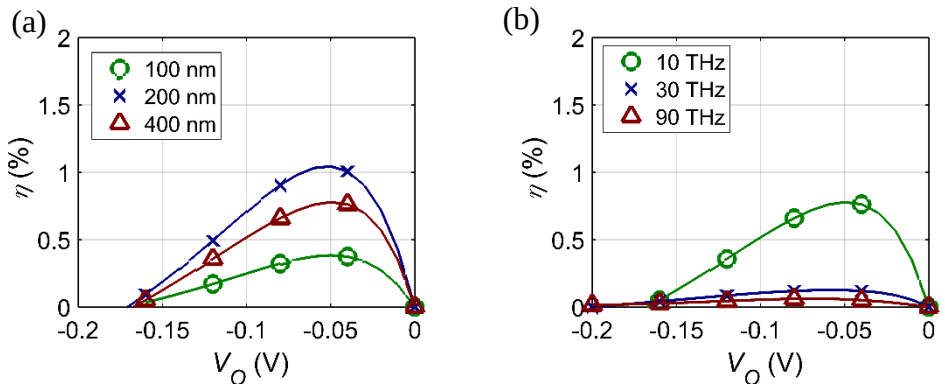

Figure IV-3. Effect of changing diode area and incident frequency on the power conversion efficiency (η) vs. V_O characteristics of the resonant MIIM diode 3A described in figure IV-2, showing the effect of the leakage current and the limited *RC* time constant of the device. The C_D is ~2.2 fF/μm^2. (a) η vs. V_O characteristics of the rectenna for changing edge-length from 100 nm to 400 nm for a square diode keeping f = 10 THz, and P_{in} = 100 μW. The η increases as the diode area increases from 100 nm to 200 nm due to an improvement in the impedance matching and decreases with increase to 400 nm due to increased reverse leakage current. (b) The η vs. V_O characteristics for changing f from 10 THz to 90 THz keeping an edge length of 400 nm and P_{in} = 100 μW. As the frequency increases, the coupling efficiency decreases.

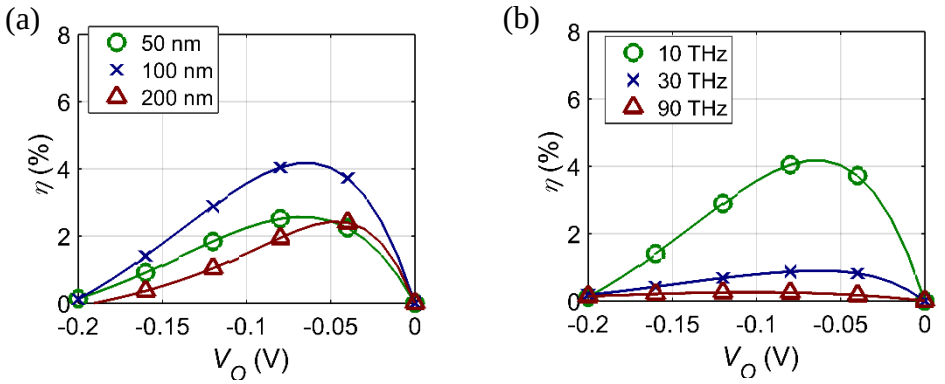

Figure IV-4. Effect of leakage current and the limited RC time constant on the efficiency (η) vs. V_O characteristics of the step MIIM diode 3B described in figure IV-2, with C_D ~17 fF/μm^2. (a) η vs. V_O characteristics of the rectenna for changing diode edge-length from 50 nm to 200 nm (f = 10 THz, P_{in} = 100 μW). The η_{peak} increases with increase in size to 100 nm but decreases at 200 nm due to increased reverse leakage. (b) η vs. V_O characteristics for changing f from 10 THz to 90 THz (edge length 100 nm, and P_{in} = 100 μW). The η_{peak} decreases as the frequency increases due to decrease in the coupling efficiency.

Both diodes show poor performance under illumination, and the efficiency is below 5%, due to small η_C and large I_{leak}. To harvest energy with high efficiency the diodes need, in addition to high

asymmetry, a good impedance match with the antenna, a short *RC* time constant, and small leakage current.

G. Other issues potentially limiting diode performance

In addition to the design issues mentioned above, there are two fundamental problems that could further limit the performance of resonant and step MIIM diodes at high frequencies:

a. Electron transit time through the diode: For efficient diode operation, the transit time of the electron through the diode must be shorter than the period of the incoming wave. However, in resonant MIIM diodes, there is a strong confinement of electrons in the resonant states, and the electron transit time is limited by the time it takes for the electrons to escape out of the resonant states. If the escape time (Kane, 1969; Price, 1988) is greater than the period of the incoming wave, electrons accumulate in the resonant states and modify the energy band diagram, resulting in an increase in the tunneling barrier height, the diode resistance, and the *RC* time constant. Experiments on negative-differential resistance diodes have shown that device operation under high frequency illumination is limited by the electron escape time through resonant states (Sollner et al., 1983). Therefore, the diode design should be such that the escape time is shorter than the period of the incoming wave.

   In step MIIM diodes, the transit time is limited by the low carrier mobility (~1 cm^2/Vs) of electrons traveling in the conduction band of a thick amorphous insulator. Therefore, the speed of the device is limited to frequencies up to a few gigahertz. Single-crystal oxide films can have higher mobility and longer mean free path lengths, and could be a potential solution to this problem.

b. Frequency dependence of the oxide relative permittivity: The relative permittivity of the insulators is a function of frequency and generally decreases with an increase in frequency (Palik, 1998), and results in a decrease in the asymmetry of the step diode. Besides changing the diode asymmetry, the permittivity decrease is beneficial in reducing the diode capacitance, and hence the *RC* time constant. A tradeoff exists between the diode asymmetry and the diode *RC* time constant, and materials selection is important when designing MIM diodes.

H. Further improvements in diode characteristics

The *J(V)* characteristics of the diodes can be improved further by tuning the metal and insulator parameters. The addition of a third insulator to the resonant MIIM diode forms a resonant MIIIM diode with two triangular wells and sequential resonant states, improving the asymmetry and reducing the turn-on voltage. In the step diode, the reverse current density can be further reduced and the forward current increased by adding a third insulator, forming a step-MIIIM diode where the second insulator is a resonant well (Maraghechi et al., 2012a; Moddel and Eliasson, 2004). The guidelines for resonant and step MIIM diodes apply to resonant and step MIIIM diodes. Unfortunately, providing a third layer of sufficient thickness increases the thickness and can increase the diode resistance and therefore degrade the impedance match with the antenna.

New diodes and structures such as the geometric diode (Moddel, 2014; Moddel et al., 2012; Zhu et al., 2013b; Z. Zhu et al., 2014) and the traveling-wave diode (Grover et al., 2010a; Hobbs et al., 2007) have short *RC* and good coupling efficiency, respectively, for operation up to 100 THz. Recently, we successfully demonstrated the working of a 28 THz rectenna detector using geometric diodes (Zhu et al., 2013b; Z. Zhu et al., 2014). However, in spite of the excellent detectivity and low noise equivalent power, the asymmetry of the device *J(V)* characteristics has

been insufficient for energy harvesting. Improvements in diode design (Zhu, 2014) could potentially give a short *RC* time constant and good asymmetry at small bias voltages.

I. Conclusions

I analyzed resonant and step metal/insulator/insulator/metal (MIIM) diode designs and presented guidelines to improve their asymmetry and reduce the diode turn-on voltage. An efficiency calculation of rectenna performance under monochromatic illumination showed that the diode performance is still poor, due to inefficient coupling with the antenna and a significant reverse leakage current. These issues are critical to the operation of a rectenna at high frequencies, but are often neglected in literature. Further tuning of diode parameters following the guidelines presented here, and new diode designs are required to enhance the rectification efficiency of MIM diodes for high frequency (infrared) energy harvesting.

CHAPTER V

SIMPLE FIGURE OF MERIT FOR OPTICAL RECTENNA ANALYSIS

A. Chapter summary

Harvesting infrared and visible light energy using optical rectennas — diode-coupled optical antennas — is strongly dependent on the diode current-voltage characteristics. Predicting the conversion efficiency is an arduous procedure that involves calculating the efficiency by solving the nonlinear diode circuit using the theory of photon-assisted tunneling. Because of the complexity of the calculations, many rectenna diodes have been reported without indications of how well these diodes will actually function in a rectenna. To provide a quick assessment of the diodes' usefulness in optical rectennas, I provide a figure of the merit that incorporates the diodes' current-voltage and capacitance, the antenna radiation resistance, and the illumination parameters.

B. Introduction

An optical rectenna consists of an antenna that receives high frequency electromagnetic radiation, connected to a high-speed diode that rectifies the AC currents to DC. Rectennas have been proposed for energy harvesting in the IR and for optical detection (Corkish et al., 2002; Hoofring et al., 1989; Moddel, 2013; Sarehraz et al., 2005; Yu et al., 2014; Zhu et al., 2013b), and use high-speed diodes, such as metal-insulator-metal (MIM) diodes (Alimardani and Conley, 2013; Choi et al., 2011; Grover and Moddel, 2012a; Heiblum et al., 1978; Maraghechi et al., 2012b; Miskovsky et al., 2012) and geometric diodes (Zhu et al., 2013b; Zixu Zhu et al., 2014). Their analysis is carried out using the theory of photon-assisted tunneling (PAT) applied to the diode (Grover et al., 2013), and requires solving the currents and voltages in a nonlinear equivalent

electrical circuit (Joshi et al., 2013; Joshi and Moddel, 2015a, 2013), which is complex and time-consuming. In this chapter, I propose a simple figure of merit (*FOM*) to estimate the performance of a rectenna under monochromatic illumination.

Several parameters determine the performance of the rectenna, including diode parameters, antenna parameters, and the input conditions. I calculate the effect of the different parameters on rectenna conversion efficiency, determined using PAT theory, and the results correspond well with the *FOM* calculations. Then I demonstrate the calculation of the *FOM* using step metal-insulator-insulator-metal (MIIM) diodes and resonant MIIM diodes (Grover and Moddel, 2012a). The *FOM* provides a convenient and qualitative expression to estimate the rectenna's performance.

C. Parameters determining rectenna performance

There are six parameters that determine the performance of a rectenna system and appear in the expression of the *FOM*. They can be divided into three categories,

a. Input conditions: Power at the antenna terminals (P_{in}), and the frequency ($f = \omega/2\pi$) of the incoming electromagnetic wave.
b. Diode characteristics: Capacitance (C_D), forward resistance (R_f) and reverse resistance (R_r) in the form of the *I(V)* characteristics of the diode, determined by approximating the diode *I(V)* by a piecewise linear characteristic.
c. Antenna parameters: Radiation resistance (R_S) of the antenna. I assume that the coupling efficiency between free-space and the antenna is unity, the antenna is in resonance (so that its impedance is purely resistive), and the propagation of the surface plasmons from the antenna to the diode is lossless. If known, these loss parameters can be included in the expression for the *FOM* as multiplicative terms.

As will be shown, the rectenna performance depends on the input conditions which means that the rectenna and the diode have to be designed based on the application. The six parameters determining the *FOM* of the rectenna can be grouped into three recognizable terms,

a. Diode reverse leakage power: The reverse leakage power (P_{leak}) is the DC power lost due to the flow of finite reverse leakage current (I_{leak}) in the diode at the operating voltage (V_O) of the rectenna. Since the rectenna operates in the second quadrant of the diode *I(V)*, the diode reverse leakage current at V_O flows in the opposite direction to the DC illuminated current (I_{illum}) and therefore degrades rectenna performance (Joshi et al., 2013; Moddel, 2013). The P_{leak} at the V_O due to the reverse leakage current is,

$$P_{leak}(V_O) = V_O I_{leak}(V_O).$$

(V-1)

A good energy harvesting diode has a leakage current such that $P_{in}/P_{leak} \gg 1$.

b. Diode responsivity: For efficient rectification, the diode must be asymmetric around the rectenna V_O and have a large responsivity (Grover, 2011; Tucker and Feldman, 1985). The diode current responsivity, which is the DC current out per unit AC power in, can be written as,

$$\beta_\Delta = \frac{1}{\Delta}\left(\frac{I(V_O+\Delta) - 2I(V_O) + I(V_O-\Delta)}{I(V_O+\Delta) - I(V_O-\Delta)}\right).$$

(V-2)

Here, the Δ is a step voltage that depends on the operating regime of the rectenna. Although the diode voltage amplitude (V_D) is the relevant parameter, due to its dynamic nature and dependence on V_O, I use V_S as an approximation for V_D to determine the operating regime. I approximate Δ by the source voltage (V_S) if the rectenna operates in the classical regime ($V_S \gg$

$\hbar\omega/q$), and is equal to $\hbar\omega/q$ if the rectenna is in the quantum regime ($V_S < \hbar\omega/q$) (Joshi, 2015; Joshi and Moddel, 2015b). A formula for determining V_S is given below.

$$V_S = \sqrt{8 R_S P_{in}^{AC}} \ .$$

(V-3)

c. Coupling efficiency between the antenna and the diode: The input conditions and the diode *I(V)* characteristics determine the diode AC resistance (R_D). For quantum operation, R_D is the secant resistance of the diode because in quantum operation the oscillating current samples the diode at only two points in its *I(V)* curve) (Grover et al., 2013). Since calculating the R_D in the classical case is not straightforward, I approximate it using the same expression as the quantum R_D but with a Δ (= V_S) suitable for classical operation,

$$R_D = \frac{2\Delta}{(V_O + \Delta)/R_f - (V_O - \Delta)/R_r} \ .$$

(V-4)

The R_D in parallel with R_S determine the effective AC resistance of the system, which along with the C_D gives the *RC* time constant and the cut-off frequency (f_c) of the rectenna,

$$f_c = \frac{1}{2\pi \dfrac{R_S R_D}{R_S + R_D} C_D} \ .$$

(V-5)

The coupling efficiency is written as (Grover, 2011; Sanchez et al., 1978),

$$\eta_C = \frac{\dfrac{4 R_S R_D}{(R_S + R_D)^2}}{1 + \left(2\pi f \dfrac{R_S R_D}{R_S + R_D} C_D \right)^2} \ .$$

(V-6)

The η_C is 100% when $R_S = R_D$ and $f \ll f_c$.

D. Steps to determine the figure of merit

I calculate the *FOM* using the following steps:

1. Calculate the input power at the antenna,

$$P_{in}^{AC} = \eta_{ant} A_{eff} I_{in} . \tag{V-7}$$

The η_{ant} is the antenna efficiency, A_{eff} is the antenna effective area, and I_{in} is the input intensity. In the absence of information about the antenna, I make the approximation that $\eta_{ant} = 1$.

2. Calculate the voltage across the antenna using Eq. V-3 (Joshi et al., 2013; Joshi and Moddel, 2015a, 2013).
3. Determine if the rectenna operates in the classical regime ($V_S > \hbar\omega/q$) or the quantum regime ($V_S < \hbar\omega/q$).
4. Using the appropriate Δ ($=\hbar\omega/q$ in the quantum regime, and V_S in the classical regime) and V_O, estimate the β_Δ using Eq. V-2 and R_D using Eq. V-4 assuming, in the classical case, that the diode is piecewise linear. The R_D in the classical regime is an approximation to the diode AC resistance. I recommend a $V_O = -\Delta/2$ as a starting value to approximate the R_D and β_Δ, as I do in the next section. This is not the V_O giving the maximum conversion efficiency of the rectenna but is convenient for comparing the rectenna *FOM* under different conditions. To determine the V_O at which the η is maximum, the V_O can be varied to maximize the *FOM*, as I show later when I calculate the *FOM* of MIIM diodes.
5. Calculate the η_C at the V_O using Eq. V-6.

6. Calculate the rectenna *FOM*, expressed as the combination of the β_{Δ}, η_C, and P_{leak} as follows,

$$FOM = 100\left(|V_O|\beta - \frac{|V_O I_{leak}(V_O)|}{P_{in}}\right)\times \eta_C \,.$$

(V-8)

The expression is such that the *FOM* corresponds approximately to the power conversion efficiency of the rectenna. If *FOM* < 1 the rectenna design is poor and the conversion efficiency is poor, whereas for *FOM* > 10 the rectenna can be expected to perform well and the conversion efficiency is >10%. This is shown in the next section where I compare the *FOM* with the conversion efficiency calculated for a rectenna having a piecewise linear diode, under different conditions using photon-assisted tunneling (PAT) theory presented in references [(Joshi et al., 2013; Joshi and Moddel, 2015a, 2013)]. In those referenced papers C_D was assumed to be negligible and had no effect on the rectenna conversion efficiency. Here I introduce the effect of C_D using an *RC* coupling efficiency term,

$$\eta_C^{RC} = \frac{1}{1+\left(2\pi f \frac{R_D R_S}{R_D + R_S} C_D\right)^2} \,.$$

(V-9)

The overall conversion efficiency, approximated by the *FOM*, is the product of η_C^{RC} and the efficiency calculated using PAT theory presented in references [(Joshi et al., 2013; Joshi and Moddel, 2015a, 2013)].

E. Calculation of the figure of merit

To show the correspondence of the *FOM* with the conversion efficiency calculated from PAT, I calculate the rectenna *FOM* vs. R_r for different input conditions (P_{in}, f) and diode characteristics (C_D, R_f). In each calculation, I change one parameter while keeping the other parameters the same. The plots of *FOM* vs. R_r with changing f, C_D, P_{in}, and R_f are shown in figures V-1 and V-2. The R_S is assumed to be 100 Ω, required for impedance matching with free-space and, as suggested in the previous section, the V_O is fixed at half $-\hbar\omega/q$ in the quantum regime and half $-V_S$ in classical regime.

I make the following observations based on FOM calculations with results shown in figures V-1 and V-2,

a. With decreasing P_{in}, the *FOM* degrades at low values of R_r (figure V-1(a)) due to the excess leakage current. The P_{in} is varied from 10 nW to 1000 nW, which is in the range of spatially coherent power available from blackbody sources such as the sun (Joshi and Moddel, 2013; Mashaal and Gordon, 2011).
b. The *FOM* decreases on increasing the R_f (figure V-1(b)) due to an increase in the *RC* time constant of the rectenna and an increase in R_D at the V_O, resulting in a poor impedance matching condition.
c. An increase in C_D (figure V-2(a)) and an increase in f (figure V-2(b)) leads to a decrease in the *FOM*, by increasing the effect of the *RC*-limited cut-off frequency of the rectenna.

I also calculate the rectenna conversion efficiency using PAT theory under the same conditions as above. The efficiency results are shown in figures V-1 and V-2 below the *FOM* plots, and follow the same trend as the *FOM* with the change in diode and input parameters, showing a very strong correlation between *FOM* and PAT-theory results.

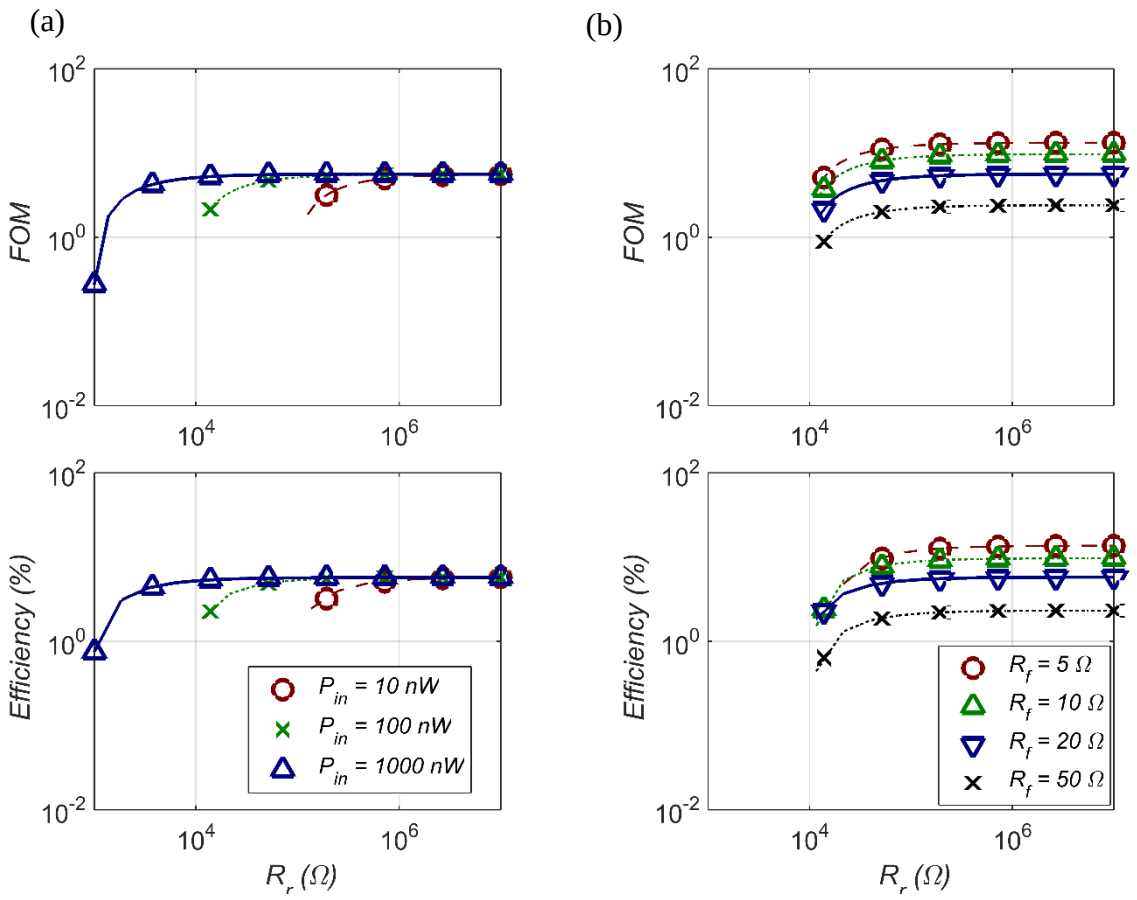

Figure V-1. Plots showing close agreement between the figure of merit (FOM) and the rectenna energy conversion efficiency (η) vs. the diode reverse resistance (R_r), calculated using PAT theory for different input powers (P_{in}) and diode forward resistances (R_f). The diode has piecewise linear *I(V)* characteristics. (a) Effect of varying P_{in} (10 nW to 1000 nW) on the *FOM* (with R_f = 20 Ω, f = 10 THz, C_D = 1 fF). The *FOM* decreases with decrease in the R_r due to the increase in leakage current. (b) Effect of varying R_f (5 Ω to 50 Ω) on the FOM (with P_{in} = 100 nW, f = 10 THz, C_D = 1 fF). As R_f increases, the impedance matching with the antenna at the operating voltage (V_O) gets poorer and the *FOM* decreases. Also plotted below the *FOM* plots is the efficiency calculated using photon-assisted tunneling (PAT) under the same conditions, showing that the conversion efficiency follows the same trend as the *FOM*.

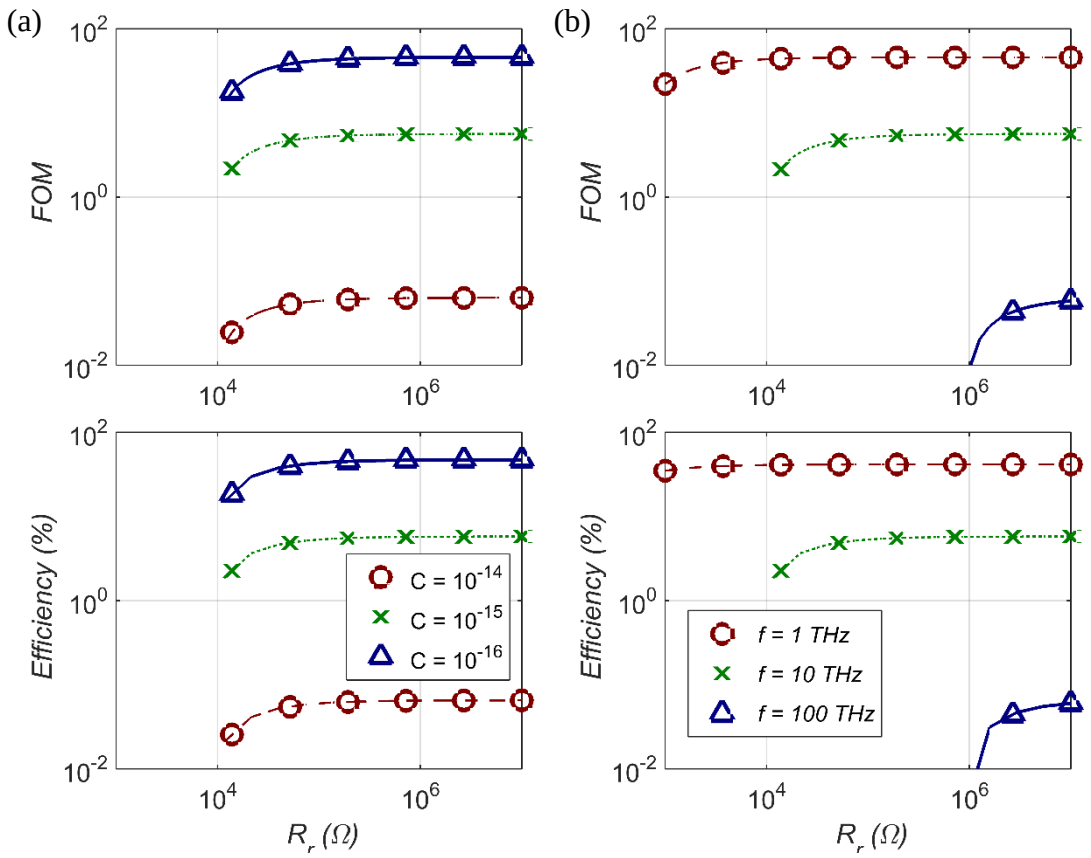

Figure V-2. *FOM* vs. R_r and the corresponding rectenna conversion efficiency calculated using PAT, showing a correlation between the two, for varying C_D and f. (a) Effect of C_D (10 fF to 0.1 fF) on the *FOM* (with R_S = 100 Ω, R_f = 20 Ω, f = 10 THz, P_{in} = 100 nW). Decreasing C_D increases the *FOM* due to a decrease in the rectenna *RC* time constant. (b) Effect of f (1 THz to 100 THz) on the *FOM* (for P_{in} = 100 nW, R_S = 100 Ω, R_f = 20 Ω, C_D = 1 fF). Increasing f decreases the *FOM* because the V_O becomes more negative and therefore the curves shift to the right due to increase in the leakage current relative to the rectified current.

These results show that the *FOM* is a good indicator of the performance of the rectenna, and elaborate calculations are not required to get an approximate idea of its energy harvesting efficiency.

F. Figure of merit of MIIM diodes

I demonstrate the calculation of the *FOM* using a resonant MIIM diode and a step MIIM diode (Grover and Moddel, 2012a). I use MIIM diodes because they can achieve greater asymmetry, a smaller turn-on voltage, and give higher rectification efficiencies compared to single insulator MIM diodes. The diode structure is shown in figures V-3(a) and V-3(c) and their current density vs. voltage [*J(V)*] characteristics, determined using the transfer-matrix method presented in reference [(Grover and Moddel, 2012a)], are plotted in figures V-3(b) and V-3(d), respectively.

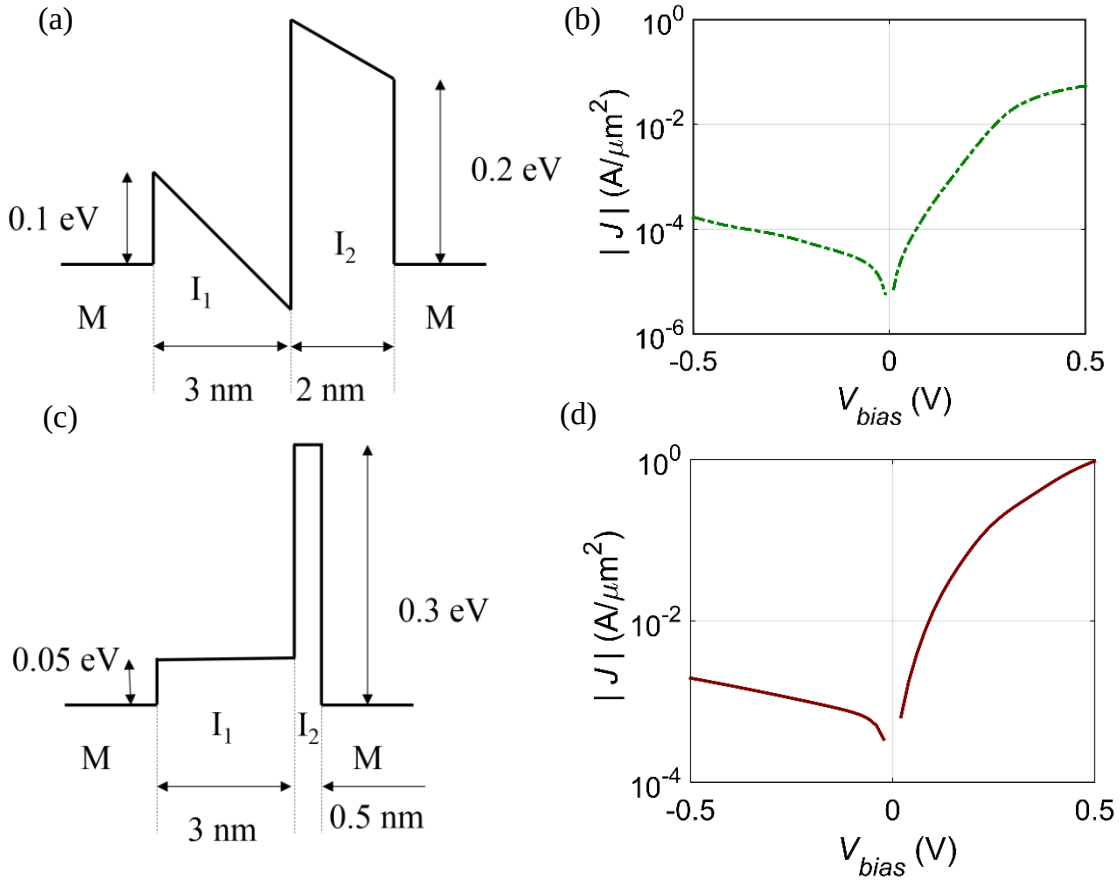

Figure V-3. Illustration of the energy-band diagram and the calculated current density vs. voltage [*J(V)*] characteristics of resonant and step MIIM diodes. (a) Energy-band diagram of the resonant diode for the indicated barrier heights and insulator thicknesses, and a work function difference ($\Delta\phi$) of 0.2 eV between the two different metal layers. The relative permittivity of the

two insulators (I_1 and I_2) are 1 and 2, respectively. (b) *J(V)* characteristics of the resonant MIIM diode for the parameters in (a), calculated using the method presented in reference [(Grover and Moddel, 2012a)] that uses the transfer matrix method to solve for the Schrodinger equation. (c) Energy-band diagram of the step diode for the barrier heights and insulator thicknesses indicated in the figure. The $\Delta\phi$ = 0 eV, and the relative permittivities of I_1 and I_2 are 100 and 1, respectively. (d) The *J(V)* characteristics of the step MIIM diode for the conditions given in (c). The effective mass of the electron in the insulators is assumed to be its rest mass.

To see the effect of the reverse leakage current on diode performance in these double-insulator diodes, I first calculate the *FOM* vs. V_O characteristics for the resonant MIIM diode with changing diode edge-length (for a square-shaped diode) and changing incident frequency. The peak *FOM* increases as the size increases (from 100 nm to 200 nm) due to increase in coupling efficiency, but decreases as the size is increased further (to 400 nm) due to increased reverse leakage current. The results are shown in figure V-4(a). The η characteristics, in figure V-4(b), follow the same trend as the *FOM* showing that there is a good correlation between the two.

Similar results are seen in figures V-5(a) and V-5(b), where I plot the *FOM* and η vs. V_O characteristics for a step MIIM diode, for increasing diode edge-length (50 nm to 200 nm).

The effect of increasing frequency is a decrease in the *FOM* and the η due to poor *RC* coupling, following Eq. V-6. This is shown in figures V-4(c) and V-4(d) for the resonant MIIM diode and for the step MIIM diode in figures V-5(c) and V-5(d), where I plot the *FOM* and η vs. V_O with increasing *f* (10 THz to 90 THz).

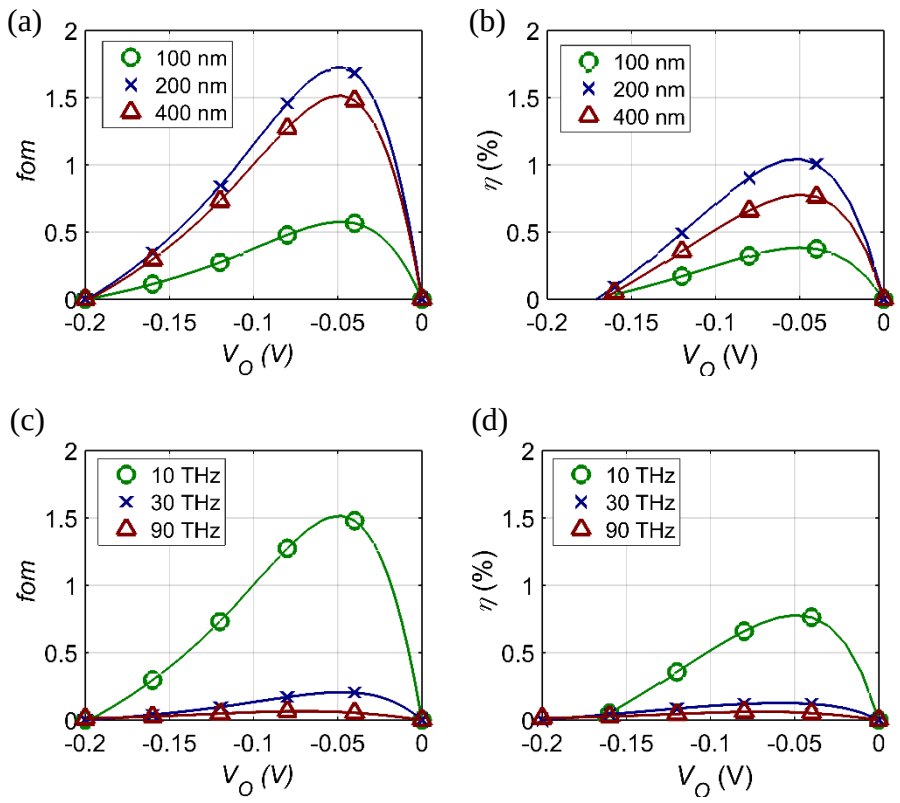

Figure V-4. Figure of merit (*FOM*) and conversion efficiency (η) characteristics of the resonant MIIM diode in figure V-3(b), showing the effect of the increase in reverse leakage current with size and operating frequency. The C_D is ~2.2 fF/μm^2. (a) *FOM* vs. V_O characteristics of the rectenna for increasing diode edge-length from 100 nm to 400 nm keeping f = 10 THz, and P_{in} = 100 μW, and (b) η vs. V_O characteristics of the rectenna calculated using photon-assisted tunneling PAT theory, and the same conditions as in (a). Both (a) and (b) show that with the increase in diode size, the peak *FOM* and conversion efficiency (η_{peak}) first increase due to improvement in the η_C but later decrease due to increase in the reverse leakage current. (c) *FOM* vs. V_O characteristics for increasing f from 10 THz to 90 THz keeping an edge length of 400 nm and P_{in} = 100 μW, and (d) η vs. V_O characteristics calculated using photon-assisted tunneling (PAT) theory, under the same conditions as in (c), showing that an increase in the f decreases the coupling efficiency due to the limited *RC* time constant of the diode.

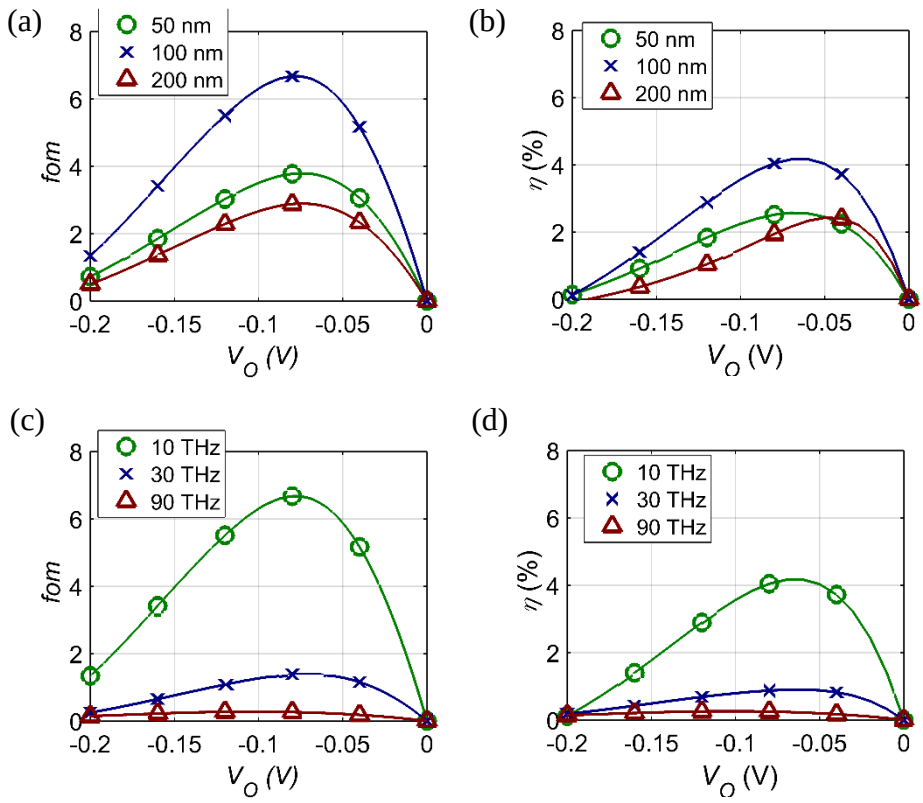

Figure V-5. Figure of merit (*FOM*) and conversion efficiency (η) vs. V_O characteristics for the step MIIM diode shown in figure V-3(d), with C_D ~17 fF/μm^2. The results follow the same trend as the resonant MIIM diode results shown in figure 4. (a) *FOM* vs. V_O characteristics of the rectenna for increasing diode edge-length from 50 nm to 200 nm keeping f = 10 THz, and P_{in} = 100 μW, and (b) conversion efficiency vs. V_O characteristics of the rectenna calculated using photon-assisted tunneling PAT theory, for the same conditions as in (a). (c) *FOM* vs. V_O characteristics for increasing f from 10 THz to 90 THz and keeping an edge length of 100 nm and P_{in} = 100 μW, and (d) η characteristics calculated using photon-assisted tunneling PAT theory, under the same conditions as in (c).

Although the *FOM* corresponds only approximately to the PAT conversion efficiency of the rectenna (because the R_D, β, and I_{leak} are approximated assuming that the diode is piecewise linear), it is a good indicator of the monochromatic efficiency of the rectenna.

G. Conclusion

In this chapter, I developed a method to calculate the figure of merit (*FOM*) of a rectenna. The simple expression for the *FOM* is a combination of the three mechanisms that determine rectenna performance: the diode reverse leakage power relative to the input power, diode responsivity, and the coupling efficiency between the antenna and the diode. I calculated the *FOM* using different rectenna parameters and input conditions, and compared the results with conversion efficiency calculated using photon-assisted tunneling theory showing a strong correlation between the two. I demonstrated the application of the *FOM* to double insulator MIM (MIIM) diodes and showed that the simple expression can be used to provide a good estimate of the rectenna performance under monochromatic illumination.

CHAPTER VI

METAL-INSULATOR-METAL DIODES FOR TERAHERTZ DETECTION

A. Introduction

Metal-insulator-metal (MIM) diodes operate on the principle of electron tunneling through an insulator. Electron tunneling through thin insulators is an inherently fast process, occurring over a time scale of less than a femtosecond (Hartman, 1962). Such high speed operation makes MIM diodes attractive for operation at terahertz frequencies. Since electron tunneling is a nonlinear process, MIM diodes have nonlinear current-voltage [*I(V)*] characteristics. A fast response with a nonlinearity in the *I(V)* allows for rectification of high frequency AC signals into DC. The DC current is directly proportional to the AC input power. In this chapter, I will look at the design and characterization of MIM diodes for detection at 1 THz.

B. Requirements for efficient detection

The MIM diode should meet the following requirements for high overall system efficiency:

1. Good system efficiency requires a MIM diode with high responsivity: diode current responsivity (β) is an important performance figure for MIM diodes working as detectors. It is defined as the maximum DC output current in amperes per unit AC input power in watts. Diode β is a function of the DC *I(V)* nonlinearity and can be calculated from the DC *I(V)* characteristics of the diode using Eq. VI-1 (Grover and Moddel, 2011; Sanchez et al., 1978).

$$\beta = \frac{d^2 I}{dV^2} \Big/ 2\frac{dI}{dV} \tag{VI-1}$$

2. Efficient energy transfer from the antenna to the diode requires matching the antenna and diode impedances: The AC input power to the diode is a function of the coupling between the antenna and the diode. A good impedance match provides efficient transfer of antenna-captured electromagnetic power to the diode. Eq. VI-2 defines the power coupling ratio (Grover, 2011).

$$\eta_C = \frac{4\dfrac{R_S R_D}{(R_S + R_D)^2}}{1 + \left(\omega \dfrac{R_S R_D}{(R_S + R_D)} C_D\right)^2}$$

(VI-2)

I modeled the diode as a lumped element using a parallel combination of the diode resistance R_D and diode capacitance C_D. The ω is the angular frequency ($=2\pi f$) of the incoming wave. The antenna is modeled as a voltage source with its radiation resistance denoted by R_S.

3. The diode *RC* time constant must be less than the operating frequency: From Eq. VI-2, to achieve a coupling efficiency close to unity the following conditions must be met,

$$\omega \frac{R_S R_D}{(R_S + R_D)} C_D << 1 \text{ and } R_S = R_D$$

(VI-3)

A good impedance match at high frequencies requires a diode *RC* time constant less than the inverse of the operating angular frequency, and $R_A \sim R_D$.

Since MIM diodes have nonlinear *I(V)* characteristics, the bias voltage can be adjusted to change the AC resistance of the diode and the impedance matching with the antenna. A bias voltage for good noise equivalent power (NEP) (Rogalski, 2010; Zixu Zhu et al., 2014) is a compromise between the impedance matching and the β. However, biasing the diode results in a DC current flow at all times during device operation, resulting in power consumption and

unwanted shot noise increasing the NEP of the detector (Zhu, 2014). I looked at both biased and zero-bias diodes for detection.

C. Requirements for detection at 1 THz

For detection of 1 THz radiation, the rectenna *RC* time constant must be < 160 fs. To match to a 100 Ω antenna, the small signal resistance of the diode at the biasing voltage should be 100 Ω. Such a diode connected to a matched antenna requires a C_D < 3.2 fF and therefore, the diode area and the insulator thickness must be such that the diode meets this requirement. In figure VI-1, I show a plot of the C_D vs the ratio of the insulator thickness (d) and the dielectric constant (ϵ_r) for different diode edge lengths (for a square shaped diode). The C_D for the parallel-plate devices is written as,

$$C_D = \frac{\varepsilon_r \varepsilon_o A}{d} \tag{VI-4}$$

Here ϵ_o is the permittivity of free space, and A is the diode area. As the diode area increases, the requirement for a thicker insulator and a smaller relative permittivity increases. However, a thicker insulator (> 4 nm) results in reduced current density, as shown in figure VI-2, where I plot the variation of the diode zero bias differential resistance, calculated by solving for the diode *I(V)* using the Schrodinger equation (Grover and Moddel, 2012a), as a function of the barrier height and oxide thickness. In addition, there are limited materials that have low relative permittivity values at 1 THz, where alumina and nickel oxide have relative permittivity of ~9.5 (Bolivar et al., 2003) and ~6.5 (Thacker, University of Missouri - Columbia), respectively. Therefore for efficient 1 THz operation, the diode size should be <400 nm.

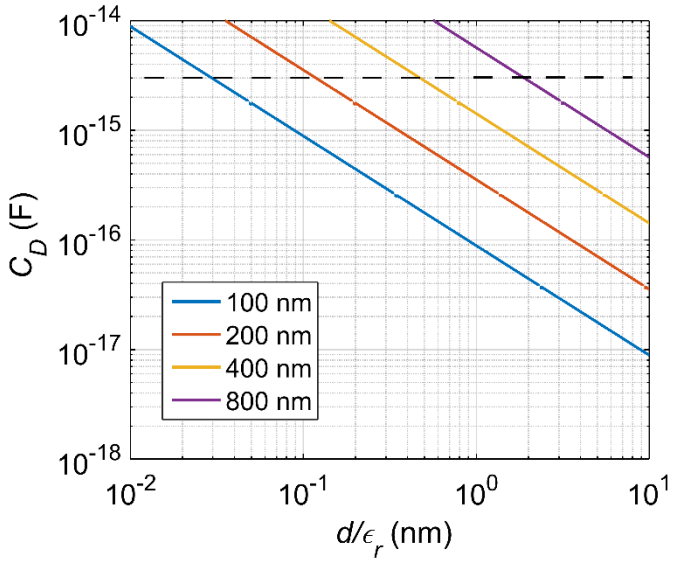

Figure VI-1. Diode capacitance (C_D) vs. the ratio of insulator thickness (d) and the relative permittivity (ϵ_r) for different diode edge-lengths (for a square-shaped diode). Increasing the diode size and decreasing the ratio d/ϵ_r increases C_D. The dotted black line shows the required C_D so that the cut-off frequency of the rectenna with a 100 Ω antenna and diode is 1 THz.

D. Materials for terahertz MIM diodes

As shown in figure VI-2, lower barrier heights and thinner oxides give lower R_D, suitable for matching the diode to the antenna. The metal-oxide barrier heights can vary depending on the metal and oxide structure and deposition conditions. Ni/NiO and Nb/Nb_2O_5 barrier heights are ~0.1 eV (Phiar, Corp.). An advantage of Nb over Ni is that Nb is compatible with dry etching. However, only NiO has a dielectric constant low enough for operation at 1 THz. The dielectric constant of Nb_2O_5 is ~24 (Grover and Moddel, 2012a) and therefore requires a smaller diode (factor of ~3) and subsequently a thinner oxide to achieve a 100 Ω device with a low *RC* time constant. However, thinner oxides (< 2 nm) give small β. These requirements make device fabrication using Nb_2O_5 challenging, and so I chose the simple Ni/NiO/Ni diode device for 1 THz detection.

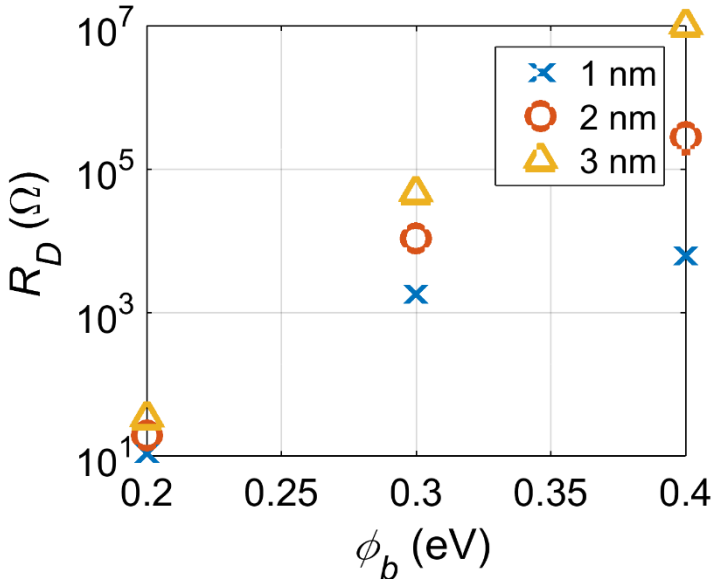

Figure VI-2. Resistance (R_D) of a symmetric diode at zero bias vs. the barrier height (ϕ_b) for different oxide thicknesses (d_{ox}). The area of the diode is (1 μm x 1 μm). The R_D increases with increase in barrier height and oxide thickness. The results are calculated from the diode *I(V)* characteristics determined by solving the Schrodinger equation as in (Grover and Moddel, 2012a)

E. Ni/NiO/Ni diodes for terahertz rectennas

a. Device simulation

Using the method presented in (Grover and Moddel, 2012a) I simulated the current density vs. voltage [*J(V)*] characteristics of the Ni/NiO/Ni diode for different oxide thicknesses. The *I(V)*, R_D, and β characteristics of the simulated Ni/NiO/Ni with a 2 nm thick oxide and a Ni/NiO barrier height of 0.1 eV are shown in figure VI-3. In the simulations, I do not take image force lowering into account due to ambiguity regarding its application (Hartstein and Weinberg, 1979, 1978). I found that a d_{ox} = 2 nm gives the highest biased peak β for a 200 nm diode (ϵ_r = 6.5) when illuminated by a 1 THz source, as shown in figure VI-4. We used this specification as the target for device fabrication.

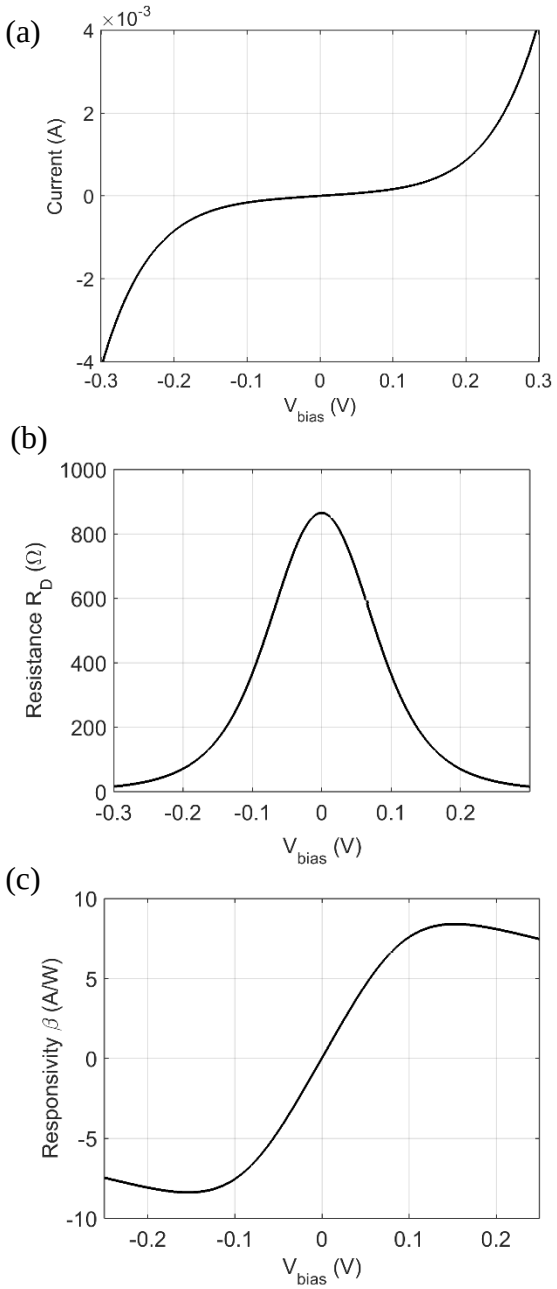

Figure VI-3. Simulated (a) current vs. voltage *I(V)*, (b) resistance (R_D), and (c) calculated DC responsivity (β) characteristics of Ni/NiO/Ni diode with d_{ox} = 2 nm and a Ni/NiO barrier height of 0.1 eV. The diode area is (400 nm)^2. The peak β is ~8 A/W at a bias voltage of 0.15 V where the R_D = 150 Ω.

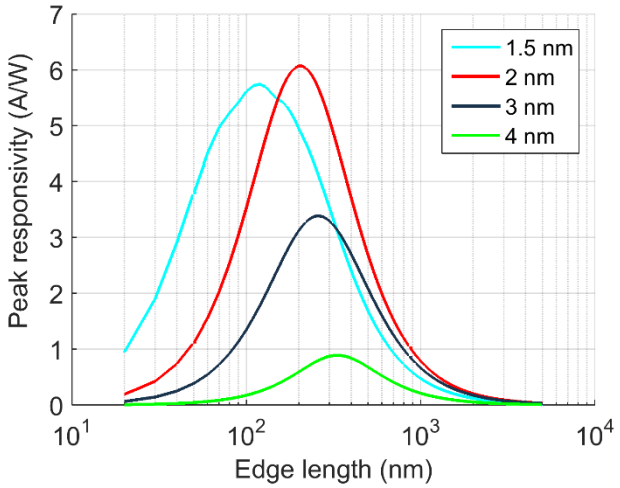

Figure VI-4. Simulated peak rectenna β under 1 THz illumination vs. the edge length of the Ni/NiO/Ni diode. Diode *I(V)* was simulated for different oxide thicknesses (four are shown) and the coupling efficiency (η_C) was calculated from Eq. VI-2 for varying diode area. The AC β was equal to the DC β multiplied with the η_C. A maximum in the peak β is obtained for a 2 nm thick NiO and a diode edge length of 200 nm. The β at diode sizes < 200 nm is low due to poor impedance match with the 100 Ω antenna.

b. Device fabrication

We used several different techniques to fabricate the MIM diodes: an overlap process, a four-layer process (Zhu, 2014), and the shadow-mask process.

The initial MIM diodes were patterned using electron-beam lithography. My colleague, Zixu Zhu, used a scanning electron microscope modified and controlled using the 'Nanometer Pattern Generation System' software by JC Nabity (Nabity, 2015). Because e-beam lithography is time consuming and the resolution of this machine was not sufficient to give 200-400 nm diodes with clean metal liftoff, we investigated using a deep UV stepper for lithography. We had issues using single layer resist due to metal deposition on the sidewalls of the resist. To avoid sidewall coating and have better metal liftoff, I developed a bilayer resist technique at the Colorado Nanofabrication Lab (CNL) using a SPR3012 photoresist suitable for 365 nm i-line lithography, and an SF5 under-layer. Figure VI-5 shows the SF5-SPR3012 bilayer pattern developed using MF-26 developer.

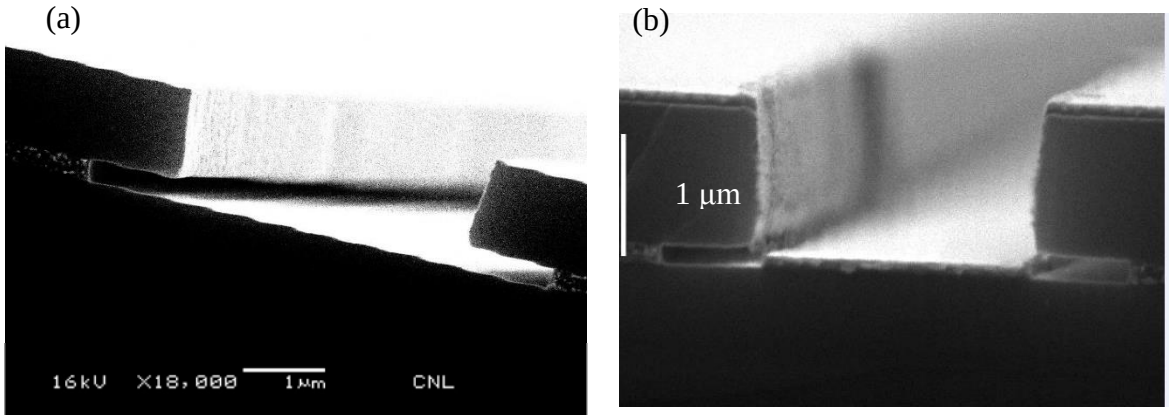

Figure VI-5. Cross-section scanning electron micrograph of the bilayer resist pattern. (a) The bilayer resist pattern showing the undercut in the SF5 under-layer resist (~300 nm thick) beneath the SPR3012 photoresist pattern (~1 μm thick), and (b) bilayer resist pattern with evaporated nickel (~60 nm thick). The undercut allows for better lift-off of the metal with the photoresist.

Because the resolution of the mask writer 'Heidelberg DWL 66FS' was limited to 1 μm, the minimum diode size was 1 μm. I deposited and oxidized the thermally evaporated Ni film in an oxygen plasma so that the oxide was thick enough to have a measurable R_D. Although the device had a poor *RC* time constant, it provided a good proof of concept of the working of the device. An optical microscope image of a diode fabricated using optical lithography is shown in figure VI-6(a). The measured *I(V)* characteristics of a diode are shown in figure VI-6(b) along with the simulated *I(V)* characteristics of a symmetric barrier using three fitting parameters: an electron mass equal to the free electron mass of the electron, a 3.5 nm thick oxide, and a 0.07 eV barrier. The simulated and experimental results match well with each other, showing that the barrier height is lower than previously expected. The diode DC responsivity was ~4 A/W at a bias of 0.08 V. I will present the experimental method used to measure the *I(V)* characteristics in the next section.

(a)

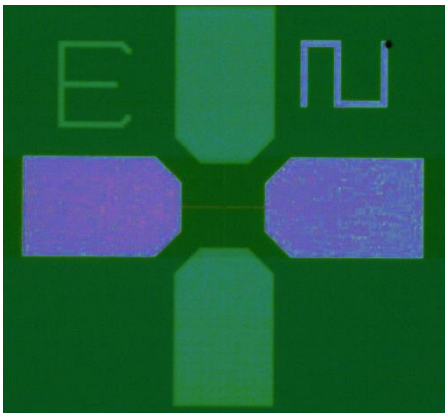

(b)

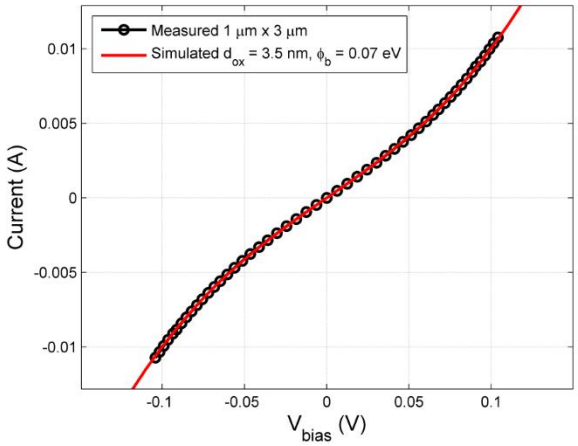

Figure VI-6. Structure and *I(V)* characteristics of a Ni/NiO/Ni diode fabricated using the overlap process and i-line optical lithography. (a) An optical microscope image of a 2 μm x 3 μm overlap diode, and (b) Measured *I(V)* characteristics (black circles) and the fitted *I(V)* characteristics (solid red line) of a 1 μm x 2 μm diode. The barrier height and the oxide thickness extracted from simulations are 0.07 eV and 3.5 nm respectively. The effective mass of the electron is assumed to be the free electron mass. The simulated and measured characteristics overlap each other.

The small area diodes with edge-lengths between 250 nm and 800 nm were fabricated using the bilayer resist overlap process by Zixu Zhu at the UCSB Nanofabrication facility. The fabrication details are in reference (Zhu, 2014). The overlap process had residue issues and gave inconsistent diodes, as I will show later, while the 4-layer process used later had resolution limitations and complicated processing with lift-off issues.

c. Electrical measurements

I used a four-point probe method to determine the DC *I(V)* characteristics of the diode. The measurement setup is shown in figure VI-7(a). Current was applied between two outer electrodes (high and low), and the voltage was measured between two inner electrodes (sense high and sense low). The probes were set up such that they were shorted to the ground through mercury switches before they were put down on the device pads to avoid breaking down the diode due to static discharge.

The DC *I(V)* curve for one such diode (diode edge-length 400 nm) is shown in figure VI-7(b). The β of the fabricated diode, in figure VI-7(c), is lower compared to the simulated diodes. I suspect non-uniformity in the oxide growth across the first Ni layer, as shown later. We have fabricated diodes with β in the range of 1.5 – 3 A/W for small area diodes (250 nm to 800 nm) and R_D in the range of 50 – 300 Ω.

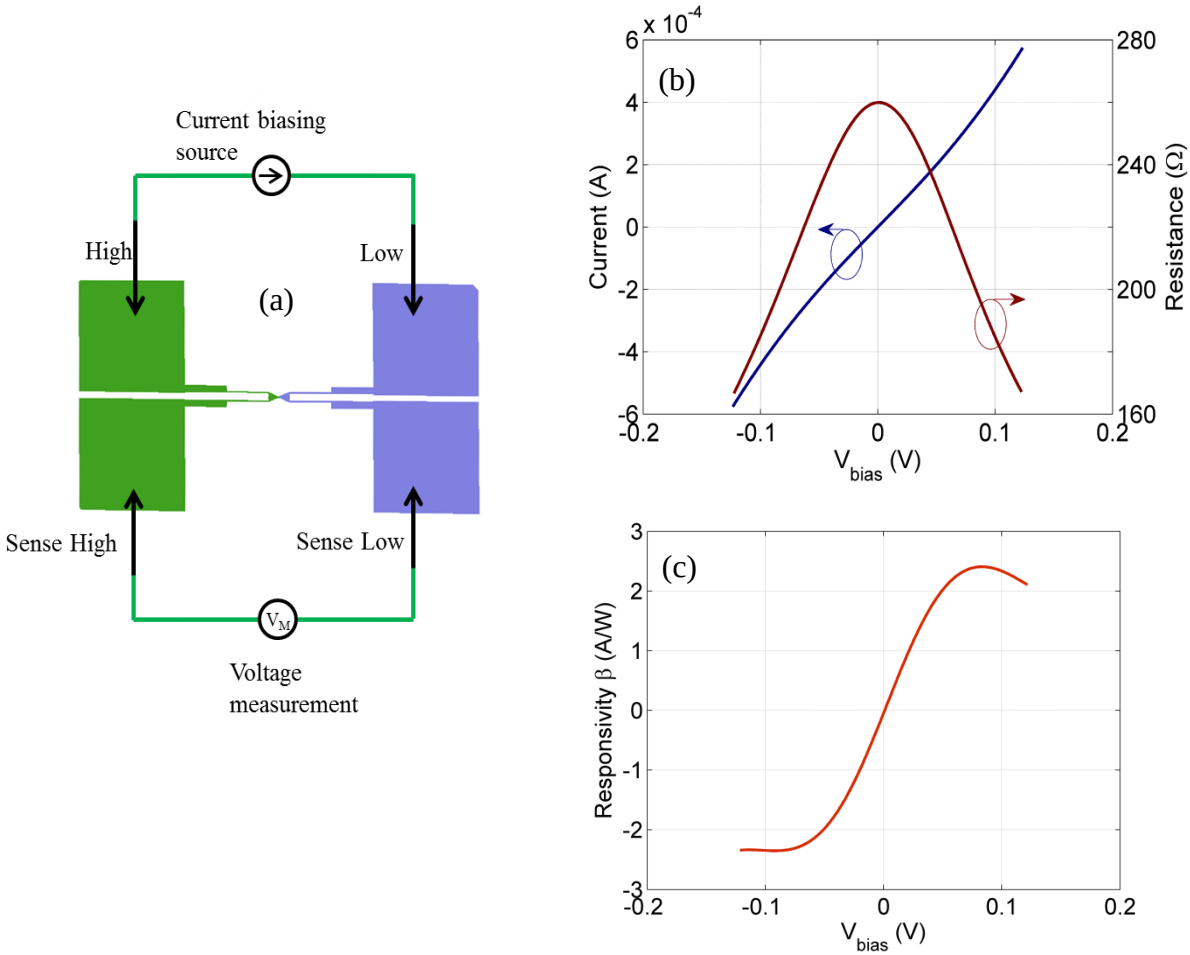

Figure VI-7. Schematic of measurement setup and measured DC characteristics of a Ni/NiO/Ni diode. (a) Setup used for diode DC current-voltage measurements. The setup consists of a current source and a voltage measurement unit. The probes connected to the device contact pads are labeled 'High', 'Low', 'Sense High', and 'Sense Low'. Current is applied between the 'High' and 'Low' probes. Voltage drop across the diode is measured between the 'Sense High' and 'Sense Low' probes using a voltage meter. (b) Measured DC *I(V)* and R_D vs. bias voltage characteristics of a square shaped Ni/NiO/Ni diode of size 250 nm fabricated using the overlap process and DUV

lithography to demonstrate the working of the diode. The target oxide thickness was 2 nm. (c) The calculated diode DC β ~2.3 A/W at a bias voltage of 0.08 V for the device in (b).

d. Device consistency

Even though the overlap and the four-layer process fabrication methods were a success, the diode characteristics were not consistent within a wafer, from device to device. We suspected that the inconsistency was due to the presence of photoresist near the diode junction, which resulted in an inconsistency in the barrier height and oxide thickness. More recently, we are fabricating diodes using a Ge shadow-mask process (Hobbs et al., 2005) and the device consistency has improved. A scanning electron micrograph of a Ni/NiO/Ni diode fabricated by Bradley Pelz using the Ge-shadow mask process is shown in figure VI-8.

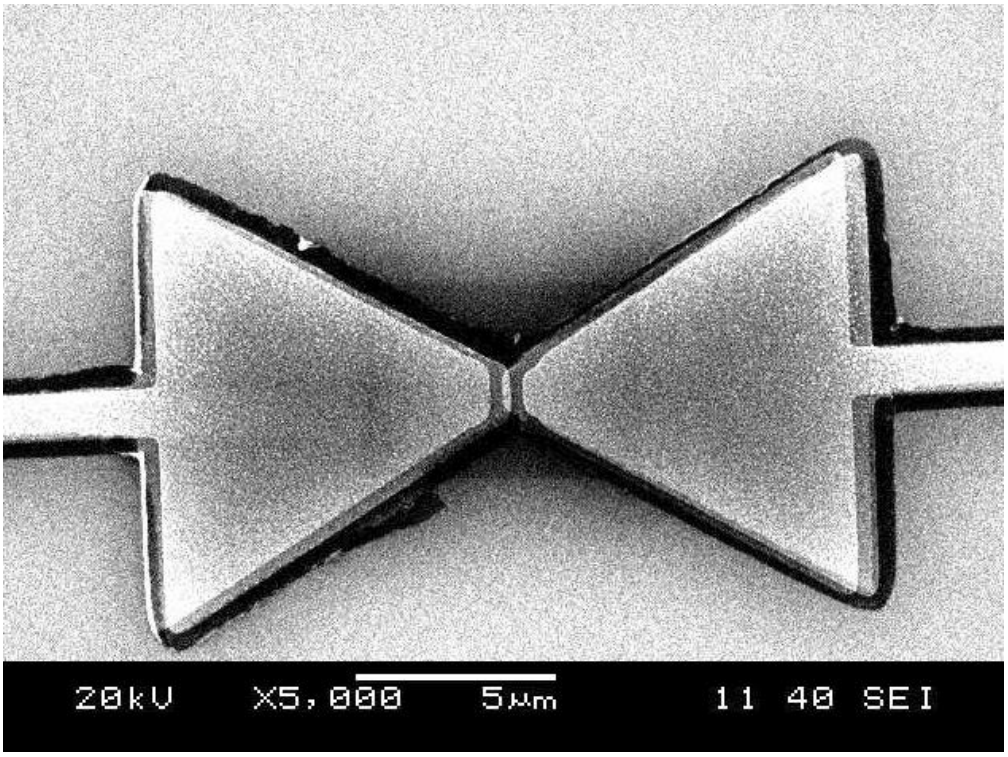

Figure VI-8. A scanning electron micrograph (SEM) of the Ni/NiO/Ni rectenna fabricated using the germanium shadow mask process. The diode junction is at the center where the two arms of the bowtie antenna meet. This bowtie antenna shown here is designed for 1 THz radiation in a medium designed for heat harvesting, not for 1 THz radiation in free space. The device was fabricated by Bradley Pelz.

The Ge-shadow mask process has improved the device consistency. In figure VI-9, I show a scatter plot of the R_D and β of devices fabricated using the overlap process and the shadow mask process. Although the β of the overlap devices is higher than the shadow mask diodes, their resistance is also high. This increase in β with R_D was typically observed in diodes with thick oxides, but it provides no advantage due to poor coupling efficiency of high R_D diodes with the antenna. The standard deviation in the R_D of overlap diodes is ~1100 Ω and for the shadow-mask diodes is ~15 Ω, and therefore the shadow-mask devices are superior from the point-of-view of diode consistency. Currently, the process is suitable for single insulator diodes, but some modifications could allow for making double insulator MIMs as well.

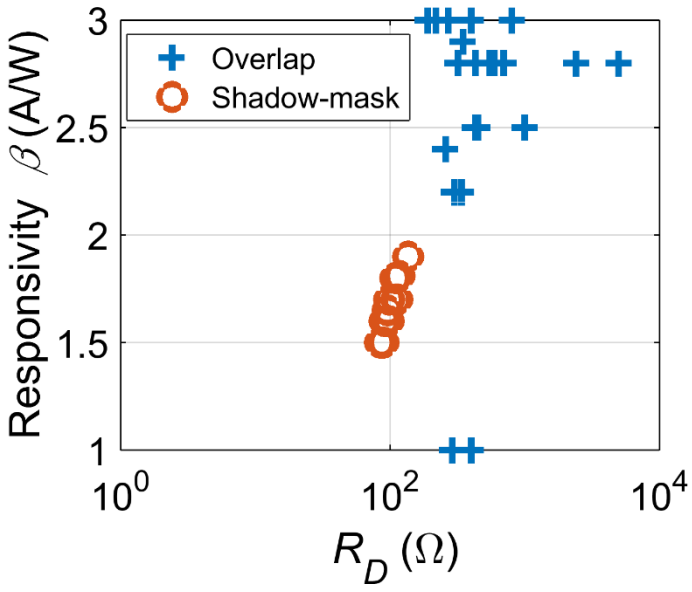

Figure VI-9. Scatter plots of the Ni/NiO/Ni diode showing the R_D vs β of a set of diodes in wafers fabricated using overlap process (blue pluses), and Ge shadow-mask process (orange circles). There is significantly reduced scatter from device to device in the Ge shadow-mask processed wafers. The oxidation conditions were the same for both the wafers.

e. Discrepancy with simulations

When I tried fitting the measured *I(V)* with the simulated *I(V)*, the results did not match each other well. Also, the R_D and β of the measured devices was unpredictable. I found that there could be three main reasons for this mismatch:

- Non-uniformity in the thickness of the nickel oxide across the device area: Presence of pinholes or regions with thin and thick oxide can reduce the β of the diode. In figure VI-10(a) and (b), I plot the simulated R_D and β for diodes with a 3.9 nm uniform oxide. The voltage at which the peak responsivity occurs in the 3.9 nm and 0.07 eV barrier simulations, matches that in the measured response. So to take the lower β and R_D into account, I proposed that the diode area had regions of 1 nm oxide and 3.9 nm thick oxide that covered 12% and 88% of the diode area, respectively. The thin oxide regions reduced the overall diode β to ~2 A/W. The resulting

simulated R_D and β characteristics of the non-uniform diode were close to the measured characteristics, as shown in figures VI-10(c) and (d). With change in the distribution of the oxide non-uniformity and the area, many diodes could be fitted with greater accuracy, compared to diodes simulated using uniform thickness. The theory was supported by the experimental observation that thicker (and possibly uniform) oxides gave higher β and a good match with simulations. If, in fact, the fabricated diodes do have multiple thicknesses, a solution to this is to use uniform oxides deposited by atomic layer deposition (Alimardani and Conley, 2013). Uniform oxides can give responsivities that approach 8 A/W, shown in figure VI-3.

- Surface of the underlying Ni is rough and polycrystalline: Studies on the roughness of the bottom metal layer and its polycrystalline structure have shown poor diode performance (Cowell et al., 2011). Leakage of current through the grain boundaries can result in a similar effect due to a non-uniform oxide. A solution is to use amorphous metal substrates that result in reduced roughness (Cowell et al., 2011), lower leakage currents in the diode, and might give a smoother oxide film.
- Alternate conduction mechanisms and presence of traps and surface states: Conduction mechanisms like trap-assisted tunneling and Poole-Frenkel effect affect the transport through the oxide and result in reduced nonlinearity (Alimardani et al., 2014b). Both mechanisms are a function of the density and number of traps in the oxide, and therefore might equally contribute to poor performance of diodes. When we fabricated Ni/NiO devices with different top metal layers (Pd, Cu, Ag), we did not see any significant effect of material asymmetry in the *I(V)* characteristics, suggesting the pinning of the metal work function at the NiO/metal

interface due to presence of surface states. A poor stoichiometry of the grown oxide could lead to traps and surface states.

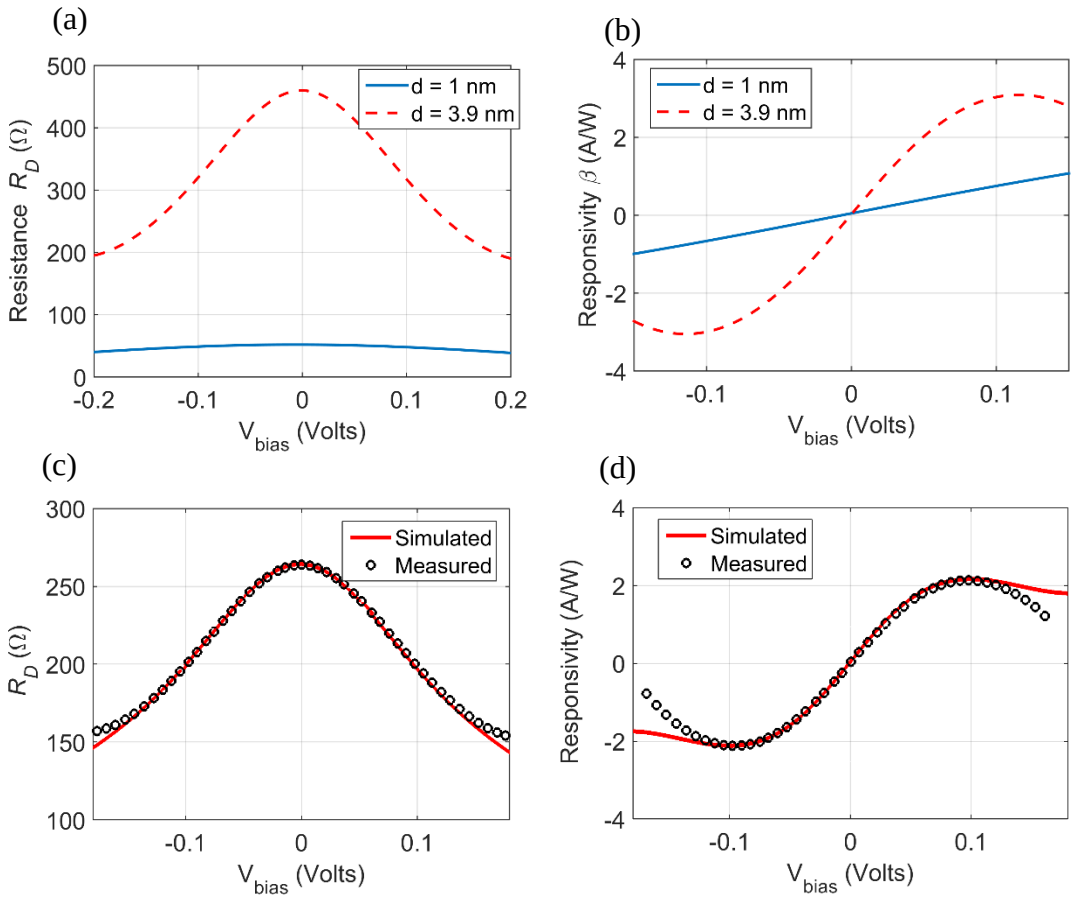

Figure VI-10. Effect of non-uniform insulator thickness from simulated and measured characteristics of a 300 nm x 300 nm Ni/NiO/Ni diode device fabricated using the overlap process. Simulated (a) R_D, and (b) β vs. voltage plots for uniform oxide thickness d = 1 nm and d = 3.9 nm (ϕ = 0.07 eV). (c) Plot of the measured R_D (black circles) and the simulated R_D (solid red line), and (d) measured β (black circles) and the simulated β (solid red line) of the diode vs. voltage. The simulated response in figures (c) and (d) is for a diode with regions of 3.9 nm and 1 nm thick oxide. The thin oxide regions (covering 12% of the diode area) reduce the R_D and β compared to the diode having uniform 3.9 nm oxide thickness shown in (b).

Each of the three mechanisms contributing to the poor responsivity of the fabricated devices could occur due to the poor structure of the underlying metal surface. The following steps could help eliminate the cause: improving the quality of the metal surface using smooth and amorphous electrodes (Cowell et al., 2011), using oxide growth methods such as sputter-etching (Heiblum et

al., 1978) to improve the quality of the oxide, and performing reflection electron energy loss spectroscopy (REELS) to determine the presence of traps and surface states in the oxide (Alimardani et al., 2014a), and adjusting the oxide growth conditions to reduce their effect on electron transport.

We are currently working on improving the quality of the oxide using methods such as ozone oxidation of metal surfaces (Ramanathan et al., 2003), and investigating the possibility of using sputtering and atomic layer deposition of electrodes to get smoother substrates.

f. Device measurements at terahertz frequencies

The terahertz measurements were performed with Zachary Thacker at the University of Missouri – Columbia using a modified terahertz time-domain spectroscopy setup (Mickan and Zhang, 2003), shown in figure VI-11.

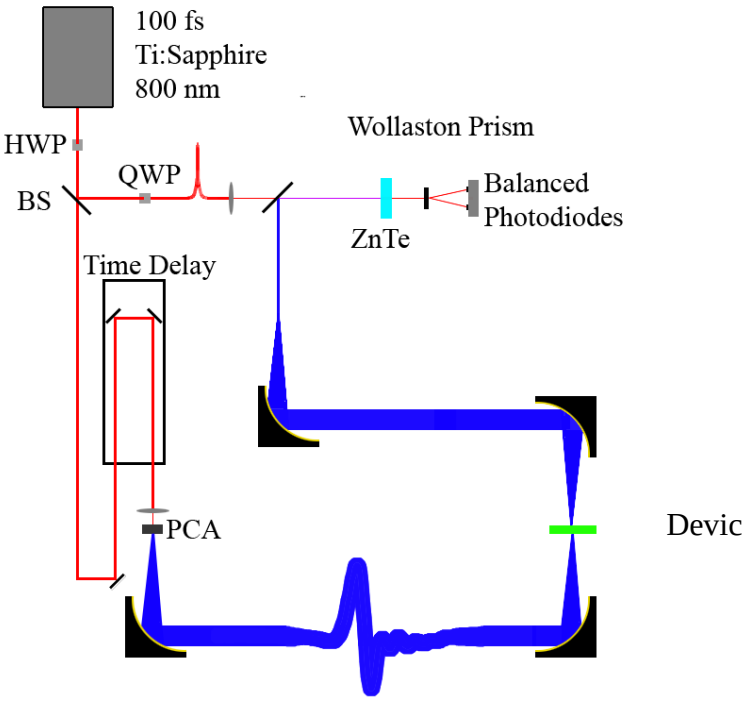

Figure VI-11. Setup for generating terahertz waves. The source is a 100 fs Ti:Sapphire laser that excites a biased photoconductive antenna (PCA) made of a dipole antenna on a GaAs wafer. Incident laser excites electrons across the two arms of the dipole antenna to modify the shape of the 100 fs pulse and generate terahertz waves. This setup was assembled by Zachary Thacker at the University of Missouri-Columbia. Image courtesy of Zachary Thacker.

The THz power spectrum from the photo-conductive antenna (PCA) was broadband with a bandwidth of ~1 THz and a peak in the spectrum at 800 GHz. The antenna was designed to work at 750-850 GHz and the power from the source in this frequency range was ~19 nW. The device electrical measurement setup during illumination was the same as in figure VI-7. For a typical good device, we observed a rectenna current of 8.5 nA at a bias voltage of ~0.08 V with a terahertz illumination of 19 nW absorbed by the antenna. This corresponds to a system responsivity of 0.44 A/W. The system NEP value was calculated to be 4.3×10^{-11} $WHz^{-1/2}$ (Zhu, 2014). The bias dependence of the rectified current was also as expected. In figure VI-12 I show the DC rectified current response, in arbitrary units, vs. the bias voltage applied to the diode. The rectified current is only a small fraction (~10^{-6}) of the DC bias current, which is not shown in the figure. The

response matches well with the shape of the expected output calculated using the η_C and the measured DC β of the diode. Since the contribution of shot noise to the NEP is of the same order of magnitude as the Johnson noise, the device would perform better if operated at zero bias, requiring zero-biased diodes.

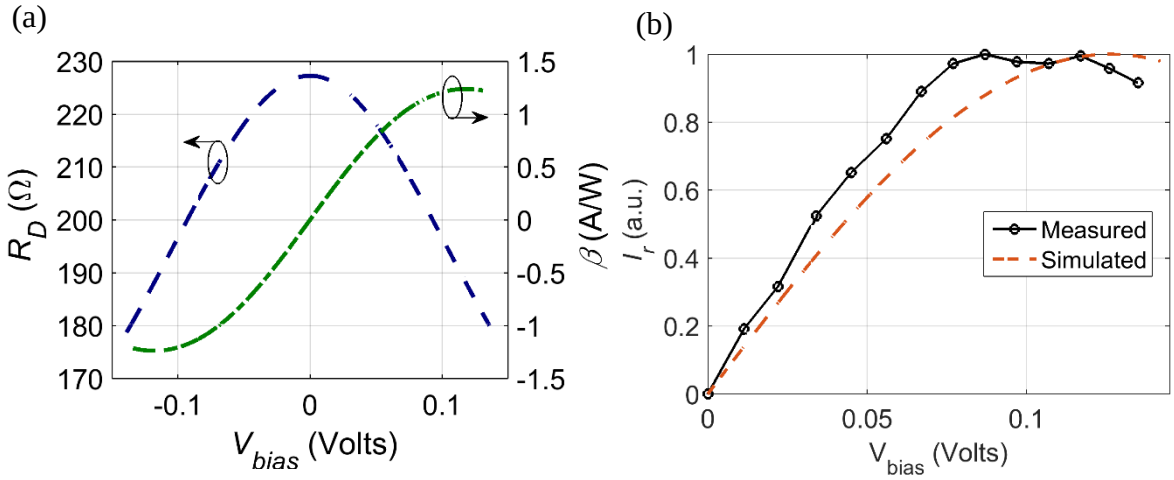

Figure VI-12. Ni/NiO/Ni diode DC characteristics and response of the terahertz rectenna device fabricated using the overlap process and DUV lithography. (a) Measured DC R_D (dashed blue line) and β (dash-dot green line) plots of the 400 nm x 400 nm Ni/NiO/Ni diode, and (b) bias dependence of the measured (black circles) and simulated (dotted red line) rectified current (I_r) from the rectenna under terahertz illumination. The simulated optical response (normalized) is calculated using the measured DC *I(V)* and η_C from Eq. VI-2, assuming a 3.5 nm oxide having a relative permittivity of 6.5. The rectified current has the same bias dependence as the simulated response. The small discrepancy between them is possible due to the assumption that the beam is monochromatic at 800 GHz.

F. Ni/NiO/Pt zero-biased diodes for terahertz rectennas

We also fabricated asymmetric Ni/NiO/Pt diodes to achieve a finite β at zero bias. The advantage of using zero-biased diodes is a reduction in the additional shot noise due to the absence of an applied DC current, and an improved NEP (Zhu, 2014). The measured R_D and β vs. voltage curves are plotted in figure VI-13(a) and VI-13(b), respectively. There is a small asymmetry in the diode R_D, and the β at zero bias is ~0.15 A/W. The R_D = 110 Ω for a ~700 nm x 300 nm diode.

The rectenna can detect high frequency terahertz radiation without the need for an external bias voltage.

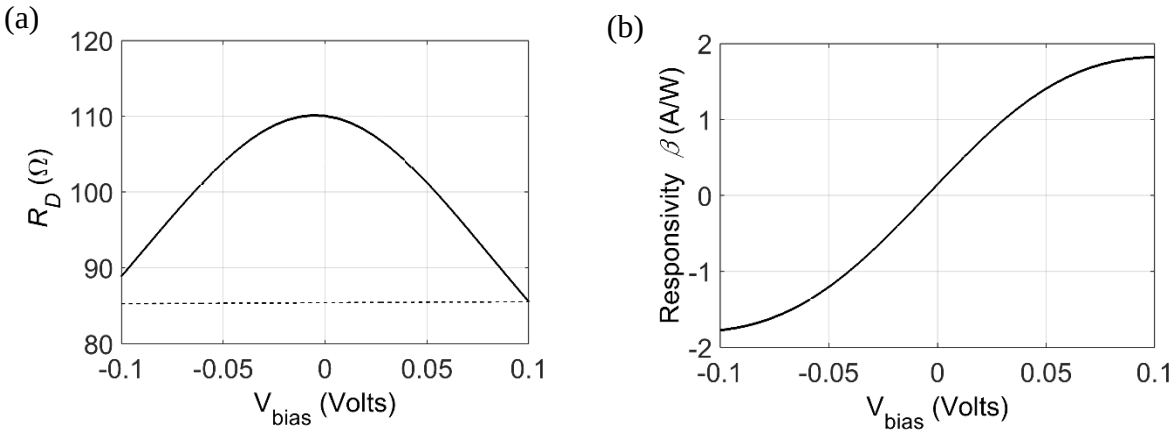

Figure VI-13. Measured characteristics of a 700 nm x 300 nm Ni/NiO/Pt diode fabricated using the shadow-mask process. (a) R_D vs. voltage characteristics of the diode. The plot is slightly asymmetric as indicated by the dotted black line which shows a difference in the diode resistance at +/−0.1 V due to the asymmetric Ni/NiO/Pt barrier. (b) The β vs. voltage characteristics of the diode. The β at zero bias is ~0.15 A/W.

The poor β of the fabricated diode compared to the simulated device suggests the same issues are in play as presented before for the Ni/NiO/Ni diode. However, these devices are currently being used in 28 THz traveling-wave diodes and have shown promising response at zero-bias demonstrating that the device works without the need of an external bias voltage (Pelz, University of Colorado - Boulder).

G. Conclusion

In this chapter, I discussed the design and characterization of MIM diodes for 1 THz detection. The design of MIM diodes for terahertz applications requires low insulator dielectric constant, small diode size, low metal/insulator barrier height and a thin insulator thickness. I chose the Ni/NiO/Ni diode for biased detection at 1 THz due to its low barrier height, low dielectric constant, and ease of fabrication. The diodes were initially fabricated using an overlap process and later a

shadow mask process and gave a responsivity (β) of 2.5-3 A/W at bias with diode resistance (R_D) ~50-300 Ω to match with the antenna. The diodes responded successfully to terahertz illumination giving a system β ~0.44 A/W. DC *I(V)* measurement results of the Ni/NiO/Pt diode for zero-bias detection showed that the device had a finite zero-bias responsivity. The experimentally measured DC β was lower than the simulated β of the diode and I suspect three potential reasons for the decrease in the diode nonlinearity: the polycrystalline nature of the metal, non-uniform thickness of the oxide, or the presence of traps and defect states that influence electron transport. Efforts to improve the quality of the bottom electrode and the oxide are in progress.

CHAPTER VII

INFRARED OPTICAL RESPONSE OF GEOMETRIC DIODE RECTENNAS

A. Introduction

As discussed in Chapter VI and in Grover and Moddel (2011), MIM diodes in their current configuration are limited in operating frequency due to large *RC* response time and poor impedance match with the antenna, and cannot be used for power conversion at frequencies approaching the near infrared and the visible.

In this chapter, I describe the demonstration of the 10.6 μm (28 THz) optical response of geometric diodes (Moddel, 2014; Zhu et al., 2011; Joshi et al., 2012; Moddel et al., 2012; Zhu et al., 2013b; Zixu Zhu et al., 2014), potentially paving way to graphene-based rectennas for high-speed electronics and energy harvesting.

B. Geometric diode operation

The geometric diode, as discussed in (Moddel et al. 2012), is an inverse arrowhead-shaped graphene device, enjoying the advantage of having a very low capacitance of the order of a few attofarads, due to its planar structure (Zhu et al., 2013b). This gives the device a low *RC* time constant and a cutoff frequency of ~100 THz.

The diode-like behavior of the geometric device arises from its asymmetric structure, which allows for the preferential flow of charge carriers in one direction. As shown in figure VII-1, the diode acts as a funnel for flow of carriers moving from left to right, with restricted flow in the opposite direction. The device is a thin film patterned such that the asymmetric constriction at the neck region is of the order of or smaller than the mean-free-path length (MFPL) of the charge

carriers. This size constraint is required to achieve current rectification so that the charge carriers 'see' the spatial geometric asymmetry. Such a stringent constraint is realized in graphene (Castro Neto et al., 2009), where the MFPL of charge carriers can be an order of magnitude larger than those in metals at room temperature.

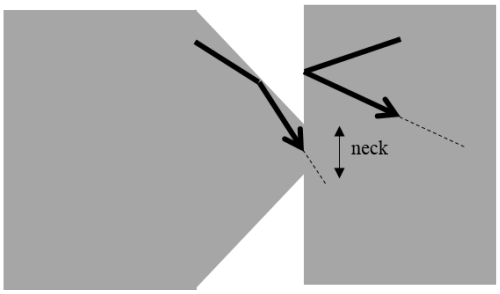

Figure VII-1. Illustration of the operation of a geometric diode. Charge carriers moving from left to right are reflected by the walls of the diode and funneled through the neck, but those moving from right to left are reflected back, giving an asymmetry to the diode *I(V)* characteristics.

Using Monte Carlo simulations of Drude charge carriers (Zhu, 2014; Zhu et al., 2013b) found that the *I(V)* of the geometric diode is asymmetric. Quantum simulations based on the non-equilibrium Green's function method (Grover, 2011) predicted similar results.

C. Device fabrication and electrical measurements

Geometric diodes were fabricated using e-beam lithography and low power oxygen plasma etching of single layer graphene exfoliated onto a 90 nm oxidized silicon wafer. Thermal evaporation and lift-off of Cr/Au metal contacts formed a four-point probe configuration. The devices had a neck width of 70 nm and shoulder width of 400 nm. The measured *I(V)* characteristics are shown in figure VII-2(a). In figure VII-2(b), I show the asymmetric resistance and responsivity of the device. I estimated the MFPL of electrons to be ~50 nm using field-effect measurements on a graphene structure defined adjacent to the geometric diode (Nayfeh, 2011).

Although this value is at the edge of the neck width, the responsivity of these un-optimized devices is substantial.

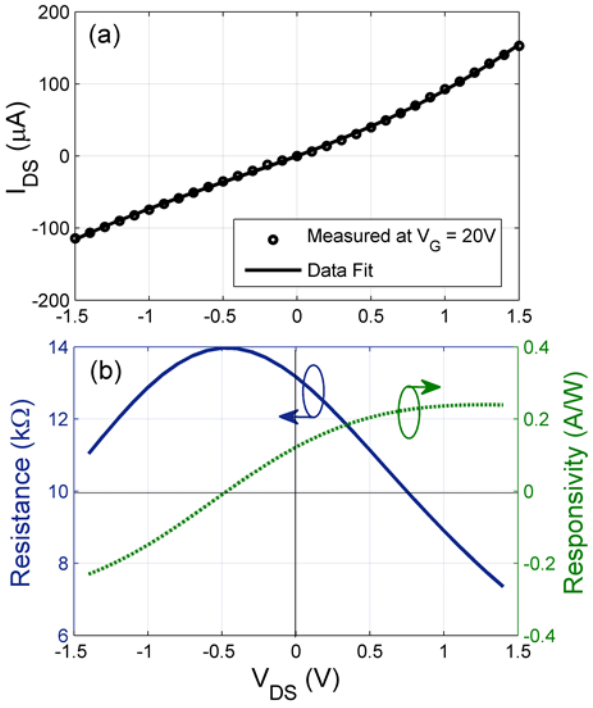

Figure VII-2. Measured DC characteristics of a geometric diode. (a) Drain-source current vs. voltage [$I_{DS}(V)$] characteristics, and (b) resistance and responsivity as a function of drain-source bias (V_{DS}) for gate voltage V_G = 20 V. The responsivity is a measure of the output DC current as a function of the input AC power. The diode has a non-zero DC responsivity at zero-bias.

For the optical measurements, the rectenna consisted of a 5.1 μm long bowtie antenna made up of two opposing 2.3 μm triangular sections, as shown in figure VII-3, and a 500 nm long geometric diode at the center.

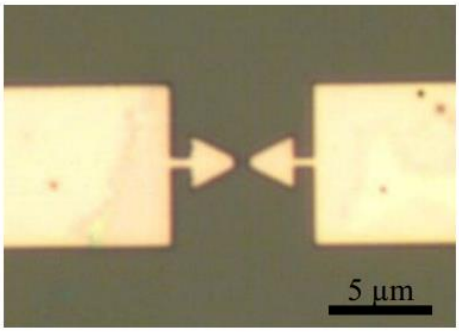

Figure VII-3. Optical microscope image of the bowtie antenna coupled to a geometric diode. The scale bar shown is 5 µm. The diode (not shown) is placed at the center of the antenna gap. Zixu Zhu fabricated the devices (Zhu, 2014).

I measured the response of the geometric diode rectenna using a 10.6 µm wavelength (28 THz) laser source. The measurement setup is shown in figure VII-4. A CO_2 laser (Synrad Model 48-1 SWJ) with intensity controlled by a pulse generator was used to illuminate the bowtie antenna of the rectenna. The chopping frequency of the laser beam was ~280 Hz and this value was fed to the lock-in amplifier (Stanford Research Systems SR830). I positioned the IR laser beam on the device using a He-Ne laser beam aligned with the CO_2 laser beam. The electrical measurement setup used a mercury switch that allowed the probes to stay at ground potential and prevent any damage to the geometric diode due to static discharge, when not in measurement. The output voltage and current was measured by the lock-in amplifier using a two-point measurement setup, and no voltage applied to the device. Using a half-wave plate, I rotated the polarization of the laser beam with respect to the antenna polarization to investigate the angular dependence of the response.

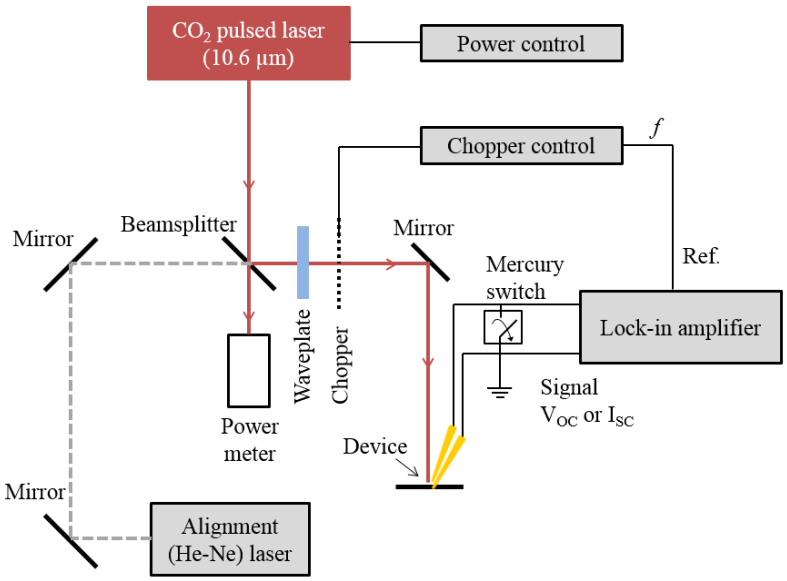

Figure VII-4. Setup for optical response measurement of geometric diode rectennas. The CO_2 laser emits a 28 THz beam that is directed to the device using a set of mirrors. The beam is aligned with the device using a He-Ne laser. The device current and voltage response is measured using two probes and the output is sent to a lock-in amplifier that is locked in to the laser chopping frequency. A half-wave plate is used to study the polarization response of the rectenna by rotating the polarization of the beam.

The spatial intensity of the laser beam fitted to the measured power using a Gaussian profile is shown in figure VII-5. The laser intensity at the device was estimated to be ~50 mW/mm^2, assuming the device was 1-2 mm offset from the center of the laser beam.

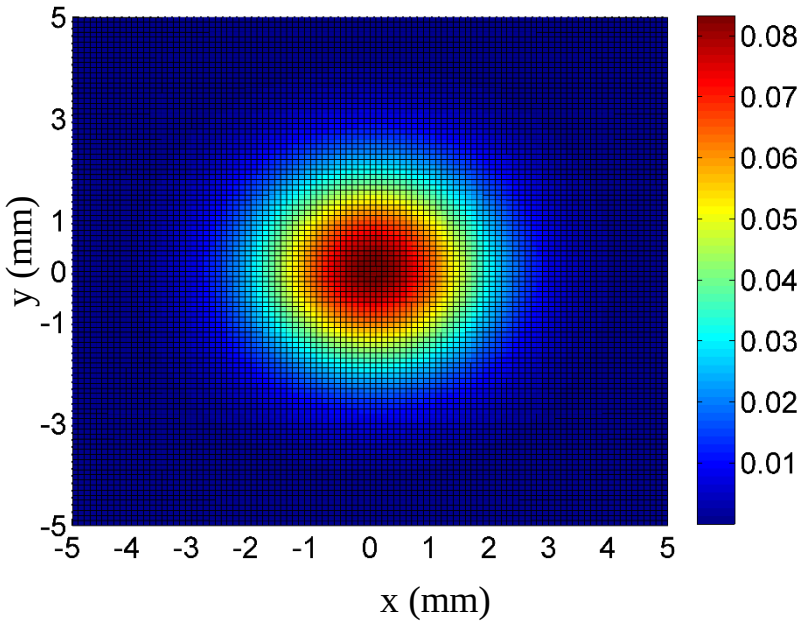

Figure VII-5. Intensity (W/mm^2) profile of the 28 THz laser beam, obtained by measuring the power near the device as a function of distance (in mm) and fitting to a Gaussian profile. The peak intensity at the center of the beam is ~80 mW/mm^2.

The geometric diode voltage response, shown in figure VII-6, is a cosine-squared function of the polarization angle with respect to the antenna axis (González and Boreman, 2005), which shows that it is due to absorption by the antenna. This demonstrates the rectifying behavior of the geometric diode at 28 THz. In figure VII-7, I show an approximately linear increase in the open circuit voltage with input power for different polarization angles.

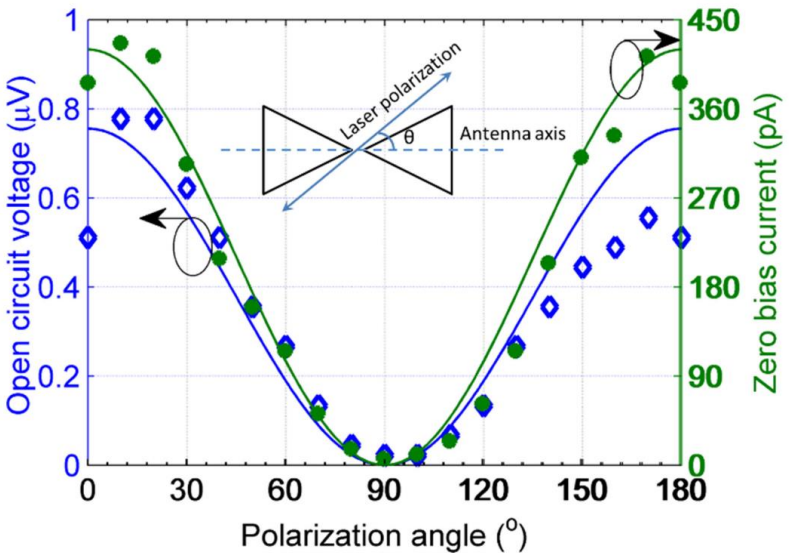

Figure VII-6. Polarization response of the geometric diode rectenna to 28 THz laser. The response follows the cosine-squared characteristics, as expected for a bowtie antenna. The peak current response (filled green circles) is ~420 pA and occurs when the antenna and the polarization of the beam are aligned with each other. The response decreases to zero when the antenna and the laser polarization are not aligned. Shown in the inset is an illustration of the laser polarization relative to the antenna axis.

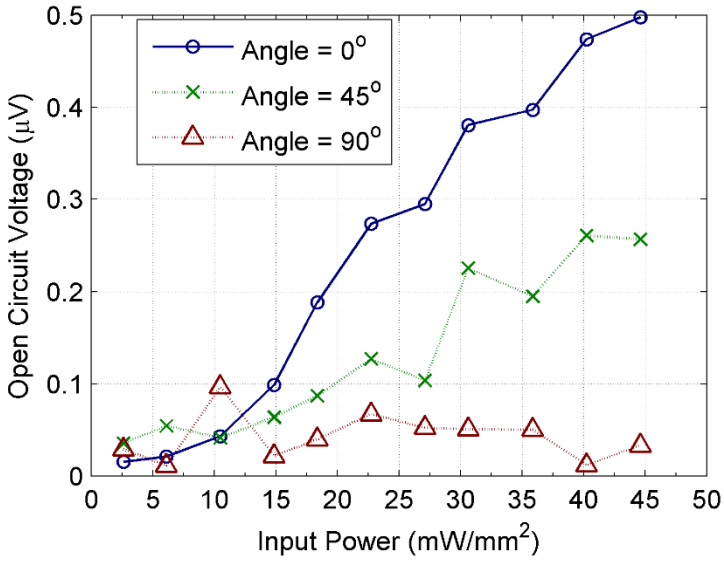

Figure VII-7. Open-circuit voltage response of the rectenna versus laser input intensity at three polarization angles: 0°, 45° and 90°. The response at 0° (blue circles) indicates perfect alignment between the laser polarization and the antenna. At 90° (red triangles), the antenna is perpendicular to the laser polarization and gives a near zero output voltage at all input intensities.

I estimated the responsivity of the device to be ~0.2 mA/W, based on an input intensity of 50 mW/mm^2 from figure VII-5, and an antenna area of 37 μm^2 (González and Boreman, 2005). (Zixu Zhu et al., 2014) calculated the noise equivalent power (NEP) of the metal antenna / graphene geometric diode rectenna IR detector to be 43 nW $Hz^{-1/2}$, showing that the graphene geometric diode is among the best room-temperature detectors for 28 THz detection.

Geometric diode rectennas potentially have application in thermophotovoltaics (TPV). Conventional TPV, which incorporates semiconductor junction solar cells, is limited to near-visible operation. Since rectenna solar cells operate in the IR – with design constraints that are more easily met than for the visible because of the lower frequency of IR light – they are better suited for TPV. There is a lot of room for improving the efficiency of the geometric diode rectenna by using higher asymmetry diode designs (Zhu, 2014), and better antenna design for efficient capture of broadband IR radiation.

D. Conclusion

In this chapter, I demonstrated the response of an antenna-coupled geometric diode to terahertz radiation (28 THz). Geometric diodes have a planar structure that improves *RC* response over parallel-plate devices, allowing for operation at THz frequencies. Diodes with asymmetric *I(V)* characteristics and having substantial zero bias responsivity were coupled to bowtie antennas designed for operation at 28 THz. The rectenna device response is polarization-dependent and validates operation of the device at IR frequencies. Further improvement in device and antenna design is expected to provide an efficient device. The device has potential to be used for thermophotovoltaic energy conversion.

CHAPTER VIII

CONCLUSIONS AND FUTURE WORK

A. Summary and conclusions

The goal of my thesis research was to analyze the performance limits of optical rectennas for detection and energy harvesting. I worked towards the goal by applying the quantum theory of photon-assisted tunneling (PAT) and developing a method to calculate the optical response of a diode in a rectenna using a simple equivalent electrical circuit. By studying the response of rectennas in the energy harvesting mode and solving for the time-dependent diode currents and voltages using PAT theory, I calculated the power conversion efficiency limits of rectennas under monochromatic illumination and when used as solar cells. I found that for diodes that are optimally matched to antennas, monochromatic power conversion efficiencies approach 100% and the multispectral efficiency is limited to 44% at solar terrestrial intensities, which is the same as the ultimate efficiency of conventional solar cells.

Developing the rectenna PAT theory further, I found that there is a correspondence between the quantum and the classical approaches. Rectennas follow Einstein's photon-based approach if the amplitude of the diode voltage (V_D) is less than the photon energy divided by the electronic charge ($\hbar\omega/q$), and follow Maxwell's classical electromagnetic wave nature of light if $V_D \gg \hbar\omega/q$. The correspondence between classical and quantum operation of the rectenna allows classical operation at optical and IR frequencies for high incident intensity and for large source and diode impedances. This is useful to improve the conversion efficiency of broadband rectennas for harvesting blackbody radiation, including solar radiation, beyond the quantum limit. The power

conversion efficiency of solar rectennas can exceed the 44% limit for conventional semiconductor solar cells if classical operation can be achieved.

Based on diode requirements from PAT for efficient energy harvesting, I worked towards improving diode characteristics. I analyzed resonant and step metal/insulator/insulator/metal (MIIM) diode designs and presented guidelines to improve their asymmetry and reduce the diode turn-on voltage. I calculated their rectification efficiency for different diode sizes and different input frequencies. An efficiency calculation of rectenna performance under monochromatic illumination showed that despite improvement in diode asymmetry, the diode performance was poor due to inefficient coupling with the antenna and a finite reverse leakage current. These issues are critical to the operation of a rectenna at high frequencies, but are often neglected in literature. Designing better diodes requires further work and new design ideas.

Because of the complexity of the efficiency calculations, many rectenna diodes have been reported without indications of how well these diodes will function in a rectenna. I presented a simple figure of merit to estimate rectenna performance for a given diode, using a combination of the three mechanisms that determine rectenna performance: the diode reverse leakage power relative to the input power, diode responsivity, and the coupling efficiency between the antenna and the diode. I calculated the *FOM* using different rectenna parameters and input conditions, compared the results with conversion efficiency calculated using PAT theory and showed a strong correlation between the two. Applying the *FOM* to MIIM diodes showed that the simple expression can be used to provide a good estimate of the rectenna performance under monochromatic illumination.

One of my projects involved the design of terahertz rectennas for detection. In Grover and Moddel (2011), it was shown that MIM diodes are not suitable for solar energy harvesting, but they work well at terahertz frequencies. The design of MIM diodes for terahertz detection requires low insulator dielectric constant, small diode size, low metal/insulator barrier height and a thin insulator. I chose the Ni/NiO/Ni diode for biased detection at 1 THz due to its low barrier height, low dielectric constant, and ease of fabrication. The diodes were initially fabricated using an overlap process and later a shadow mask process, and gave a responsivity of 2.5-3 A/W at bias with a ~100 Ω resistance to match with an antenna. The diodes responded to terahertz illumination giving a system responsivity of 0.44 A/W. In chapter VI, I also presented DC *I(V)* measurement results of the Ni/NiO/Pt diode for zero-bias detection. The experimentally measured DC responsivity was lower than the simulated responsivity of the diode and I gave three potential reasons for the decrease in the diode nonlinearity: non-uniform thickness of the oxide, the polycrystalline nature and surface roughness of the metal layers, or the presence of conduction mechanisms such as trap-assisted transport and Frenkel-Poole effect, in addition to tunneling. Efforts to improve the quality of the bottom electrode and the oxide are in progress using smoother electrodes and more uniform oxide films.

Finally, I measured the optical response of geometric diodes at 28 THz. These diodes have a planar structure that improves *RC* response over parallel-plate MIM devices, allowing for operation at IR wavelengths. Geometric diodes with asymmetric *I(V)* characteristics and having substantial zero bias responsivity, were coupled to bowtie antennas designed for operation at 10.6 μm wavelength. The rectenna device response was shown to be polarization-dependent and validated operation of the device at IR frequencies.

B. Future work

This work provides further insight into the three approaches for improving the conversion efficiency of optical rectennas,

1. Beyond the 44% quantum efficiency limit: I showed that the conversion efficiency of rectennas can exceed the 44% limit if classical operation can be achieved. There are two ways to achieve classical operation, increasing the input intensity and the antenna radiation resistance. However there are some problems related to:
    a. Improving the spatial coherence of radiation from thermal sources: The limited spatial coherence of blackbody radiation and small incident power relative to the photon energy makes classical operation of rectennas at visible and IR frequencies challenging. It has been shown that radiation from blackbody sources can be made partially coherent in the near field using polar materials (Greffet et al., 2002). Such methods of improving the coherence from hot sources can help increase the input power available to the rectenna, potentially allowing classical operation and easing turn-on voltage and reverse leakage current restrictions on diode design. It is unclear whether this can be applied for radiation from the sun.
    b. Compensation of the diode capacitance: Because increasing the antenna radiation resistance for classical operation requires increasing the diode resistance, this method requires compensation of the capacitance of the diode. Several methods are used in the microwave region to provide good impedance match between the antenna and the diode (Chang, 2004). If a similar approach is used at IR and optical frequencies, it could be possible to compensate for the increased *RC* time constant, at the cost of reduced rectenna bandwidth.

2. Improving diode design to rectify energy from low intensity sources: Further tuning of diode parameters following the guidelines presented in chapter V, and new diode designs and tailored materials are required to enhance the rectification efficiency of MIM diodes for infrared energy harvesting.
3. Using hot (cold) resistors or antennas connected to cold (hot) diodes to harvest energy from thermal noise: A hot resistor generates noise spectral density according to the 1D Planck distribution function (Oliver, 1965; Yu et al., 2014). Recently (Byrnes et al., 2014) proposed the use of a rectenna to make an emissive energy harvester, a device that generates energy by emitting thermal radiation to clear sky. The calculations presented in chapter I can be applied to determine the rectification response of such device, or a diode connected to any antenna/resistor. However, as the radiation corresponds to infrared wavelengths, these devices face similar limitations as rectennas and new ideas are required to implement them.

To conclude, rectennas are an exciting and practical concept with the potential to harvest radiant energy from many different energy sources and detect a range of electromagnetic frequencies from microwaves up to the visible, including in the so called 'terahertz gap' (Chamberlain, 2004). As with every breakthrough technology, rectenna technology is challenging and requires new ideas, their proper implementation, and efficient design to replace the conventional and existing non-conventional energy sources.

REFERENCES

Alimardani, N., Conley, J.F., 2013. Step tunneling enhanced asymmetry in asymmetric electrode metal-insulator-insulator-metal tunnel diodes. Appl. Phys. Lett. 102, 143501. doi:10.1063/1.4799964

Alimardani, N., King, S.W., French, B.L., Tan, C., Lampert, B.P., Jr, J.F.C., 2014a. Investigation of the impact of insulator material on the performance of dissimilar electrode metal-insulator-metal diodes. J. Appl. Phys. 116, 024508. doi:10.1063/1.4889798

Alimardani, N., McGlone, J.M., Wager, J.F., Jr, J.F.C., 2014b. Conduction processes in metal–insulator–metal diodes with Ta2O5 and Nb2O5 insulators deposited by atomic layer deposition. J. Vac. Sci. Technol. A 32, 01A122. doi:10.1116/1.4843555

Bailey, R.L., 1972. Proposed new concept for a solar-energy converter. J Eng Power 94, 73–77.

Bareiß, M., Ante, F., Kälblein, D., Jegert, G., Jirauschek, C., Scarpa, G., Fabel, B., Nelson, E.M., Timp, G., Zschieschang, U., Klauk, H., Porod, W., Lugli, P., 2012. High-Yield Transfer Printing of Metal–Insulator–Metal Nanodiodes. ACS Nano 6, 2853–2859. doi:10.1021/nn3004058

Berland, B., 2003. Subcontractor Report. National Renewable Energy Laboratory. Subcontract. Rep. NREL/SR-520-33263.

Bolivar, P.H., Brucherseifer, M., Gómez Rivas, J., Gonzalo, R., Ederra, I., Reynolds, A.L., Holker, M., de Maagt, P., 2003. Measurement of the dielectric constant and loss tangent of high dielectric-constant materials at terahertz frequencies. IEEE Trans. Microw. Theory Tech. 51, 1062–1066. doi:10.1109/TMTT.2003.809693

Briones, E., Alda, J., González, F.J., 2013. Conversion efficiency of broad-band rectennas for solar energy harvesting applications. Opt. Express 21, A412. doi:10.1364/OE.21.00A412

Brown, W., 1973. Adapting Microwave Techniques to Help Solve Future Energy Problems. Microw. Theory Tech. IEEE Trans. On 21, 753 – 763. doi:10.1109/TMTT.1973.1128128

Brown, W.C., 1969. Experiments Involving a Microwave Beam to Power and Position a Helicopter. Aerosp. Electron. Syst. IEEE Trans. On AES-5, 692 –702. doi:10.1109/TAES.1969.309867

Byrnes, S.J., Blanchard, R., Capasso, F., 2014. Harvesting renewable energy from Earth's mid-infrared emissions. Proc. Natl. Acad. Sci. 111, 3927–3932. doi:10.1073/pnas.1402036111

Cahay, M., McLennan, M., Datta, S., Lundstrom, M.S., 1987. Importance of space-charge effects in resonant tunneling devices. Appl. Phys. Lett. 50, 612–614. doi:doi:10.1063/1.98097

Castro Neto, A.H., Guinea, F., Peres, N.M.R., Novoselov, K.S., Geim, A.K., 2009. The electronic properties of graphene. Rev. Mod. Phys. 81, 109–162. doi:10.1103/RevModPhys.81.109

Chamberlain, J.M., 2004. Where optics meets electronics: recent progress in decreasing the terahertz gap. Philos. Trans. R. Soc. Lond. Math. Phys. Eng. Sci. 362, 199–213. doi:10.1098/rsta.2003.1312

Chang, K., 2004. RF and Microwave Wireless Systems. John Wiley & Sons.

Choi, K., Yesilkoy, F., Ryu, G., Cho, S.H., Goldsman, N., Dagenais, M., Peckerar, M., 2011. A Focused Asymmetric Metal-Insulator-Metal Tunneling Diode: Fabrication, DC Characteristics and RF Rectification Analysis. IEEE Trans. Electron Devices 58, 3519 – 3528. doi:10.1109/TED.2011.2162414

Corkish, R., Green, M.A., Puzzer, T., 2002. Solar energy collection by antennas. Sol. Energy 73, 395–401. doi:10.1016/S0038-092X(03)00033-1

Cowell, E.W., Alimardani, N., Knutson, C.C., Conley, J.F., Keszler, D.A., Gibbons, B.J., Wager, J.F., 2011. Advancing MIM Electronics: Amorphous Metal Electrodes. Adv. Mater. 23, 74–78. doi:10.1002/adma.201002678

Dayem, A.H., Martin, R.J., 1962a. Quantum Interaction of Microwave Radiation with Tunneling Between Superconductors. Phys. Rev. Lett. 8, 246–248. doi:10.1103/PhysRevLett.8.246

Dayem, A.H., Martin, R.J., 1962b. Quantum Interaction of Microwave Radiation with Tunneling Between Superconductors. Phys. Rev. Lett. 8, 246–248. doi:10.1103/PhysRevLett.8.246

Elchinger, G.M., Sanchez, A., Davis, C.F., Javan, A., 1976. Mechanism of detection of radiation in a high-speed metal-metal oxide-metal junction in the visible region and at longer wavelengths. J. Appl. Phys. 47, 591–594. doi:doi:10.1063/1.322674

Eliasson, B.J., 2001. Ph.D. Thesis. University of Colorado, Boulder.

Eliasson, B.J., Moddel, G., 2003a. Metal-oxide electron tunneling device for solar energy conversion. 6534784.

Eliasson, B.J., Moddel, G., 2003b. Metal-oxide electron tunneling device for solar energy conversion. US Patent 6534784.

Estes, M.J., Moddel, G., 2007. Surface plasmon devices. US7177515 B2.

Fumeaux, C., Herrmann, W., Kneubühl, F.K., Rothuizen, H., 1998. Nanometer thin-film Ni–NiO–Ni diodes for detection and mixing of 30 THz radiation. Infrared Phys. Technol. 39, 123–183. doi:10.1016/S1350-4495(98)00004-8

González, F.J., Boreman, G.D., 2005. Comparison of dipole, bowtie, spiral and log-periodic IR antennas. Infrared Phys. Technol. 46, 418–428. doi:10.1016/j.infrared.2004.09.002

Goswami, D.Y., Vijayaraghavan, S., Lu, S., Tamm, G., 2004. New and emerging developments in solar energy. Sol. Energy 76, 33–43. doi:10.1016/S0038-092X(03)00103-8

Greffet, J.-J., Carminati, R., Joulain, K., Mulet, J.-P., Mainguy, S., Chen, Y., 2002. Coherent emission of light by thermal sources. Nature 416, 61–64. doi:10.1038/416061a

Grossman, E.N., Harvey, T.E., Reintsema, C.D., 2002. Controlled barrier modification in Nb/NbOx/Ag metal insulator metal tunnel diodes. J. Appl. Phys. 91, 10134–10139. doi:10.1063/1.1471385

Grover, S., 2011. Diodes for Optical Rectennas. PhD Thesis Univ. Colo.

Grover, S., Dmitriyeva, O., Estes, M.J., Moddel, G., 2010a. Traveling-Wave Metal/Insulator/Metal Diodes for Improved Infrared Bandwidth and Efficiency of Antenna-Coupled Rectifiers. IEEE Trans. Nanotechnol. 9, 716 –722. doi:10.1109/TNANO.2010.2051334

Grover, S., Dmitriyeva, O., Estes, M.J., Moddel, G., 2010b. Traveling-Wave Metal/Insulator/Metal Diodes for Improved Infrared Bandwidth and Efficiency of Antenna-Coupled Rectifiers. IEEE Trans. Nanotechnol. 9, 716 –722. doi:10.1109/TNANO.2010.2051334

Grover, S., Joshi, S., Moddel, G., 2013. Quantum theory of operation for rectenna solar cells. J. Phys. Appl. Phys. 46, 135106. doi:10.1088/0022-3727/46/13/135106

Grover, S., Moddel, G., 2012a. Engineering the current–voltage characteristics of metal–insulator–metal diodes using double-insulator tunnel barriers. Solid-State Electron. 67, 94–99. doi:10.1016/j.sse.2011.09.004

Grover, S., Moddel, G., 2012b. Engineering the current–voltage characteristics of metal–insulator–metal diodes using double-insulator tunnel barriers. Solid-State Electron. 67, 94–99. doi:10.1016/j.sse.2011.09.004

Grover, S., Moddel, G., 2011. Applicability of Metal/Insulator/Metal (MIM) Diodes to Solar Rectennas. IEEE J. Photovolt. 1, 78 –83. doi:10.1109/JPHOTOV.2011.2160489

Hagerty, J.A., Helmbrecht, F.B., McCalpin, W.H., Zane, R., Popovic, Z.B., 2004. Recycling ambient microwave energy with broad-band rectenna arrays. IEEE Trans. Microw. Theory Tech. 52, 1014–1024. doi:10.1109/TMTT.2004.823585

Hamilton, C.A., Shapiro, S., 1970. rf-Induced Effects in Superconducting Tunnel Junctions. Phys. Rev. B 2, 4494–4503. doi:10.1103/PhysRevB.2.4494

Hartman, T.E., 1962. Tunneling of a Wave Packet. J. Appl. Phys. 33, 3427–3433. doi:doi:10.1063/1.1702424

Hartstein, A., Weinberg, Z.A., 1979. Unified theory of internal photoemission and photon-assisted tunneling. Phys. Rev. B 20, 1335–1338. doi:10.1103/PhysRevB.20.1335

Hartstein, A., Weinberg, Z.A., 1978. On the nature of the image force in quantum mechanics with application to photon assisted tunnelling and photoemission. J. Phys. C Solid State Phys. 11, L469. doi:10.1088/0022-3719/11/11/006

Heiblum, M., Wang, S., Whinnery, J., Gustafson, T., 1978. Characteristics of integrated MOM junctions at DC and at optical frequencies. IEEE J. Quantum Electron. 14, 159 –169. doi:10.1109/JQE.1978.1069765

Hobbs, P.C.D., Laibowitz, R.B., Libsch, F.R., 2005. Ni-NiO-Ni tunnel junctions for terahertz and infrared detection. Appl. Opt. 44, 6813–6822. doi:10.1364/AO.44.006813

Hobbs, P.C.D., Laibowitz, R.B., Libsch, F.R., LaBianca, N.C., Chiniwalla, P.P., 2007. Efficient waveguide-integrated tunnel junction detectors at 1.6 ?m. Opt. Express 15, 16376–16389. doi:10.1364/OE.15.016376

Hocker, L.O., Sokoloff, D.R., Daneu, V., Szoke, A., Javan, A., 1968. Frequency Mixing in the Infrared and Far-Infrared Using a Metal-to-Metal Point Contact Diode. Appl. Phys. Lett. 12, 401–402. doi:doi:10.1063/1.1651873

Hoofring, A.B., Kapoor, V.J., Krawczonek, W., 1989. Submicron nickel-oxide-gold tunnel diode detectors for rectennas. J. Appl. Phys. 66, 430–437. doi:doi:10.1063/1.343841

Joshi, S., 2015. Performance limits of optical rectennas. Ph.D. Thesis, University of Colorado.

Joshi, S., Grover, S., Moddel, G., 2013. Efficiency Limits for Solar Spectrum Rectification, in: Moddel, G., Grover, S. (Eds.), Rectenna Solar Cells. Springer New York, pp. 47–67.

Joshi, S., Moddel, G., 2015a. Rectennas at optical frequencies: how to analyze the response. Be Submitt.

Joshi, S., Moddel, G., 2015b. Optical Rectenna Operation: Where Maxwell meets Einstein. Be Submitt.

Joshi, S., Moddel, G., 2015c. Simple figure of merit for optical rectenna analysis. Be Submitt.

Joshi, S., Moddel, G., 2013. Efficiency limits of rectenna solar cells: Theory of broadband photon-assisted tunneling. Appl. Phys. Lett. 102, 083901–083901–5. doi:doi:10.1063/1.4793425

Joshi, S., Zhu, Z., Grover, S., Moddel, G., 2012. Infrared optical response of geometric diode rectenna solar cells, in: 2012 38th IEEE Photovoltaic Specialists Conference (PVSC). Presented at the 2012 38th IEEE Photovoltaic Specialists Conference (PVSC), pp. 002976–002978. doi:10.1109/PVSC.2012.6318209

Kane, E.O., 1969. Basic Concepts of Tunneling, in: Burstein, E., Lundqvist, S. (Eds.), Tunneling Phenomena in Solids. Springer US, pp. 1–11.

Krishnan, S., Stefanakos, E., Bhansali, S., 2008. Effects of dielectric thickness and contact area on current–voltage characteristics of thin film metal–insulator–metal diodes. Thin Solid Films 516, 2244–2250. doi:10.1016/j.tsf.2007.08.067

Landsberg, P.T., Tonge, G., 1979. Thermodynamics of the conversion of diluted radiation. J. Phys. Math. Gen. 12, 551–562. doi:10.1088/0305-4470/12/4/015

Maraghechi, P., Foroughi-Abari, A., Cadien, K., Elezzabi, A.Y., 2012a. Observation of resonant tunneling phenomenon in metal-insulator-insulator-insulator-metal electron tunnel devices. Appl. Phys. Lett. 100, 113503–113503–5. doi:doi:10.1063/1.3694024

Maraghechi, P., Foroughi-Abari, A., Cadien, K., Elezzabi, A.Y., 2012b. Observation of resonant tunneling phenomenon in metal-insulator-insulator-insulator-metal electron tunnel devices. Appl. Phys. Lett. 100, 113503. doi:10.1063/1.3694024

Markvart, T., 2007. Thermodynamics of losses in photovoltaic conversion. Appl. Phys. Lett. 91, 064102–064102–3. doi:doi:10.1063/1.2766857

Mashaal, H., Gordon, J.M., 2013. Solar and Thermal Aperture Antenna Coherence Performance Limits, in: Moddel, G., Grover, S. (Eds.), Rectenna Solar Cells. Springer New York, pp. 69–86.

Mashaal, H., Gordon, J.M., 2011. Fundamental bounds for antenna harvesting of sunlight. Opt. Lett. 36, 900–902. doi:10.1364/OL.36.000900

Matsumoto, Y., Hanajiri, T., Toyabe, T., Sugano, T., 1996. Single Electron Device with Asymmetric Tunnel Barriers. Jpn. J. Appl. Phys. 35, 1126–1131. doi:10.1143/JJAP.35.1126

McPherson, J.W., Kim, J., Shanware, A., Mogul, H., Rodriguez, J., 2003. Trends in the ultimate breakdown strength of high dielectric-constant materials. IEEE Trans. Electron Devices 50, 1771–1778. doi:10.1109/TED.2003.815141

McSpadden, J.O., Fan, L., Chang, K., 1998. Design and experiments of a high-conversion-efficiency 5.8-GHz rectenna. Microw. Theory Tech. IEEE Trans. On 46, 2053 –2060. doi:10.1109/22.739282

Messenger, G.C., McCoy, C.T., 1957. Theory and Operation of Crystal Diodes as Mixers. Proc. IRE 45, 1269–1283. doi:10.1109/JRPROC.1957.278532

Mickan, S.P., Zhang, X.-C., 2003. T-Ray Sensing and Imaging. Int. J. High Speed Electron. Syst. 13, 601–676. doi:10.1142/S0129156403001843

Miskovsky, N.M., Cutler, P.H., Feuchtwang, T.E., Shepherd, S.J., Lucas, A.A., Sullivan, T.E., 1980. Effect of geometry and multiple-image interactions on tunneling and I-V characteristics of metal-vacuum-metal point-contact junctions. Appl. Phys. Lett. 37, 189–192. doi:doi:10.1063/1.91820

Miskovsky, N.M., Cutler, P.H., Mayer, A., Weiss, B.L., Willis, B., Sullivan, T.E., Lerner, P.B., 2012. Nanoscale Devices for Rectification of High Frequency Radiation from the Infrared through the Visible: A New Approach. J. Nanotechnol. 2012, 1–19. doi:10.1155/2012/512379

Moddel, G., 2014. Geometric diode, applications and method. US8803340 B2.

Moddel, G., 2013. Will Rectenna Solar Cells Be Practical?, in: Moddel, G., Grover, S. (Eds.), Rectenna Solar Cells. Springer New York, pp. 3–24.

Moddel, G., Eliasson, B.J., 2004. High speed electron tunneling device and applications. US6756649 B2.

Moddel, G., Grover, S., 2013. Rectenna Solar Cells, 2013 edition. ed. Springer, New York.

Moddel, G., Zhu, Z., Grover, S., Joshi, S., 2012. Ultrahigh speed graphene diode with reversible polarity. Solid State Commun. 152, 1842–1845. doi:10.1016/j.ssc.2012.06.013

Nabity, J., 2015. . Nanometer Pattern Gener. Syst. URL http://www.jcnabity.com/ (accessed 3.18.15).

Nayfeh, O.M., 2011. Radio-Frequency Transistors Using Chemical-Vapor-Deposited Monolayer Graphene: Performance, Doping, and Transport Effects. IEEE Trans. Electron Devices 58, 2847–2853. doi:10.1109/TED.2011.2159721

Oliver, B.M., 1965. Thermal and quantum noise. Proc. IEEE 53, 436–454. doi:10.1109/PROC.1965.3814

Palik, E.D., 1998. Handbook of Optical Constants of Solids. Academic Press.

Pelz, B., University of Colorado - Boulder. Private communication.

Periasamy, P., Berry, J.J., Dameron, A.A., Bergeson, J.D., Ginley, D.S., O'Hayre, R.P., Parilla, P.A., 2011. Fabrication and Characterization of MIM Diodes Based on Nb/Nb2O5 Via a Rapid Screening Technique. Adv. Mater. 23, 3080–3085. doi:10.1002/adma.201101115

Periasamy, P., Guthrey, H.L., Abdulagatov, A.I., Ndione, P.F., Berry, J.J., Ginley, D.S., George, S.M., Parilla, P.A., O'Hayre, R.P., 2013. Metal–Insulator–Metal Diodes: Role of the Insulator Layer on the Rectification Performance. Adv. Mater. 25, 1301–1308. doi:10.1002/adma.201203075

Phiar, Corp. Private communication.

Price, P.J., 1988. Theory of resonant tunneling in heterostructures. Phys. Rev. B 38, 1994–1998. doi:10.1103/PhysRevB.38.1994

Ramanathan, S., Chi, D., McIntyre, P.C., Wetteland, C.J., Tesmer, J.R., 2003. Ultraviolet-Ozone Oxidation of Metal Films. J. Electrochem. Soc. 150, F110–F115. doi:10.1149/1.1566416

Rogalski, A., 2010. Infrared Detectors, Second Edition. CRC Press.

Riley, K.F., Hobson, M.P., Bence, S.J., 2006. Mathematical Methods for Physics and Engineering: A Comprehensive Guide. Cambridge University Press.

Sanchez, A., Davis, C.F., Liu, K.C., Javan, A., 1978. The MOM tunneling diode: Theoretical estimate of its performance at microwave and infrared frequencies. J. Appl. Phys. 49, 5270–5277. doi:doi:10.1063/1.324426

Sarehraz, M., Buckle, K., Weller, T., Stefanakos, E., Bhansali, S., Goswami, Y., Krishnan, S., 2005. Rectenna developments for solar energy collection, in: Conference Record of the Thirty-First IEEE Photovoltaic Specialists Conference, 2005. Presented at the Conference Record of the Thirty-first IEEE Photovoltaic Specialists Conference, 2005, pp. 78 – 81. doi:10.1109/PVSC.2005.1488073

Shockley, W., Queisser, H.J., 1961a. Detailed Balance Limit of Efficiency of p-n Junction Solar Cells. J. Appl. Phys. 32, 510–519. doi:doi:10.1063/1.1736034

Shockley, W., Queisser, H.J., 1961b. Detailed Balance Limit of Efficiency of p-n Junction Solar Cells. J. Appl. Phys. 32, 510 –519. doi:10.1063/1.1736034

Simmons, J.G., 1969. Image force in metal-oxide-metal tunnel junctions, in: Burstein, E., Lundqvist, S. (Eds.), Tunneling Phenomenon in Solids. Plenum Press, New York, pp. 135–148.

Small, J.G., Elchinger, G.M., Javan, A., Sanchez, A., Bachner, F.J., Smythe, D.L., 1974. ac electron tunneling at infrared frequencies: Thin-film M-O-M diode structure with broad-band characteristics. Appl. Phys. Lett. 24, 275–279. doi:doi:10.1063/1.1655181

Sollner, T.C.L.G., Goodhue, W.D., Tannenwald, P.E., Parker, C.D., Peck, D.D., 1983. Resonant tunneling through quantum wells at frequencies up to 2.5 THz. Appl. Phys. Lett. 43, 588–590. doi:10.1063/1.94434

Song, A.M., 2002. Electron ratchet effect in semiconductor devices and artificial materials with broken centrosymmetry. Appl. Phys. A 75, 229–235. doi:10.1007/s003390201334

Thacker, Z., University of Missouri - Columbia. Private communication.

Tien, P.K., Gordon, J.P., 1963. Multiphoton Process Observed in the Interaction of Microwave Fields with the Tunneling between Superconductor Films. Phys. Rev. 129, 647–651. doi:10.1103/PhysRev.129.647

Trivich, D., Flinn, P.A., 1955. Maximum efficiency of solar energy conversion by quantum processes, in: Daniels, F., Duffie, J.A. (Eds.), Solar Energy Research. The University of Wisconsin Press.

Tucker, J.R., 1979. Quantum limited detection in tunnel junction mixers. IEEE J. Quantum Electron. 15, 1234 – 1258. doi:10.1109/JQE.1979.1069931

Tucker, J.R., Feldman, M.J., 1985. Quantum detection at millimeter wavelengths. Rev. Mod. Phys. 57, 1055–1113. doi:10.1103/RevModPhys.57.1055

Vandenbosch, G.A.E., Ma, Z., 2012. Upper bounds for the solar energy harvesting efficiency of nano-antennas. Nano Energy 1, 494–502. doi:10.1016/j.nanoen.2012.03.002

Wilke, I., Oppliger, Y., Herrmann, W., Kneubühl, F.K., 1994. Nanometer thin-film Ni-NiO-Ni diodes for 30 THz radiation. Appl. Phys. Mater. Sci. Process. 58, 329–341. doi:10.1007/BF00323606

Yoo, T.-W., Chang, K., 1992. Theoretical and experimental development of 10 and 35 GHz rectennas. IEEE Trans. Microw. Theory Tech. 40, 1259 –1266. doi:10.1109/22.141359

Yu, F., Moddel, G., Corkish, R., 2014. Quantum Rectennas for Photovoltaics, in: Nozik, A.J., Conibeer, G., Beard, M.C. (Eds.), Advanced Concepts in Photovoltaics. Royal Society of Chemistry, pp. 506–546.

Zhu, Z., 2014. Graphene geometric diodes for optical rectennas. PhD Thesis Univ. Colo.

Zhu, Z., Grover, S., Krueger, K., Moddel, G., 2011. Optical rectenna solar cells using graphene geometric diodes, in: 2011 37th IEEE Photovoltaic Specialists Conference (PVSC). Presented at the 2011 37th IEEE Photovoltaic Specialists Conference (PVSC), pp. 002120–002122. doi:10.1109/PVSC.2011.6186372

Zhu, Z., Joshi, S., Grover, S., Moddel, G., 2013a. Geometric Diodes for Optical Rectennas, in: Moddel, G., Grover, S. (Eds.), Rectenna Solar Cells. Springer New York, pp. 209–227.

Zhu, Z., Joshi, S., Grover, S., Moddel, G., 2013b. Graphene geometric diodes for terahertz rectennas. J. Phys. Appl. Phys. 46, 185101. doi:10.1088/0022-3727/46/18/185101

Zhu, Z., Joshi, S., Moddel, G., 2014. High Performance Room Temperature Rectenna IR Detectors Using Graphene Geometric Diodes. IEEE J. Sel. Top. Quantum Electron. 20, 70–78. doi:10.1109/JSTQE.2014.2318276

Zhu, Z., Joshi, S., Moddel, G., 2014. High Performance Room Temperature Rectenna IR Detectors Using Graphene Geometric Diodes. IEEE J. Sel. Top. Quantum Electron. 20, 1–9. doi:10.1109/JSTQE.2014.2318276

APPENDIX - A

A. Method used to calculate the optical rectenna response

I use the theory of photon-assisted tunneling (PAT) to calculate the optical response of the rectenna. A simplified flowchart of the algorithm is shown in figure A-1 and the detailed steps are as follows.

a. Determine the following input parameters,

   i. Monochromatic illumination: Input intensity (I_{in}) in watts, effective antenna area (A_{eff}) in m^2, antenna radiation resistance (R_S) in ohms, antenna efficiency (η_{ant}), frequency ($f=\omega/2\pi$) in Hz or eV, and the operating voltage (V_O) of the rectenna.

   ii. Broadband illumination: I_{in}, A_{ant}, R_S, η_{ant}, the input intensity spectrum in W/m^2-Hz or W/m^2-eV, and V_O.

   Since the rectenna operates in the second quadrant, the sign of V_O is negative.

b. Calculate the input power available at the antenna (P_{in}^{AC})

$$P_{in}^{AC} = \eta_{ant} A_{eff} I_{in} \tag{A-1}$$

c. Calculate the source voltage in the time-domain

   i. Monochromatic illumination: The peak amplitude of the source voltage is written as,

$$V_S = \sqrt{8 R_S P_{in}^{AC}} \ . \tag{A-2}$$

The time-domain source voltage is,

$$v_S(t) = V_S \cos(\omega t).$$

(A-3)

ii. Broadband illumination: The source voltage spectrum is approximated as the square root of the input intensity/power spectrum. For a blackbody, the power spectrum is a function of the frequency and the temperature (T) of the blackbody, and it follows the 3-dimensional Planck blackbody spectrum,

$$I_{3D}(\omega) \propto \frac{\omega^3}{e^{\frac{\hbar\omega}{kT}} - 1}.$$

(A-4)

For a linear resistor or a 1D dipole antenna, the power spectrum follows the 1-dimensional Planck blackbody spectrum,

$$I_{1D}(\omega) \propto \frac{\omega}{e^{\frac{\hbar\omega}{kT}} - 1}$$

(A-5)

The frequency spectrum is converted to time-domain using a fast Fourier transform (FFT) with random phase spectrum generated using normally distributed pseudorandom numbers to determine the $v_S(t)$. The time-domain voltage is normalized such that the power sent to an impedance matched load is equal to P_{in}^{AC}. The normalization factor is,

$$C = \frac{P_{in}^{AC}}{\frac{1}{T_o}\int_0^{T_o} \frac{[v_S(t)]^2}{4R_S}}.$$

(A-6)

The time-period (T_o) is such that it represents the bandwidth of the rectenna.

d. Approximate the diode voltage $v_D(t)$ by the $v_S(t)$ to calculate the diode current, following PAT theory (Tucker and Feldman, 1985),

$$i_D(t) = \iint d\omega' W(\omega') I_{dark}\left(\omega' + \frac{qV_O}{\hbar}\right) e^{-i\omega' t} d\omega'' W(\omega'') e^{-i\omega'' t}.$$

(A-7).

This equation is represented by the function $f[I_{dark}, v_D(t)]$ in figure A-1. The $I_{dark}(V)$ is the dark $I(V)$ characteristics of an ideal diode, or obtained from tunneling simulations. $W(\omega)$ is calculated by taking the Fourier transform of the time-dependent phase factor,

$$W(t) = \int_{-\infty}^{\infty} d\omega' W(\omega') e^{-i\omega' t} = \exp\left\{-i\frac{q}{\hbar}\int^{t} dt'\left[v_D(t')\right]\right\}.$$

(A-8)

e. Calculate the voltage across the diode at steady state: Since there is no DC current flow in the antenna circuit, the source current $i_S(t)$ is the ac component of the $i_S(t)$. The $i_S(t)$ is substituted in the following equation to calculate $v_D(t)$,

$$v_D(t) = -|V_O| + v_S(t) - i_S(t) R_S.$$

(A-9)

The resulting $v_D(t)$ is adjusted by a factor δ and used again to calculate the $W(t)$ and $i_D(t)$. This step is repeated till the solution of the $(n+1)^{th}$ iteration and the n^{th} iteration is within ε, a small fraction (0.001) of the maximum amplitude of $v_S(t)$.

f. Average the $i_D(t)$ to calculate the DC rectified current through the diode (I_{illum}) at the V_O.

g. Calculate the DC output power (P_{out}^{DC}) and the power conversion efficiency (η) of the rectenna,

$$P_{out}^{DC}(V_O) = |V_O| I_{illum}(V_O) \tag{A-10}$$

$$\eta(V_O) = \frac{P_{out}^{DC}(V_O)}{P_{in}^{AC}}. \tag{A-11}$$

h. Vary the V_O over a range of values to determine the illuminated $I(V)$ characteristics of the rectenna.

i. Find the V_O at which the η is maximum and calculate the required load resistance,

$$R_L = V_O / I_{illum}(V_O) \tag{A-12}$$

The results in chapters I through IV are calculated using this method.

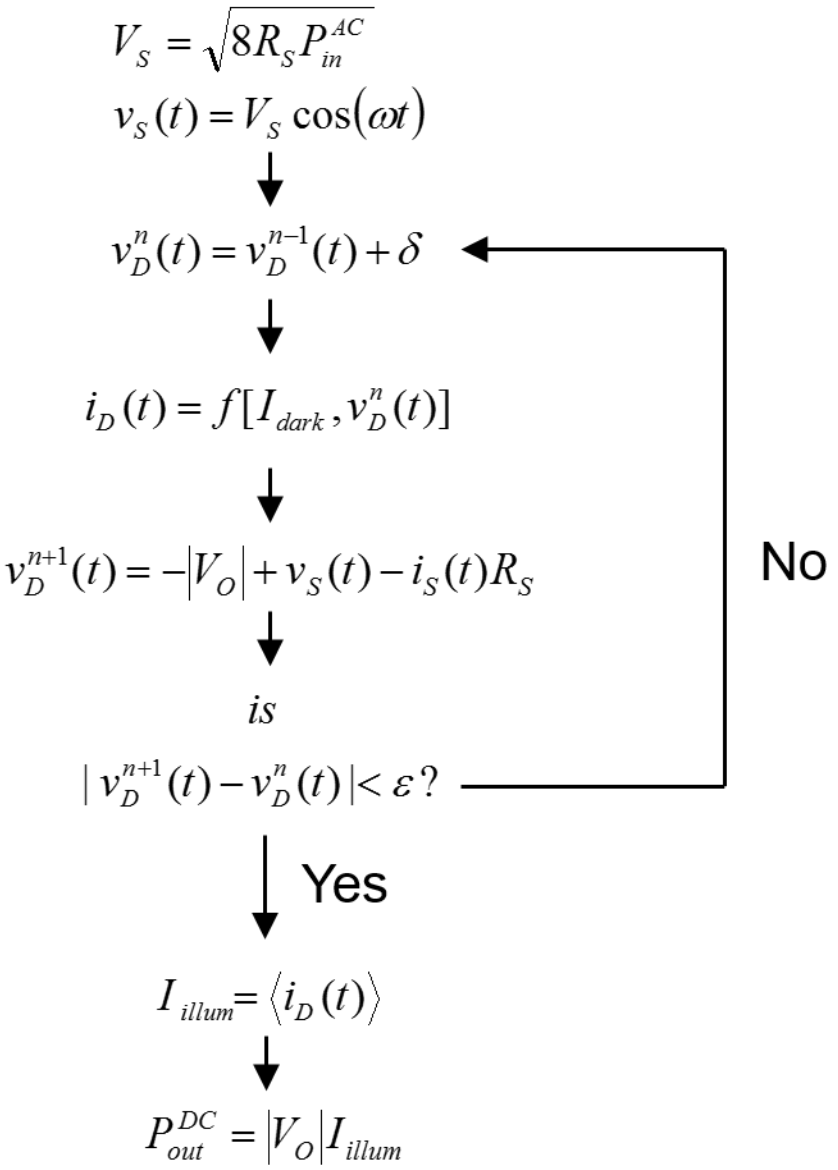

Figure A-1. Simplified flowchart showing the process used to calculate the rectenna response to monochromatic illumination using the theory of PAT. The δ represents the small change in the diode voltage [$v_D(t)$] for every new iteration, repeated till the error ε is reached. In the first iteration, the $v_D(t)$ is chosen to be equal to the source voltage [$v_S(t)$]. The source current [$i_S(t)$] is the ac component of the diode current $i_D(t)$.

References

Tucker, J.R., Feldman, M.J., 1985. Quantum detection at millimeter wavelengths. Rev. Mod. Phys. 57, 1055–1113. doi:10.1103/RevModPhys.57.1055